EarthByte Group

School of Geosciences

The University of Sydney
Australia

The dynamics of subduction and its tectonic implications

Submitted in fulfilment of the requirements
for the degree of Doctor of Philosophy

Nathaniel P. Butterworth

2013

Abstract

Forces associated with subduction are an integral aspect of plate tectonics and mantle processes. However due to the non-linear overlap of physical processes and forces driving subduction their tectonic implications remain difficult to resolve. The aim of this thesis is to examine insufficiently understood drivers of subduction and relate them to their explicit tectonic expressions at regional and global scales. To systematically study the parameters controlling subduction this investigation utilises the Stokes flow solver, BEM-Earth, and the global mantle convection code, Terra. I investigate the role of the plates overriding the subduction zone and the feedbacks between the down-going slab interacting with the surface plates. Particularly, I distinguish the force partitioning between the trench-orthogonal and trench-perpendicular mantle flow induced by a subducting slab's overriding plate. It is determined that overriding plate rheology, boundary configuration, and kinematics interact and partially control subducting slab morphology and velocity. This is important for explaining surface plate motions and apparent structure of positive wave-speed anomalies in the mantle imaged with seismic tomography. I further analyse subduction driven forces acting on the Pacific Plate, during the Late Cretaceous and early Cenozoic, and spatially and temporally correlate resulting plate motions and subsequent lithospheric deformation to geophysical observations. The modeled buoyancy driven subduction self-consistently produces surface plate motions, in-turn providing constraints on absolute reference frames and plate kinematics. Subducting slabs are found to induce lithospheric deformation, far away from plate boundaries, that correlate with volcanic products, helping identify which hotspot mechanisms are responsible for intraplate seafloor structures. I also unravel subduction histories to constrain the accuracy of absolute reference frames and quantify regional and global slab sinking rates. I use alternative absolute plate reconstruction reference frames as input, to reproduce present-day subducted slabs globally, and compare the resulting mantle structure with geological constraints and seismic tomography. Disentanglement of slab sinking velocities and suduction history has implications for coupling regional subduction models to global-scale analyses, linking geological observations with deep seismic tomography anomalies, and subsequently producing tighter constraints on the validity of absolute reference frames. This multi-scale analysis of subduction provides a deeper understanding of Earth's tectonic configurations and resulting geological processes through time.

Acknowledgements

My gratitude, respect, admiration, and most humble thanks are owed to so many people. Dietmar, a pillar of geoscience, you are damn good at what you do; Leonardo and Gabriele, I have always felt smarter just by being near you; to all of EarthByte for making everything interesting and amazing, thank you; thank you to my office friends, past and present, who share and enlighten my passion for science, and help me with so many things; thanks to my family, every single one of you; and finally, to sweet Saskia, who reminds me everyday, "Somewhere, something incredible is waiting to be known."

Declaration

I declare that this thesis is less than 80,000 words in length, and that the work contained in this thesis has not been submitted for a higher degree at any other university or institution.

No animal or ethical approvals were needed during the completion of this study. The data used in this thesis have been collated for interpretation by the author, all sources have been duly acknowledged, as is the assistance provided by others in preparing this study.

Nathaniel Butterworth, August 2013

Preface

This Ph.D. thesis represents much of the work achieved since its inception on 1st March 2010. It consists of a series of papers published as internationally peer-reviewed journal articles, or submitted to an internationally peer-reviewed journal. The publications are appropriate to the discipline of geology and geophysics and form part of an integrated project in subduction dynamics. The first chapter consists of an introduction providing a broad background on the current state of research in the field of subduction processes, prompting the assumed motivations for pursuing this research. The introductory chapter also provides insight into the methodology and datasets used in this thesis to study subduction processes. Subsequent chapters delve into a specific problem relating to subduction processes. Each of these chapters has been published or prepared for publication in international peer-reviewed journal as this allows my research to be better appreciated by the scientific community rather than gather dust in a dark corner of a university library. Chapter 2 presents an article published in *Geochemistry, Geophysics, and Geosystems*, investigating the role of the overriding plate during subduction. Chapter 3, submitted to *Solid Earth*, examines how subduction morphology controls lithospheric deformation, specifically in the Pacific plate during the Cenozoic. The main aims of Chapter 4, an article published in *The Journal of Geodynamics*, link subduction processes to slab dynamics, investigating the role of plate convergence and subsequent mantle sinking. The final discussion chapter links the thesis together and draws upon each section's conclusions to state what this dissertation offers to the study of plate tectonics. An additional co-author chapter, relevant to the 'subduction dynamics' theme of this thesis, is included in the appendix for further reference, published in *Computational Mechanics*. Each of the core chapters provides its own list of references, and the bibliography of the framing chapters is included at the end. This thesis was originally submitted for review in August 2013 and finalised by April 2014.

Contents

1   Introduction

Differential temperature between the core-mantle boundary and Earth's surface, along with internal heating by radioactive decay, are the driving mechanisms of mantle convection (Davies, 1980). Tectonics is the surface expression of convection, represented as simplified tectonic plates which result from the formation of lithosphere at mid-ocean ridges (Forsyth, 1977). As oceanic crust moves away from the ridge over tens of millions of years it becomes thicker, colder, and more dense because of thermal contraction. Due to the dense lithosphere's gravitational instability, it is eventually recycled back into the mantle at subduction zones (Carlson et al., 1983). Subduction provides one of the fundamental forces driving plate motions (i.e. slab pull and slab suction) and thus modulates the evolution of the Earth's surface and interior over geological time (Bercovici et al., 2000; Conrad and Lithgow-Bertelloni, 2004; Gerya, 2011).

Stresses that result from convergence at subduction zones are imparted and transmitted over regional scales, for example, via orogenesis (Allmendinger et al., 1997; Capitanio et al., 2011), back arc spreading (Molnar and Atwater, 1978; Sdrolias and Müller, 2006), and the generation of stress in the bending lithosphere. Furthermore, feedback mechanisms in a dynamic plate-mantle system mean that subduction-derived stresses also operate on plate-wide (specifically due to the near-rigid behaviour of oceanic plates) and global-scales, including large-scale plate motion changes (Silver et al., 1998; Schellart et al., 2010), plate deformation, and influence on global mantle flow. The geodynamics community has long-attempted to reconcile models of the Earth's tectonic forces with observations to determine which forces are fundamental drivers of plate motions (e.g Forsyth and Uyeda, 1975; Becker and Faccenna, 2009) and their tectonic consequences (e.g. Clouard and Gerbault, 2008; Schellart and Moresi, 2013). Plate driving forces and resistive forces are governed by a non-linear interaction of the plate's physical

properties (Conrad and Hager, 1999; Bercovici, 2003), and thus isolating the effect of a particular parameter is challenging. In order to unravel the mechanisms of subduction-induced forces, geodynamic models that simulate these complex Earth processes may compliment geophysical observations. Geodynamic models aim to be realistic enough to be applicable to natural observations, whilst also being simplistic enough to be explored in a systematic way, enabling the isolation of individual parameters.

This thesis investigates several aspects of the multi-scale nature of subduction processes by linking numerical models and observations to the natural world. Each of the chapters in this thesis presents a series of geophysical controversies, a comprehensive methodology for addressing such problems, and the subsequent observations and interpretations.

Chapter 2 presents new insights into subduction modeling focusing on the influence of the overriding plate on slab geometry and mantle flow. Understanding the time-dependent dynamics of subduction zones remains an unresolved problem as the forces partitioned between the subducting slab and the overriding plates through time have not yet been thoroughly investigated. In this chapter the effect of mantle flow induced by overriding plates are investigated and compared with the strengths of slab bending resistance, slab pull, and ridge push. Concurrently, deformation regimes in the overriding plate, related to its length, width and rheology, are explored.

Chapter 3 explores the plate kinematic consequences of varying slab pull forces acting on the Pacific Plate during the early Cenozoic and Late Cretaceous. The full plate dynamics are investigated to resolve issues regarding the effective contributions of forces to the motion of the plates from various sources, including slab pull, ridge push and basal tractions from viscous mantle flow. The tectonic consequences of these forces, such as links to plate reorganizations and stress distributions, are analysed and compared with geochemical observations to provide mechanisms for understanding non-plume related hotspot products.

Chapter 4 provides a thorough geophysical analysis of the dynamics of sinking slabs. Geological observations, tomographic modeling, kinematic reconstructions, and geodynamic models are analysed, to estimate a global mean slab sinking rate. I investigate the evolution of subducting slabs as they enter the upper mantle and continue their descent through the transition zone and their sinking trajectory towards the core-mantle boundary.

A discussion is provided to contextualise the three core chapters and highlight

their implications on our understanding of subduction zone geodynamics. I highlight the tectonic consequences resulting from the dynamics of each of the subduction processes examined.

1.1 Methodologies

To investigate the multi-scale subduction processes, several datasets and methodologies have been employed. The details and context of each dataset and methodology are described in each chapter, but are presented here in summary form.

1.1.1 Datasets and Tools

Geophysical observations essential to understanding the tectonosphere and Earth's mantle have been utilised in this thesis. Firstly, the use of plate tectonic models (e.g. Seton et al., 2012) in the plate reconstruction software, GPlates (Boyden et al., 2011), to visualise ancient plate arrangements have been vital to the applications of testing alternative scenarios of subduction investigated in this thesis. Paleo-ages of oceanic lithosphere (Müller et al., 2013), that influence the thickness of thermal lithosphere, provided the basis for much of the subduction volumetric analysis used in Chapters 3 and 4. The vertical gravity gradient (Sandwell and Smith, 2009) and the Global Seamount Database (Kim and Wessel, 2011) were used for analysis of the complexity of seafloor structures. I made use of the GEOROC (Max Planck Institute for Chemistry, Mainz) database to organise and research the volcanics of the Pacific. The Slab1.0 model (Hayes et al., 2012) helped to benchmark model input. P and S-wave seismic tomography models of the mantle (Li et al., 2008; Simmons et al., 2010; Ritsema et al., 2010; Montelli et al., 2004) were necessary for comparing our geodynamicaly derived models of the Earth. The fracture zone dataset (Matthews et al., 2011) was used in our reconstructions and was vital in the interpretations of our models' tectonic consequences in how stress is localised on pre-existing crustal heterogeneities.

1.1.2 Geodynamic Modeling

Over geological timescales the mantle deforms slowly through dislocation and diffusion creep. Numerical modeling of fluid dynamics forms the basis for many geophysical investigations (Gerya, 2011). Simulating convective mantle processes typically rely on a few key physical principals and assumptions beginning with *conservation of mass, momentum, and energy*.

We may begin with the non-dimensional conservation equations, as formulated by Zhong et al. (2007),

$$u_{i,j} = 0 \tag{1.1}$$

$$\sigma_{ij,j} + RaT\delta_{i3} = 0 \tag{1.2}$$

$$\frac{\partial T}{\partial t} = u_i T_{,i} = (\kappa T_{,i})_{,i} + \gamma \tag{1.3}$$

where u_i and σ_{ij}, are the velocity and stress tensors respectively, T is the temperature, γ the heat-production rate, Ra is the Rayleigh number, and δ_{ij} is the Kronecker delta.

Within the scope of this thesis, two significant mantle convection codes have been utilised for exploring the state of mantle convection in the natural world. The first code, *BEM-Earth* (Morra et al., 2007), has been developed contemporaneously with this thesis. The second, *Terra* (Baumgardner, 1983; Bunge and Baumgardner, 1995; Bunge, 1997), has been previously well-utilised (e.g. Shephard et al., 2012; Davies, 2008; Clarke et al., 2013) and has a well-established development community.

BEM-Earth

Obtaining accurate numerical solutions of variable viscosity Stokes flow, which assumes viscosities are high and velocity is low, is one of the most important issues for better geodynamic understanding of mantle convection and mantle melting. An ideal numerical approach for solving global geodynamics should be able to handle drastic viscosity changes, free surfaces, diverse scales, and the effects of these components in a multi-scale framework in spherical global coordinates. The *Boundary Element Method* (BEM) is a numerical method for solving linear partial differential equations formulated as integral equations (Pozrikidis, 1992). BEM uses fewer computational elements than traditional *Finite Element* and *Finite Difference* methods used in geodynamics (Morra et al., 2009).

BEM-Earth is the software utilised for the numerical models in Chapters 2 and 3. It is a BEM code with a Fast Multipole (FM) implementation, as described by Morra et al. (2007). The FM-BEM is a novel numerical method that is well suited for plate tectonic modeling involving processes at planetary scales.

Equations governing mantle convection are derived from the *conservation of mass, momentum, and energy*. Numerical methods are required to solve these

equations. Such solutions are the basis of the boundary-integral representation, whereby a Stokes flow in a given domain is expressed in terms of surface integrals of velocities and stresses over the domain boundaries. The dimensionality of the problem is thereby reduced by one (from 3D to 2D or from 2D to 1D), making the boundary element method a powerful numerical technique that does not require discretisation of the whole flow domain (Zhong et al., 2007).

For Stokes flow problems one only needs to solve equations 1.1 and 1.2 so as to consider the dynamic effects of a given buoyancy field or prescribed surface plate motion on gravity anomalies, deformation rate, and stress at the surface and the interior of the mantle. Numerical approaches used for modeling geodynamics adopt several more assumptions in order to simplify the flow equations to solve. BEM-Earth does not include the heat equation within the model, instead an effective viscosity represents a combined thermo-chemical boundary. The simplest mathematical formulation for mantle convection within BEM-Earth enforces incompressibility whereby it assumes density does not change with time. In the models, the mantle is considered to be based on the general continuum hypothesis, requiring quantities (e.g. density, viscosity) to be defined everywhere at discrete points. Adopting such a hypothesis for the mantle is an estimate, as the mantle is known to be heterogenous at various scales, and is made of compositionally distinct grains (Ricard, 2007). The equation of continuity with the incompressibility condition is thus

$$\nabla \cdot \mathbf{u} = 0 \tag{1.4}$$

where $\mathbf{u}$ is the velocity field. Another simplification comes from the *Boussinesq approximation*, suggesting density differences are small enough to be neglected, so inertia is negligible and gravity is dominant. Given the boundary conditions of a Stokes flow, this can be found without any temporal knowledge of the flow. As such, the formulation of Stokes flow equation for a highly viscous flow is given by

$$\nabla \cdot \sigma + \rho \mathbf{b} = 0, \tag{1.5}$$

where σ is the full stress tensor, ρ is the density, $\mathbf{b}$ represents the body forces (e.g. gravity). In terms of the dynamic viscosity μ, and the pressure P, the gradient of the stress tensor is

$$\nabla \cdot \sigma = \mu \nabla^2 \mathbf{u} - \nabla P. \tag{1.6}$$

For whole-Earth geodynamic problems, solving the Stokes equation using the BEM (Morra et al., 2009) requires subdividing the mantle into several closed

regions, each characterised by an effective temperature and composition, and thus a constant viscosity. So we define a relative viscosity between a surface (e.g. a subducting slab) μ_i, and a reference viscosity (e.g. the mantle) μ_0, as $\lambda_i = \frac{\mu_i}{\mu_0}$. The Stokes equation (Equation 1.1.2) can be evaluated in integral form using the BEM (Morra et al., 2009; Grzhibovskis et al., 2011) for some point on a surface, $\mathbf{x} \in \partial S_j$, as

$$
\begin{aligned}
\mathbf{u}(\mathbf{x_0}) = & - \left(\frac{1}{1 + \lambda_i} \right) \frac{1}{4\pi\mu_0} \sum_j \int_{S_j} \mathbf{G}(\mathbf{x}) \cdot \Delta\mathbf{f}(\mathbf{x}) \, dS(\mathbf{x}) + \\
& \sum_j \left(\frac{1 - \lambda_j}{1 + \lambda_i} \right) \frac{1}{4\pi} \int_{S_j}^{PV} \mathbf{u}(\mathbf{x}) \cdot \mathbf{T}(\mathbf{x}, \mathbf{x_0}) \cdot \mathbf{n}(\mathbf{x}) \, dS(\mathbf{x}).
\end{aligned}
\tag{1.7}
$$

The normal to the surface at each point is given by $\mathbf{n}$, the principal value of the integral is PV, for the diverging terms. $\mathbf{T}$ and $\mathbf{G}$ represent the Green's functions for the traction and velocity fields respectively. And here the body force (i.e. gravitational buoyancy) difference at an interface is $\Delta\mathbf{f} = \Delta\rho(\mathbf{b} \cdot \mathbf{x}) \cdot \mathbf{n}$. The velocity and stress fields are determined within the confines of the boundary, and the problem is only solved at each interface between boundaries.

Traditionally, mantle dynamic software utilise the Finite Difference and Finite Element methods; these have a high number of degrees of freedom N, scaling as $N = (L/h)^3$, where L is the model size (i.e. Earth diameter) and h is the resolution. The Fast Multipole Boundary Element Method applied in BEM-Earth operates with a substantially reduced number of degrees of freedom, scaling as $N = (L/h)^2$, improving computational performance.

The FM-BEM speedup and low memory requirements derived from the use of 3 dimensional analytical solutions defined only on the surface of the regions of interest, allows solving on bigger and finer meshes in a more convenient lower dimensionality. This suits more ambitious solutions to problems where global structures like the subducting plates are to be strongly coupled to small-scale dynamics such as rising plumes. Such improvement in performance allows effective modeling of such multi-scale problems self-consistently (Quevedo et al., 2010), that is to let the system follow fundamental forces like gravity in an unconstrained fashion, and reproduce the measured quantities by tuning the unknown driving forces like slab pull, ridge push or mantle drag.

The FM-BEM solver has been parallelised using MPI. Parallel efficiency on an Opteron cluster with Quadrics connections shows very good scaling up to 64 CPUS, still keeping 90% efficiency (Morra et al., 2009). In its current implementation the FM-BEM uses a shared KD-tree, thus reducing the communication load

at the expense of memory requirements. Parallel efficiency is mainly affected by geometrical mesh query and manipulation routines that are currently in process of being parallelised. The surface mesh resolution can vary dynamically and track the physics of interest by using a refined mesh in places, saving computational time.

BEM-Earth models are fully dynamic, making no predispositions on velocity. And by utilising a spherical domain, we remove the consequences of pre-imposed boundary conditions. To determine parameters for model input, we make deductions based on the geophysical and geological observations. For additional information on BEM-Earth, including its numerical implementation, see Chapters 2 and 3, Appendix A, and Grzhibovskis et al. (2011).

1.1.3 Terra

Terra is a global mantle convection code solving for momentum and heat conservation on a spherical shell. Terra discretises the global spherical shell into a icosahedral grid for full parallelisation. The grid allows for a finite element (FE) analysis of the conservation equations solved using a multigrid method (Baumgardner, 1983). FE methods are extensively and effectively used to solve differential equations with complicated geometries and material properties, thus are well suited to geoscience problems (Moresi and Gurnis, 1996; Zhong et al., 2007; Ulvrová et al., 2012). The FE method divides the domain into a collection of subdomains each with its own set of element equations (simpler equations that locally approximate the original problem). This is followed by the combination of all sets of elemental equations into a global system of equations. In essence the FE method transforms a very complex set of partial differential equations into a giant linear algebra problem.

The nonlinear energy transport described in equation 1.3 is treated explicitly with a multidimensional positive definite advection transport algorithm (Bunge, 1997). The code does not impose compressibility and so *conservation of mass* describes the physical properties defined within a model. The physical properties are described by field variables (as scalars, vectors, or tensors), such as temperature, velocity, and stress, etc. Terra utilises the Uzawa pressure correction strategy for solving the FE formulation of the discretised Navier-Stokes and incompressibility equations. The equations governing the Terra simulations through time, t, can thus be formulated similar to BEM-Earth as

$$\nabla \cdot \mathbf{u} = 0, \tag{1.8}$$

$$\mu \nabla^2 \mathbf{u} - \nabla P + R(\bar{T} - T)\hat{\mathbf{k}} = 0, \tag{1.9}$$

$$\frac{\partial T}{\partial t} + \mathbf{u} \cdot \nabla T = \nabla^2 T + h. \tag{1.10}$$

Here $\mathbf{u}$, P and T are the fields of velocity, pressure and temperature respectively, $\bar{T}$ is the radial temperature profile, μ is the viscosity, R is the Rayleigh number, $\hat{\mathbf{k}}$ is the gravitational unit vector, and h is the internal heating rate. For a full mathamatical implementation the reader is directed to Bunge et al. (2003).

Boundary conditions for velocities and temperatures must be specified in Terra simulations at the surface of the Earth and the CMB. This is set to a fixed value for temperature. Appropriate velocity vectors that are free-slip at the CMB and no-slip (specified surface kinematics from plate motion reconstructions) at the surface of the Earth (Bunge et al., 2003). To overcome the unknown initial conditions the technique of data assimilation is used (Hager and O'Connell, 1979). Thus Terra models use a set of 'known' parameters for temperatures, velocities, and heating constants (Bunge, 1997), through data assimilation and initial conditions, along with the physical laws governing the mantle flow to solve the convection problem. Terra, as used here, implements a layered viscosity structure, a simplified reflections of the Earth's mantle.

2   Article 1

Butterworth, N. P., Quevedo, L.,Morra, G., and Müller R. D. (2012), **Influence of overriding plate geometry and rheology on subduction**, *Geochem. Geophys. Geosyst.*, 13, Q06W15, doi:10.1029/2011GC003968.

Geochemistry
Geophysics
Geosystems

G³

Influence of overriding plate geometry and rheology on subduction

N. P. Butterworth and L. Quevedo
EarthByte Group, School of Geosciences, University of Sydney, Madsen Building, Sydney, New South Wales 2006, Australia (nathaniel.butterworth@sydney.edu.au; leonardo.quevedo@sydney.edu.au)

G. Morra
School of Earth and Environmental Sciences, Seoul National University, Gwanak-gu, Seoul 151-742, South Korea (gabrielemorra@gmail.com)

R. D. Müller
EarthByte Group, School of Geosciences, University of Sydney, Madsen Building, Sydney, New South Wales 2006, Australia (dietmar.muller@sydney.edu.au)

[1] Subduction dynamics is strongly dependent on the geometry and rheology of the subducting slab and adjacent plates, as well as on the induced mantle flow driven by the evolution of tectonic configurations along subduction zones. However, these processes, and the associated plate tectonic driving forces, are difficult to study using time-dependent 3-dimensional computer simulations due to limitations in computing resources. We investigate these phenomena with a novel numerical approach, using BEM-Earth, a Stokes flow solver based on the Boundary Element Method (BEM) with a Fast-Multipole (FM) implementation. The initial BEM-Earth model configurations self-consistently determine the evolution of the entire lithosphere-mantle system without imposing additional constraints in a whole-Earth spherical setting. We find that models without an overriding plate overestimate trench retreat by 65% in a 20 m.y. model run. Also, higher viscosity overriding plates are associated with higher velocity subducting slabs, analogue to faster oceanic plates subducting beneath more rigid continental lithosphere. In our models poloidal flows dominate the coupling between the down-going and overriding plates, with trench-orthogonal length variations in overriding plates inducing flows at least ~2× stronger than trench-parallel width variations. However, deformation in the overriding plate is related to its length and width, with narrower and longer plates extending more than wider and shorter plates.

Components: 9400 words, 6 figures, 3 tables.

Keywords: boundary element method; overriding plate; plate driving forces; subduction.

Index Terms: 8120 Tectonophysics: Dynamics of lithosphere and mantle: general (1213); 8155 Tectonophysics: Plate motions: general (3040); 8170 Tectonophysics: Subduction zone processes (1031, 3060, 3613, 8413).

Butterworth, N. P., L. Quevedo, G. Morra, and R. D. Müller (2012), Influence of overriding plate geometry and rheology on subduction, *Geochem. Geophys. Geosyst.*, *13*, Q06W15, doi:10.1029/2011GC003968.

Theme: Plate Reconstructions, Mantle Convection, and Tomography Models: A Complementary Vision of Earth's Interior
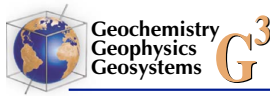
1. Introduction

[2] Subduction of tectonic plates forms an integral aspect of mantle convection. However some aspects of the explicit forces driving this phenomenon remain ambiguous. Here we use a numerical model that helps elucidate the dynamics of subduction systems. The simplest numerical subduction models have down-going slabs that are driven purely by the negative buoyancy of the slab in a two dimensional domain with only a single subducting plate [e.g., *Ribe*, 2010; *Di Giuseppe et al.*, 2008], allowing for investigating the dynamics of the down-going slab. Extending this to three dimensions [*Morra et al.*, 2006; *Schellart et al.*, 2007; *Capitanio et al.*, 2009; *Morra et al.*, 2009; *Stegman et al.*, 2010a, 2010b; *Schellart et al.*, 2010] allows also investigation of the trench-parallel component of the subducting plate's effect on mantle dynamics. Recent studies have also considered the significant influence that the overriding plate, sometimes referred to as the upper plate, has on the down-going slab, both in a dynamic simulation environment [*Arcay et al.*, 2008; *Clark et al.*, 2008; *Yamato et al.*, 2009; *Capitanio et al.*, 2010; *van Dinther et al.*, 2010], and also from an observational perspective [*Lallemand et al.*, 2005; *Schellart*, 2008a]. Further, the relative contributions of the major plate driving forces are well resolved [*Conrad and Lithgow-Bertelloni*, 2004]. But still, the forces distributed between the subducting slab and the overriding plates through time have not yet been thoroughly investigated. As such we try to pin down the difference in overriding plate and subducting slab coupling forces arising from various tectonic configurations. A statistical analysis of the role of the overriding plate, the subducting plate, and correlations to mantle flow in controlling subduction is given by *Lallemand et al.* [2005].

[3] Here, we utilize a fast Stokes flow solver, BEM-Earth, to model lithospheric slab coupling processes with the mantle. The FM-BEM implementation in BEM-Earth is a novel numerical method that is well suited for plate tectonics modeling involving processes at planetary scales. Our BEM-Earth models depict free-subduction, where the down-going slabs are driven purely by the negative buoyancy of the slab. We analyze subduction zone geometries of varying overriding plate and subducting plate thickness, length, and width. The dynamic variations that result are inherited from the respective poloidal and toroidal mantle flows induced by the various geometrical set-ups. The rheology of the subducting plate and the surrounding environment (the mantle, near-by plates, etc) also have an influence on the

dynamics of the interacting plates. As such we also investigate various plate viscosity ratios between the overriding plate and subducting plate, and the affect these parameters have on the subduction dynamics. The overriding and subducting plates are coupled through mantle flow and interplate forces so there is an effect on the overriding lithosphere from the down-going slab, and conversely there is an effect that the overriding plate has on the subducting slab. *Becker and O'Connell* [2001] and *Becker and Faccenna* [2009] showed that velocity correlations were not very sensitive to edge forces, accordingly our models disregard intraplate interactions. Because of the computational efficiency of BEM-Earth, we are able to make use of a full three-dimensional spherical model for a number of consecutive model runs to explore the geometric and rheological parameters existing in natural subduction. Our numerical models reflect the 'mode 1' subduction style of laboratory models of *Bellahsen* [2005]. The style of subduction observed is also consistent with the 2D-BEM simulations of *Ribe* [2010] and the Finite Element simulations of *Di Giuseppe et al.* [2008] and *Capitanio et al.* [2010].

2. Boundary Element Method Model Setup

[4] We utilize BEM-Earth [*Morra et al.*, 2007], a BEM code with a FM implementation, that solves for Stokes flow over a given domain. The BEM [*Pozrikidis*, 1992] is a numerical method for solving linear partial differential equations formulated as boundary integral equations.

[5] BEM-Earth produces fully dynamic models, unconstrained by velocity boundary conditions, allowing for parameters of the system to be specified at input, including, viscosity, density, and geometry. Each iteration of the code then determines velocity and stress fields over each of the model's rheological isosurfaces. Each isosurface bounds a homogenous region characterized by an effective density and viscosity, representative as an average of their properties, in line with a well established modeling framework [*Capitanio et al.*, 2010; *Ribe*, 2010]. The viscosity contrast between each isosurface is fixed for the simulation, thus thermal effects are not considered in the model. Systematic simulations of different initial parameter choices are made, allowing for the determination of each parameter's influence on subduction within the model framework. A schematic cross-section of the model area of interest is shown in Figure 1 with the parameters explained in Table 1.
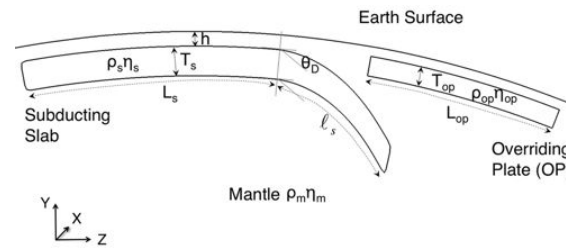
Figure 1. Diagram of a portion of the interacting plates model, with symbols defined. Mantle material permeates the intervening space between each isosurface. The separation of the isosurfaces is maintained by the contact parameters.

[6] Contact properties that influence the interactions between each model isosurface are initially defined. These parameters prevent the slab from detaching from the Earth surface and sinking vertically; rather the subducting plate advances in a more realistic fashion. There are several methods for providing a balancing buoyancy force in numerical models [*Morra et al.*, 2007; *Stegman et al.*, 2010a; *Ribe*, 2010] to keep the plate in local isostatic equilibrium. Here we use a 'lubrication layer' method, where the Earth boundary is described as an adaptive surface, whose dynamic behavior is controlled partially by the distance parameter h. The affect of the contact properties are analyzed in Appendix A and its method of operation is detailed in *Morra et al.* [2012, Appendix D].

[7] The density difference between the mantle and Earth surface self-consistently sustains the unsubducted lithosphere, as on the Earth, but lets the upper surface of the lithosphere free to deform in a full free-surface setting. The density difference drives the plates and the lubrication below the free-surface provides the normal stresses that prevent vertical sinking. During the simulation the Earth surface subsides under the weight of the lithosphere, generating an uplifting force [*Morra et al.*, 2007], reproducing the forcing controlling dynamic topography in the Earth.

[8] We use a spherical Earth made up of 20480 triangular elements on the surface, resulting in a resolution of about 29 km. By utilizing a spherical domain, we remove the consequences of pre-imposed artificial boundary conditions. A rectangular-prism plate is produced with an element resolution of about 24 km, and emplaced within the Earth. The Earth surface is then refined around where the plate is located. Additional isosurfaces are implemented (e.g., overriding plate, trailing plate, etc) as needed for each model. Mantle material permeates the Earth and the spaces between each isosurface. Spaces between isosurfaces vary as the models evolve, with a compressive regime imposed as the contact properties approach a minimum distance. There is no equivalent extensional algorithm at a distance, so the trench-ward pull on the overriding plate produced by suction is underestimated due to this gap.

[9] We maintain two reference models, one with a subducting plate only (Slab-Only), and one with an overriding plate (OP). Parameters used for model input are chosen based on well established parameters and other geodynamic models, detailed in Table 2. The geometric dimensions of the reference model are

Table 1. Model Symbol Definitions and Typical Initial Values

Parameter	Symbol	Value
Length of overriding plate	L_{op}	1274 km
Length of subducting plate	L_s	2038 km
Length of subducted portion of slab	ℓ_s	510 km
Dip angle	θ_D	45°
Thickness of slab	T_s	64 km
Thickness of overriding plate	T_{op}	64 km
Isosurface separation distance	h	26 km

Table 2. Reference Model Parameters

Parameter	Symbol	Value
Earth Radius	r_E	6371 km
Mantle Viscosity	η_m	10^{23} Pa · s
Mantle Density	ρ_m	3300 kg/m^3
Slab Viscosity	η_s	50×10^{23} Pa · s
Slab Density	ρ_s	3400 kg/m^3
Slab Width	W_s	2548 km
Slab Length	L_{sp}	2548 km
Slab Thickness	T_s	64 km
OP Viscosity	η_{op}	50×10^{23} Pa · s
OP Density	ρ_{op}	3270 kg/m^3
OP Width	W_{op}	2548 km
OP Length	L_{op}	1274 km
OP Thickness	T_{op}	64 km

Table 3. Overriding Plate Model Dimensions

Model Name	OP Width (km)	OP Length (km)
Slab-Only	-	-
OP	2548	1274
OP-Wide	3822	1274
OP-Narrow	1274	1274
OP-Long	2548	2548
OP-Long/Wide	3822	2548
OP-Long/Narrow	1274	2548

chosen to reflect a small to medium Earth sized subducting plate. Rheology of the reference model is chosen as the most versatile (in terms of model stress testing) from a range of viscosities tried previously and based on other investigations [*Funiciello et al.*, 2003; *Schmeling et al.*, 2008; *Schellart*, 2008b; *Morra et al.*, 2012; *Capitanio et al.*, 2010; *van Dinther et al.*, 2010]. Versatile contact parameters are difficult to choose for a reference model, subducting plates may detach if they are not strong enough, and the plates may pierce the free Earth surface if they are too weak. Thus, we pick values empirically, that are stable for the greatest range of model parameter choices. Each model is run for 400 time steps, equivalent to about 25 m.y., the output velocity field data is then post-processed leading to the results in the succeeding sections.

[10] We do not consider subduction initiation, as we consider models that represent already established subduction zones which are self-sustaining and driven by the negative buoyancy of the slabs. 20% of the rectangular prism subducting plate is initially bent at a specified dip angle before being projected onto the free-surface sphere. This initial bending is to initiate subduction. The model then evolves freely under gravity through time.

[11] The mantle in the model is a homogeneous region with no rheological stratification. This causes slabs to approach vertical sinking with time, but otherwise, the dynamics under investigation are better isolated without the mantle heterogeneity observed in nature.

[12] Including a stiff core in preliminary models showed a negligible effect on the general dynamics of the plate interactions we consider in this paper. As such, the core was removed from the models for computational efficiency.

[13] In this analysis we do not model the ridge push force explicitly. However, ridge push can be considered by tapering the volume and density of the plate's trailing edge. We find that its impact on plate-mantle dynamics in our models is masked out

by the surface contact layer. Since we determine this effect to be on average less than 1%, we use plates with constant thickness for simplicity.

3. Effects of the Overriding Plate on Subduction Dynamics

3.1. Dimensions of the Overriding Plate

[14] Geometrical dimensions of the overriding plate will influence the dynamics of the down-going slab. Here the rheological properties of the subducting plate are maintained, and the length and width of the overriding plate are systematically changed. The initial set-up for each model uses the reference parameters detailed in Table 2, but with different overriding plate dimensions, described in Table 3.

[15] We first consider the motion of the subduction trench as a way to contrast each model. The plot in Figure 2 shows the trench after 22 m.y. evolution. Trench location is defined as the point along the subducting plate corresponding to the minimum value of curvature, further explained in section 4. The Slab-Only model shows the trench rolling-back the furthest from the initial position, consistent with *Capitanio et al.* [2010]. All other models with overriding plates have rolled-back less substantially than the Slab-Only model. The OP-Wide model, behaves similarly to the OP model, indicating that overriding lithosphere extending laterally beyond the trench-parallel extent of the down-going slab has little affect on the subducting plate's evolution. The OP-Narrow model shows substantial slab-rollback on the edges of the subducting plate (where the overriding plate does not overhang) but shows similar trench migration to the OP model in the middle of the slab, further suggesting that the lateral spatial dimension of the overriding plate has a major affect on the down-going slab's evolution. As in the 2-D study of *Capitanio et al.* [2010], we find longer overriding plate models have similar trench shape development to the shorter models but with overall less evident rollback.

[16] The strain from the on-surface stress projection, seen at 10 m.y. in Figure 3, for the down-going plate in each model was found to remain similar regardless of the presence or shape of the overriding plate. Only deformation along the trench differs, along with timing of slab deformation, due to changed slab kinematics. However, the pattern of strain and the type of deformation in the overriding plate depends on its internal geometry. Generally, the strain distribution shows a circular intensity pattern radiating from trench side of the plate. The overall
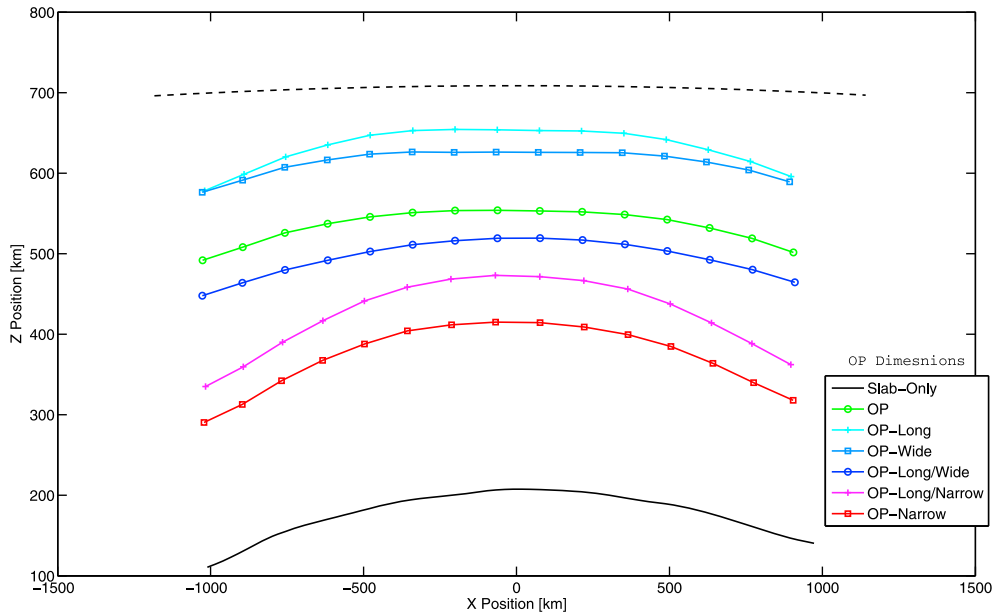
Figure 2. Trench morphology after 22 m.y. evolution projected onto the XZ-plane for the seven models with different size overriding plates. The dashed line shows the position at 0 m.y. for all models. The relative Z-position indicates amount of trench rollback.
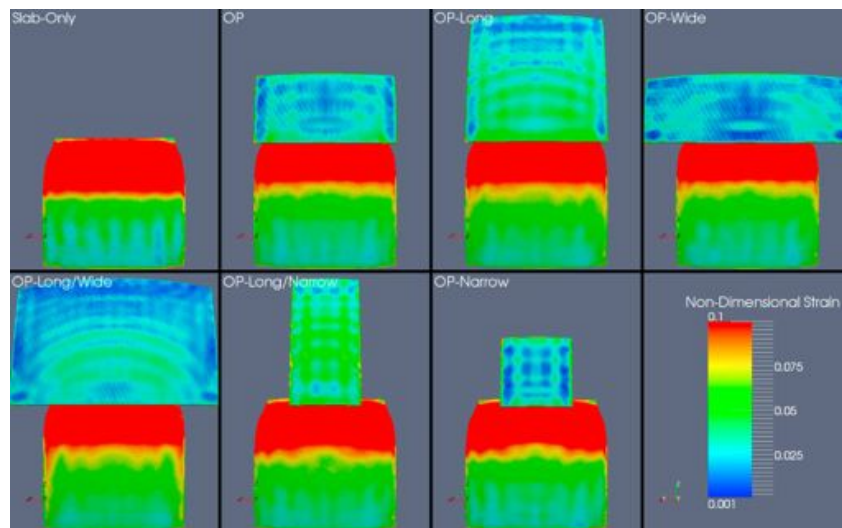

Figure 3. Seven models each with different overriding plate dimensions. The models are labeled in the figure and the dimensions of each overriding plate are given in Table 3. The Earth free-surface has been removed to expose the plates. The colors represent strain after 10 m.y. model evolution, low strain indicates compression and high strain indicates extension. Viscosity in the down-going plate is the same as the overriding plate, leading to highly strained subducting plates.
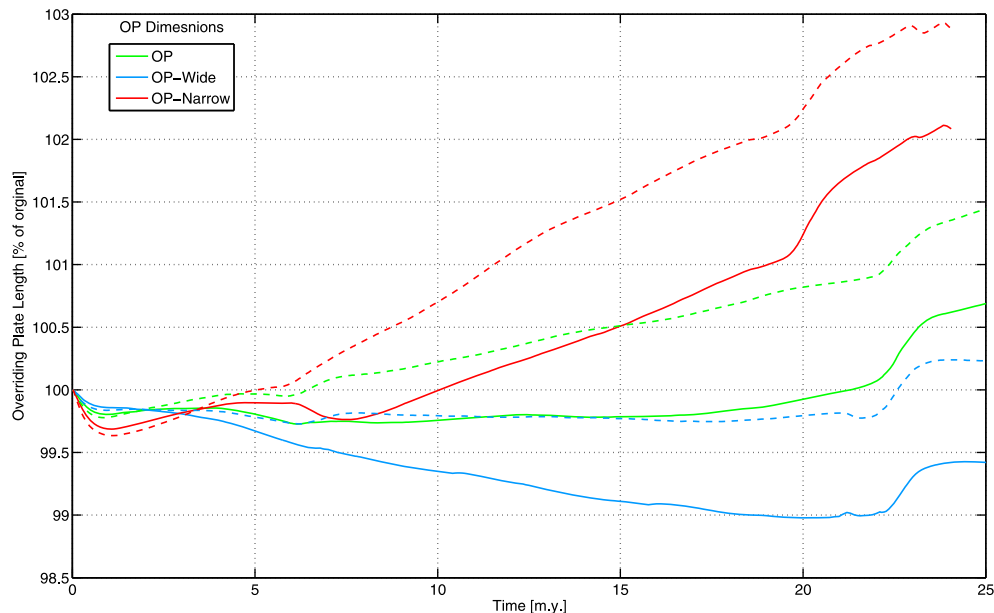
Figure 4. The length of the overriding plate through time for three models with different overriding plate widths. The solid lines are the deformation through the center of the overriding plate. The dashed lines represent a transect 500 km left of the center line.

trend of deformation can be seen in Figure 4, which shows the changing trench-orthogonal length of the overriding plate as the model evolves. In this figure, the three models immediately move into compression. At about 7 m.y. the OP-Narrow overriding plate begins to extend. The OP overriding plate is relatively undeformed until around 20 m.y. evolution when it begins extending rapidly. The OP-Wide overriding plate is continuously in a compressive regime, then around 22 m.y. there is a jump towards extension. After 20 m.y. the deformation of the three models along the center line are: OP-Narrow; 1.3%, OP; −0.1%, and OP-Wide; −1.0%, where positive deformation is extension. The same relative deformation regimes were found for longer overriding plate models but with each overriding plate showing more extension (OP-Long/Narrow; 4.9%, OP-Long; 2.9%, and OP-Long/Wide; 2.0% after 20 m.y.) than the shorter models with equivalent widths. We note that the rate of deformation in our models is generally low compared with that observed in nature.

[17] Poloidal flows induced by the overriding plate only affect the region of subducting plate inline with the trench-parallel lateral extent of the overriding plate. In 2-D studies [e.g., *Ribe*, 2010], a slab descending

into the mantle produces a flow that goes down and under the slab, due to the displacement of the slab material entering the mantle. However in 3-D, material is displaced laterally around the edges as well, resulting in the subducting plate curving along the trench-parallel direction as highlighted in Figure 2. The two narrow models have steeply curved edges similar to the Slab-Only model. Whereas the other four models have similarly curved trenches.

3.2. Influence of Plate Width

[18] Subducting plate speed is found to scale with overriding plate geometric dimensions. The trench-orthogonal length of the overriding plate plays a role in scaling the speed of the subducting plate, with longer overriding plates having faster down-going slabs. The width of the overriding plate has a less substantial role in controlling subducting plate kinematics, but generally wider overriding plates have faster down-going slabs than models with narrower overriding plates. The Slab-Only model has the slowest subducting-plate of the models, moving around half the speed of (the fastest) OP-Long/Wide subducting plate. However, if the subducting plate width is scaled up with the overriding plate width, we find that the subducting plate speed increases with

width. This result is consistent with *Stegman et al.* [2006] and *Schellart et al.* [2010], who found subducting plate width scales with trench and subducting plate velocity in a 3-D cartesian box environment without an overriding plate.

[19] As the width increases the curvature of the subduction zone increases due to the faster velocities away from slab edges. With an overriding plate present the total degree of bending decreases. The general bending is suggested to be due to the curvature of the Earth and also the flow associated with each size plate [*Morra et al.*, 2009; *Mahadevan et al.*, 2010]. The width of the subducting plate will determine the concavity of the trench. A wide subducting plate will be convex, and a narrow subducting plate will be concave. The edges of the wide trenches were shown to have the same flexural shape as subduction zones presented in *Schellart et al.* [2007].

3.3. Influence of Overriding Plate Thickness

[20] Changing the thickness of the overriding plate has a minimal effect on subduction dynamics. This behavior in our three-dimensional free-subduction setting is comparable to the one obtained by *Capitanio et al.* [2010] in a two-dimensional setting. It is observed that thin overriding plates deform more than thicker plates, but the thickness does not influence the subducting slab.

3.4. Influence of a Trailing Plate

[21] A 2548 × 1274 × 64 km plate is introduced behind the subducting plate, referred to as the *trailing plate*. The internal properties are the same as the subducting plate. The length of the gap, L_{gap}, between the trailing plate and the back of the subducting plate is varied between 127–637 km. The trailing plate has the effect of slowing the advance of the subducting plate due to small scale convection in the intervening gap. The L_{gap} distance does not significantly change the coupling between the two plates as the slab dynamics are found to be consistent between each model.

[22] We also compare the trailing plate model with a model that replaces the subducting and trailing plates with one long plate of length $\ell + L_s + L_{gap} + L_{trailing}$. We confirm gap induced dynamics are not a consequence of the length of L_{gap}, but of the gap itself. The presence of any gap appears to change how much the subducting plate will advance as compared to rolling-back. This result in our model is expectedly opposed to natural observations, where a ridge push force

would be actively pushing the advance of the subducting plate. Inclusion of the gap between the subducting plate and trailing plate causes the slab to advance and subduct more for equivalent time. The resulting dynamics of the down-going slab, in the presence of any trailing plate, bears analogy to the conclusions by *Funiciello et al.* [2004]; *Schellart* [2005]; *Stegman et al.* [2010b] of a trailing edge boundary condition having a dominant role in determining the morphology of the slab.

3.5. Influence of Lateral Plates

[23] Emplacing large non-subducting plates adjacent to the subducting plate changes the rate of subduction and the angle of dip. The subducting slab is slowed and the dip angle is decreased compared to a model without the surrounding plates. This same result was found by *Yamato et al.* [2009] in a 3-D cartesian box.

[24] The dynamics of a subducting slab are controlled by more than its internal negative buoyancy force. Adjacent non-subducting plates (overriding, lateral, and trailing plates) affect mantle flows. The non-subducting model isosurfaces act as a conduit to direct the mantle flows induced by the down-going slab. This results in the subducting plate experiencing higher mantle drag and slab suction forces.

3.6. Viscosity of an Overriding Plate

[25] We analyze several models with different overriding plate viscosity values, to determine how ocean-ocean and ocean-continent subduction may differ, addressing the heterogeneity of plate rheology and the possibility that continental lithosphere is more viscous than the oceanic lithosphere [*Zhong*, 2001]. Each model's overriding plate viscosity is changed from 10–$300 \times \eta_m$, whilst all other parameters take the values from Table 2. Models exhibit similar behavior in two distinct overriding plate viscosity regimes, high-viscosity or low-viscosity. The turning point between regimes for our model is found to be $\eta_{op} = 180 \times \eta_m$.

[26] Figure 5 shows a sample cross-section of the high-viscosity and low-viscosity models, along with Slab-Only model, after 15 m.y. evolution. We remark how the flow differs between the models, specifically from the altered shape of the slab. Low-viscosity overriding plate models have greater upturned slab tips than high-viscosity overriding plates. The slab tip in the low-viscosity overriding plate models approach the morphology of the Slab-
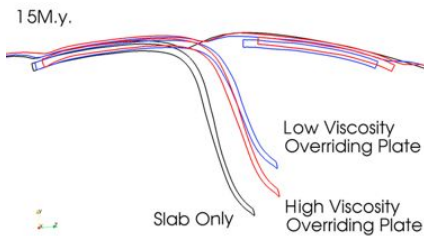
Figure 5. Slice of models with different overriding plate viscosities at 15 m.y. High-viscosity model has $\eta_{op} = 300\eta_m$, the low-viscosity models has $\eta_{op} = 50\eta_m$, and the Slab-Only model is shown in black. Isostatic compensation in BEM-Earth causes the models to move relatively to each other, causing some of the offset between models, but absolute motions are still accurate.

Only model. The deep subduction in the Slab-Only model is allowed because there is no overriding plate to couple to. Because the total energy of the system is conserved, energy is dissipated by deforming the overriding plate more when the viscosity is low, so when there is a high-viscosity overriding plate, energy is available to drive the slab down faster. This in-turn drives the distance between the overriding plate and the trench, thereby increasing the distance for high-viscosity models and decreasing it (approaching the minimum allowed by the contact algorithm) for the low-viscosity models. Following from this, we find the dip of the slab at the trench is slightly steeper, at equivalent times, when a high-viscosity overriding plate is present. However, the angle of dip in all models will be steep due partially to the lack of mantle layering in our BEM-Earth model setup.

[27] The stresses change very little with different dynamics (they are due to elastic propagation of gravity forces), and the dissipation is essentially the inverse of the plate viscosity. In other words, stronger plates deform less and dissipate less energy [e.g., *Capitanio et al.*, 2007]. This leaves more energy for the other plate that can subduct more.

[28] In Figure 5 we can also note the size of the subduction channel, as the gap between the down-going and overriding plate. The low viscosity overriding plate model evolves with a smaller channel than the high viscosity overriding plate model. As the slab going down beneath the high viscosity overriding plate moves faster the force exerted on the overriding plate not only extends the plate, but also pushes it further from the hinge. The initial gap (seen in Figure 1) is set and then subsequently minimized by the contact algorithm. However the contact algorithm utilized has no equivalent 'pulling' regime, so

the only force moving the overriding plate toward the trench is the basal tractions from the induced flows beneath. And thus, there is no intraplate stress propagation between the plates.

[29] Isosurface bulging evident in the models, also seen in Figure 5, is a proxy for the free-Earth surface expression of dynamic topography. Such dynamic topography is due exclusively to the viscous flow in the mantle. Imposing an overriding plate masks the topography as the flow energy interacts with the plate instead of moving the free-Earth surface. However, flexural bulging along the plate isosurfaces is evident due to the mass entering the mantle and the viscosity of the plate causing the plate to bend (bulge).

[30] We consider the plate velocity for each model as being the angular speed at the Euler pole for each timestep, of the unsubducted part of the subducting plate. Overriding plate angular speed is calculated similarly. Figure 6 shows the forward velocities of the subducting plates for each model at 10 m.y. and the corresponding overriding plate velocity. We define the direction of subducting plate advance as the positive Z-direction from Figure 1. This figure is typical of the relative speed of the subducting plate through time, however beyond about 17 m.y. all velocities enter an oscillatory stage, with higher viscosity models having longer wavelength features than lower viscosity models.

[31] Models with overriding plate viscosity of 10–$150\eta_m$ show similar deformation styles and velocities up to 17 m.y. of evolution. In this time frame high-viscosity models tend to sink faster than low-viscosity models, resulting in deeper subduction with a steeper dip angle. Subducting plates will advance forward through time, with the amount of slab-rollback dependent on the properties of the overriding plate. High-viscosity models also show increased plate advance but with enough slab-rollback to maintain equivalent trench position with the low-viscosity models, this is indicated by the positions of the subducting plate's trailing edge and the trench. Still, we find the Slab-Only model show the most slab-rollback. We find that the trench velocity, V_t compared with the subducting plate velocity, V_{sp}, for the Slab-Only model is $\frac{V_t}{V_{sp}} = 1$, and the OP model shows $\frac{V_t}{V_{sp}} = 0.35$, averaged over the model run.

[32] The general pattern of strain on the overriding plate for the OP model (with $\eta_{op} = 50\eta_m$) shown in Figure 3 is consistent for the high and low-viscosity models but showing different magnitudes. Low-viscosity overriding plate models show minimal
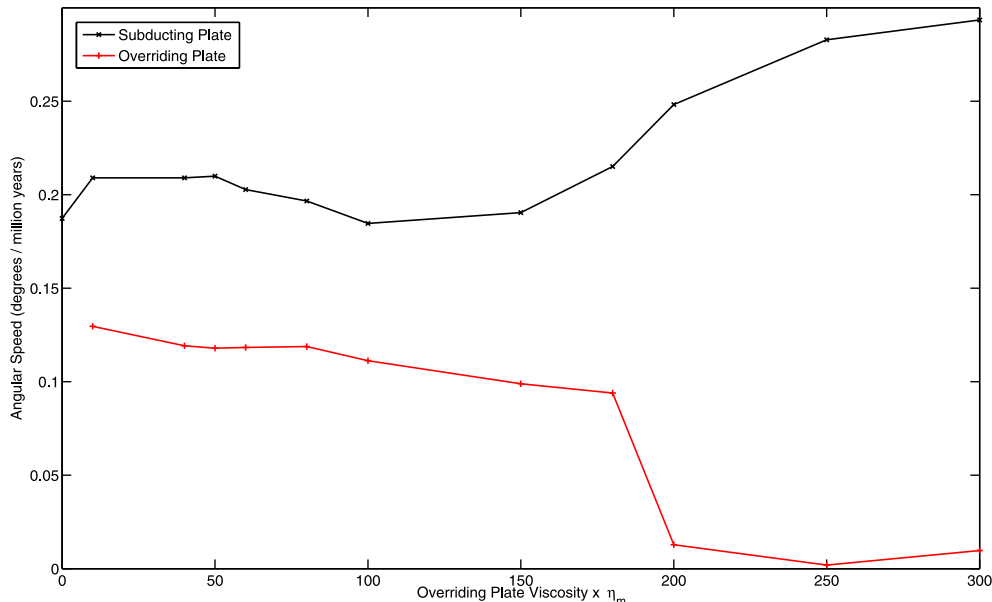
Figure 6. Angular speed of the subducting and overriding plates compared against different overriding plate viscosities at 10 m.y. The subducting and overriding plates are both moving toward the trench, thus the plate speeds are opposite in direction. Angular speed is determined from the plate's Euler pole and averaged every 10 timesteps. Models with $\eta_{op} > 180\eta_m$ have a faster moving subducting plate than models with $\eta_{op} < 180\eta_m$. The model with $\eta_{op} = 0\eta_m$ is the Slab-Only model, and does not have an overriding plate isosurface.

extensive deformation in the overriding plate, and overriding plates $<80\eta_m$ show compressive deformation. The magnitude of deformation increases as viscosity deviates from $\eta_{op} = 80\eta_m$. When the trench velocity approximately equals the overriding plate velocity the back-arc strain is not significant, consistent with the 'neutral line' from *Lallemand et al.* [2008]. High-viscosity models exhibit extension through all time. Low-viscosity overriding plate models and the Slab-Only model results in highest plane stress on the advancing face of the subducting slab either side of the trench, showing similar stress patterns to *van Dinther et al.* [2010]. High-viscosity overriding plate models display more deformation over the entire subducting plate compared to the low-viscosity models. For all models, the strain in the overriding plate becomes more pronounced during periods of subducting plate acceleration, e.g., between 15–19 m.y. During these periods, the entire subducting plate experiences increased deformation compared to lower acceleration periods.

[33] Here we have modeled a fixed geometry with varying overriding plate viscosity to try to gain an understanding of what relatively high and low overriding plate viscosities will have on the evolution of a down-going slab. In all models evolution reveals an upward bending in the forepart of the subducting slab, similar to the models by *Yamato et al.* [2009], even without a mantle viscosity discontinuity that other models generally have. High-viscosity overriding plates cause the subducting plate to evolve quicker than equivalent subducting plates with a low-viscosity overriding plate. The same conclusions are found when the two interacting plates are up to 2× wider, and when the down-going plate's viscosity is increased to $100 \times \eta_m$.

4. Thin-Sheet Analysis of Plate Driving Forces

[34] Each model is independently a good representation of natural subduction, however because of the time-dependency of the models, having implicitly defined time steps with an evolving slab geometry, direct comparison between models is not accurate. As such, we are motivated by the 2-D BEM analysis of *Ribe* [2010] to define geometric
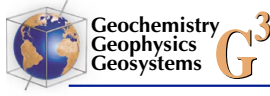
and kinematically defined characteristic quantities which are consistent between models.

[35] We simplify our 3-D analysis by taking a trench-orthogonal row of panels along the upper surface of the subducting plate and project them onto the YZ-plane (removing minor X-direction perturbations). The angle between the unit normal of the panel, $\hat{n}$, and inclination unit vector $\hat{e}_\theta$ is thus related to the trench-ward dip of each panel, θ_D, by

$$\theta_D = \cos^{-1}(\hat{n} \cdot \hat{e}_\theta) - \frac{\pi}{2}. \qquad (1)$$

[36] Now to determine model-independent subducting plate properties, we use the definition of *Ribe* [2003, 2010] for curvature (K) defined along the plate's surface (s) as

$$K = -\frac{\partial \theta_D}{\partial s}. \qquad (2)$$

[37] This leads to the definition of a subducting plate's bending length, ℓ_b. We take ℓ_b as the distance from the tip of advancing face of the slab to the global minimum of K. We use these quantities to determine the forces acting in the models.

[38] The velocity of the down-going slab corresponds to the forces acting upon and within it. It has been shown previously by *Forsyth and Uyeda* [1975] and *Schellart* [2004] that the buoyancy force acting to pull the slab down into the mantle can be approximated by

$$F_b \sim T_s \ell_s W_s \Delta \rho_s g. \qquad (3)$$

[39] Also, the force acting in the forward limb of a subducting slab responsible of the resistance to bending (or slab straightening force) is given per unit length of the trench by [*Ribe*, 2001]

$$F_r \sim \eta_s V \left(\frac{T_s}{l_b}\right)^3. \qquad (4)$$

[40] Finally, there is a resistive viscous drag force on a slab moving in the surrounding mantle with a sinking velocity of V. As shown in *Happel and Brenner* [1983] and *Capitanio et al.* [2007, Appendix A], this force may be approximated by that over a thin ellipsoid with semi-axes $a > b \gg c$ which is given by

$$F_d \sim \frac{\eta_m V a}{1 + \log(a/b)} \qquad (5)$$

The drag force over the overriding plate is in turn proportional to its velocity U_{op} and area A

$$F_{dop} \sim \eta_m U_{op} A \qquad (6)$$

Now, the downward acting buoyant force incites a flow beneath and above the face of the down-going slab causing tractions between the plates. So, the relative velocity between the overriding plate and the down-going slab gives an indication to the relative contributions of the forces acting. Thus we may determine the distribution of forces in each of the models.

[41] Previous plate driving force analysis like that of *Conrad and Lithgow-Bertelloni* [2004] have a net torque within the models due to the imposed pulling force, they correct for this by summing the torques and subtracting the difference. In our BEM-Earth models we produce torque in an absolute frame where only gravity moves material self-consistently, so the total angular momentum of the system is preserved.

[42] We measure a plate's resistance to bending compared to drag in analogy with the definition of the 'stiffness' of a subducting plate given by *Ribe* [2010]

$$\frac{F_r}{F_d} \sim \frac{\eta_s}{\eta_m} \left(\frac{T_s}{\ell_b}\right)^3 \frac{W_s}{a} [1 + \log(a/b)] \equiv S. \qquad (7)$$

This is a measure of a plate's resistance to bending compared to drag along the trench-parallel extent of the subducting plate, W_s.

[43] Cases tested here represent $S < 1$, thus the trench rollback we see in Figure 2 is expected [*Di Giuseppe et al.*, 2008]. There is indication that larger (wider and longer) overriding plates will cause the down-going slab's ℓ_b to evolve slower compared to the smaller (narrower and shorter) overriding plates. By comparison, we find the change in S due to the overriding plate area is at most equivalent to doubling η_s. It is also found lower viscosity overriding plates couple to slabs resulting in high S and vice-versa. Further model runs show S is influenced by the width of the subducting plate. Wider subducting plates generally have increased drag with or without an overriding plate, so S increases.

[44] We can also consider the ratio of the overriding plate drag (F_{dop}) to the down-going slab bending resistance (F_r) representative of a suction type force acting through the poloidal flows coupling the

overriding plate and the down-going slab. We observe that longer models have a lower ratio compared to the shorter models. Generally we find this suction force greatest in the shorter models. We find in quasi-steady state periods the mean difference between $\frac{F_{dop}}{F_r}$ is most affected by the trench-orthogonal length of the overriding plate. Here the difference of $\frac{F_{dop}}{F_r}$ between longer and shorter overriding plate models of equivalent width is ~4.2 × 10^4. The mean difference between models of different widths and equivalent length is ~0.5× smaller, suggesting overriding plate width is not as an important factor as length in coupling the plates.

[45] Finally, we consider the ratio of F_{dop} to slab drag (F_d). We find a similar distribution of forces as in the $\frac{F_{dop}}{F_r}$ relationship. Again, during periods of quasi-steady state there is a distinct force partitioning between the long and shorter models, with shorter models having a greater F_{dop}. We find that the mean difference of $\frac{F_{dop}}{F_d}$ between the longer and shorter overriding plate models of equivalent widths to be ~1.4 × 10^3. The models can be further distinguished by the relative width of the overriding plates, so the narrow plate has the lowest and the wide plate the highest F_{dop} to F_d ratio. As such, $\frac{F_{dop}}{F_d}$ is found to be ~0.5× smaller when comparing models of different overriding plate widths of equivalent length.

[46] Geometric dimensions in the models influence the distribution of forces between the plates. Similar analysis shows high-viscosity overriding plates do not couple as strongly as low-viscosity overriding plates to the down-going slab. Because F_b will be consistent between models, as the amount of material is consistent in each model, we conclude that the different induced suction forces in each of the overriding plate models is causing the change in the plate motion.

5. Discussion and Conclusions

[47] The presence of an overriding plate along the subduction zone reduces the trench-orthogonal motion of the subducting plate directly beneath it, suggesting that poloidal flows dominate the coupling between the subducting slab and the overriding plate. This is backed up by the trench-parallel width of the overriding plate, compared with the trench-orthogonal length of the overriding plate, having a lesser effect on the suction forces coupling the down-going slab and overriding plate. These

results maintain that the presence of an overriding plate tends to slow trench migration [Yamato et al., 2009; Capitanio et al., 2010].

[48] The quantity S can be a good proxy for plate bending curvature [Wu et al., 2008]. Our models suggest that the geometrical and rheological properties of the overriding plate contribute to the stiffness of the down-going plate through the flows coupling the plates together. We find that the strongest coupling of $\frac{F_{dop}}{F_d}$ and $\frac{F_{dop}}{F_r}$ between the subducting and overriding plates (seen in the OP-Wide model) leads to shortening in the overriding plate. As the width of the overriding plate is reduced (OP and OP-Narrow models) the coupling suction decreases and the overriding plate deformation moves into extension. This is compared with weaker coupling in longer (OP-Long/Wide, OP-Long, OP-Long/Narrow) overriding plates that show more extension in the back-arc region. Capitanio et al. [2011] and Laffaldano et al. [2012] considered shear force gradients and intraplate frictional forces respectively of the Nazca-South American plate system to help account for Andean topography. The deformation seen in Figures 2–4 suggests the area of the overriding plate mechanically coupled to the down-going plate influences the shear and intraplate forces that can result in the formation of Andean style topography.

[49] We identify two subduction regimes associated with different overriding plate viscosities: subducting slabs influenced by high-viscosity overriding plates ($\eta_{op} > 180\eta_m$) or by low-viscosity overriding plates ($\eta_{op} < 180\eta_m$). High-viscosity overriding plates increase subducting plate velocity and produce slabs with slightly more steeply dipping angles. The presence of the overriding plate changes the dynamics of the down-going plate, but also changing the viscosity of the overriding plate itself will affect the asthenospheric flow coupling the two plates together.

[50] Invariably our model setup predicates steep angle subduction like that seen in the Western-Pacific. Such deep angle subduction has been linked with back-arc basin formation [Uyeda and Kanamori, 1979; Lallemand et al., 2005], subsequently we expect to see extension in the overriding plates in our models. Also, back-arc extension is expected to begin when the overriding plate moves away from trench [Sdrolias and Müller, 2006]. Overriding plates in our models generally move towards the trench as the slab rolls back. The length of the trench primarily used in this study is

comparable to back-arc systems encountered in nature. Also, the sizes of the overriding plates investigated are similar for the range of overriding plate sizes where back-arcs form. Whilst we find a clear connection in our models between overriding plate width, length and deformation, no such correlation seems to exist in nature. This is partially due to the lack of adjacent plates, that would change the natural movements of the plates. For low-viscosity models we find $V_{op} \approx V_t$, and coincidentally we find back-arc strain to be minimal [*Lallemand et al.*, 2008]. Further, the low-viscosity models show $V_{op} < 0$ and $V_{sp} > 0$. The correlation between deformation in these models to the back-arcs studied in *Lallemand et al.* [2008] is comparable.

[51] The change in subduction dynamics due to only the changing rheology suggests that a subducting plate may deform differently along the trench-parallel subduction extent as it subducts below an overriding plate with a heterogeneous rheology. This is exemplified by the Kamchatka subduction zone, north of Japan, where the subduction style changes along the subduction zone [*Li et al.*, 2008]. Towards the north the Pacific plate is moving relatively slowly at a steep angle, with the overriding plate in extension. Moving to the south, the overriding plate becomes more compressed, the Pacific plate increases speed and the dip angle shallows.

[52] Changing the thickness of the overriding plate has no clear affect on subducting plate dynamics, but influences the deformation in the overriding plate itself. This is consistent with *Capitanio et al.* [2010], but a recent study by *Rodríguez-González et al.* [2012] suggest that a varying trench-perpendicular overriding plate thickness can change subducting plate motion and style. The modeling technique used by *Rodríguez-González et al.* [2012] imposed plate kinematics and restricted vertical movements that may impact the results. Other non-subducting plates immediately behind, and lateral to, a subducting plate are found to slow subduction velocity and change the slab dip. Therefore non-subducting plates adjacent to subduction zones must be considered in more realistic models.

[53] The dynamic evolution of a subducting slab in a spherical setup is influenced by a variety of both intrinsic and external parameters. Inclusion of an overriding plate and other non-subducting plates changes the dynamics of a subduction system by altering velocities over the slab. The rheological and geometric properties of these plates change the

induced mantle flows coupling them with the downgoing slab. This in-turn changes trench migrations and trench curvature. However, the attributes of the overriding plate studied here generate secondary effects that are overwhelmed by other forcings on the system [*Schellart*, 2004; *Capitanio et al.*, 2010; *van Dinther et al.*, 2010]. It appears the down-going slab is the main driver for overriding plate dynamics, in terms of rheology and stress [*Billen*, 2008; *Capitanio et al.*, 2011].

[54] BEM-Earth is emerging as an intermediately complex subduction model framework [*Gerya*, 2011], with simple environmental set-ups with realistic physical model drivers. Dynamically driven models produced in BEM-Earth can provide insights into subduction systems, by easily isolating individual parameters for testing. The nature of the models allows for further complications to be added approaching more complex realistic scenarios at the global scale [*Morra et al.*, 2012].

Appendix A

A1. Contact Parameter Affect

[55] The isosurface separation parameter, h, and the isosurface interaction distance, control the interactions between the isosurfaces. These contact parameters are empirically determined, with the order of $h \sim T_s$, at the beginning of each suite of experiments and kept constant across simulations to be compared. If the contact layer, h, is too small instabilities arise during the computation. If h is too large the uplifting force is not properly calculated so the plate isosurface in 'contact' with the external isosurface will detach and sink vertically into the mantle. This is a standard numerical modeling practice [*Morra et al.*, 2007; *OzBench et al.*, 2008; *Schmeling et al.*, 2008; *Ribe*, 2010] and its implementation in BEM-Earth is detailed in *Morra et al.* [2012, Appendix D].

[56] Different model dynamics can be due to the strength of the contact parameter or due to the altered flow from the presence of an overriding plate. We consider the trench dynamics for determining these relative effects. We analyze 3 sets of well-evolved (22 m.y.) models by changing the contact parameter between the upper ($h = T_s \times 0.42$) and lower stability ($h = T_s \times 0.38$) bounds for these models. We then compare the results to the contact parameter used in the analysis ($h = T_s \times 0.4$). We find the maximum change in the amount

of trench-rollback from the initial position is; 26% increased rollback for the OP models; 8% for the OP-Narrow models; and 15% for the Slab-Only models. Trench morphology is also influenced by the contact. Again, changing the contact within the stability bounds results in at-most a median deviation (from the curvature of the model with the stable contact) of; 1% for the OP models; 2% for the OP-Narrow models; and 5% for the Slab-Only models. Thus, we find flow changes due to the presence of an overriding plate overwhelm the effect of the contact when considering trench morphology and trench-rollback, when the contact parameters are held constant between simulations.

A2. Ridge Push Affect

[57] We use two models, OP and OP with 5% of the trailing edge chamfered. We contrast the bending length of each model at each timestep up to 268 ($\sim$17 m.y.), the time that the chamfered model breaks down by crossing the free-surface. We measure the absolute deviation as $\frac{\ell_{bop} - \ell_{bsharpen}}{\ell_{bop}}$, and find this to be at most 4.792% with a median of 0.003% and a mean of 0.080%. The small amount of deviation allows us to remove this feature from the models.

A3. Thin Sheet Derivation

[58] We take a YZ-plane strip of panels and then transform each panel's coordinates into a spherical coordinate system, and determine a basis unit vector for each panel. Using the centroid of the panel given by position vector, $\vec{r} = (x, y, z)$ in spherical coordinates as $\vec{r} = (\rho, \theta, \phi)$ where

$$
\begin{pmatrix} \rho \\ \theta \\ \phi \end{pmatrix} = \begin{pmatrix} \sqrt{x^2 + y^2 + z^2} \\ \cos^{-1} \frac{z}{\rho} \\ \tan^{-1} \frac{y}{x} \end{pmatrix}.
$$

[59] And the basis unit vectors are determined as

$$
\begin{pmatrix} \hat{e}_\rho \\ \hat{e}_\theta \\ \hat{e}_\phi \end{pmatrix} = \begin{pmatrix} \sin\theta\cos\phi, \sin\theta\sin\phi, \cos\theta \\ \cos\theta\cos\phi, \cos\theta\sin\phi, -\sin\theta \\ -\sin\phi, \cos\phi, 0 \end{pmatrix}.
$$

[60] The angle between the unit normal of the panel, $\hat{n}$, and inclination unit vector $\hat{e}_\theta$ is thus related to the trench-ward dip of each panel, θ_D, by

$$
\theta_D = \cos^{-1}(\hat{n} \cdot \hat{e}_\theta) - \frac{\pi}{2}. \tag{A1}
$$

[61] We also use the orthogonal or normal velocity of the panel, $W = \hat{n} \cdot \vec{v}$, and the longitudinal or tangential velocity, $U = \vec{d} \cdot \vec{v}$, where $\vec{v}(x, y, z)$ is the velocity of the panel, and $\vec{d}(x, y, z)$ is the displacement vector between two adjacent panel centroids.

[62] Now to determine model-independent slab properties, we use the definitions of *Ribe* [2003, 2010] for curvature (K), stretching (Δ), rotation (ω), and curling ($\dot{K}$):

$$
K = -\frac{\partial\theta_D}{\partial s} \tag{A2}
$$

$$
\Delta = \frac{\partial U}{\partial s} - KW \tag{A3}
$$

$$
\omega = \frac{\partial W}{\partial s} + KU \tag{A4}
$$

$$
\dot{K} = \frac{\partial\omega}{\partial s} - K\Delta. \tag{A5}
$$

[63] Numerical differentiation along the slab surface, s, is computed using a smooth noise-robust method (P. Holoborodko, Smooth noise robust differentiators, http://www.holoborodko.com/pavel/numerical-methods/numerical-derivative/smooth-low-noise-differentiators/, 2008) such that the derivative of any function, f, is given by

$$
f' = \frac{2(f_{s_1} - f_{s_{-1}}) + f_{s_2} - f_{s_{-2}}}{2(s_2 - s_{-2})} \tag{A6}
$$

with f' of the first and last 2 panels initialized to 0.

Acknowledgments

References

Arcay, D., S. Lallemand, and M. P. Doin (2008), Back-arc strain in subduction zones: Statistical observations versus

numerical modeling, *Geochem. Geophys. Geosyst.*, *9*, Q05015, doi:10.1029/2007GC001875.

Becker, T. W., and C. Faccenna (2009), A review of the role of subduction dynamics for regional and global plate motions, in *Subduction Zone Geodynamics*, edited by S. Lallemand and F. Funiciello, pp. 3–34, Springer, Berlin, doi:10.1007/978-3-540-87974-9_1.

Becker, T. W., and R. J. O'Connell (2001), Predicting plate velocities with mantle circulation models, *Geochem. Geophys. Geosyst.*, *2*(12), 1060, doi:10.1029/2001GC000171.

Bellahsen, N. (2005), Dynamics of subduction and plate motion in laboratory experiments: Insights into the "plate tectonics" behavior of the earth, *J. Geophys. Res.*, *110*, B01401, doi:10.1029/2004JB002999.

Billen, M. I. (2008), Modeling the dynamics of subducting slabs, *Annu. Rev. Earth Planet. Sci.*, *36*, 325–356, doi:10.1146/annurev.earth.36.031207.124129.

Capitanio, F. A., G. Morra, and S. Goes (2007), Dynamic models of downgoing plate-buoyancy driven subduction: Subduction motions and energy dissipation, *Earth Planet. Sci. Lett.*, *262*, 284–297, doi:10.1016/j.epsl.2007.07.039.

Capitanio, F. A., G. Morra, and S. Goes (2009), Dynamics of plate bending at the trench and slab-plate coupling, *Geochem. Geophys. Geosyst.*, *10*, Q04002, doi:10.1029/2008GC002348.

Capitanio, F. A., D. R. Stegman, L. N. Moresi, and W. Sharples (2010), Upper plate controls on deep subduction, trench migrations and deformations at convergent margins, *Tectonophysics*, *483*, 80–92, doi:10.1016/j.tecto.2009.08.020.

Capitanio, F. A., C. Faccenna, S. Zlotnik, and D. R. Stegman (2011), Subduction dynamics and the origin of Andean orogeny and the Bolivian orocline, *Nature*, *480*, 83–86, doi:10.1038/nature10596.

Clark, S. R., D. R. Stegman, and R. D. Müller (2008), Episodicity in back-arc tectonic regimes, *Phys. Earth Planet. Inter.*, *171*, 265–279, doi:10.1016/j.pepi.2008.04.012.

Conrad, C. P., and C. Lithgow-Bertelloni (2004), The temporal evolution of plate driving forces: Importance of slab suction versus slab pull during the Cenozoic, *J. Geophys. Res.*, *109*, B10407, doi:10.1029/2004JB002991.

Di Giuseppe, E., J. van Hunen, F. Funiciello, C. Faccenna, and D. Giardini (2008), Slab stiffness control of trench motion: Insights from numerical models, *Geochem. Geophys. Geosyst.*, *9*, Q02014, doi:10.1029/2007GC001776.

Forsyth, D., and S. Uyeda (1975), On the relative importance of the driving forces of plate motion, *Geophys. J. R. Astron. Soc.*, *43*, 163–200.

Funiciello, F., G. Morra, K. Regenauer-Lieb, and D. Giardini (2003), Dynamics of retreating slabs: 1. Insights from two-dimensional numerical experiments, *J. Geophys. Res.*, *108*(B4), 2206, doi:10.1029/2001JB000898.

Funiciello, F., C. Faccenna, and D. Giardini (2004), Role of lateral mantle flow in the evolution of subduction systems: insights from laboratory experiments, *Geophys. J. Int.*, *157*, 1393–1406, doi:10.1111/j.1365-246X.2004.02313.x.

Gerya, T. (2011), Future directions in subduction modeling, *J. Geodyn.*, *52*(5), 344–378, doi:10.1016/j.jog.2011.06.005.

Happel, J., and H. Brenner (1983), *Low Reynolds Number Hydrodynamics: With Special Applications to Particulate Media*, Martinus Nijhoff, The Hague, Netherlands.

Laffaldano, G., E. Di Giuseppe, F. Corbi, F. Funiciello, C. Faccenna, and H.-P. Bunge (2012), Varying mechanical coupling along the Andean margin: Implications for trench curvature, shortening and topography, *Tectonophysics*, *526–529*, 16–23, doi:10.1016/j.tecto.2011.09.014.

Lallemand, S., A. Heuret, and D. Boutelier (2005), On the relationships between slab dip, back-arc stress, upper plate absolute motion, and crustal nature in subduction zones, *Geochem. Geophys. Geosyst.*, *6*, Q09006, doi:10.1029/2005GC000917.

Lallemand, S., A. Heuret, C. Faccenna, and F. Funiciello (2008), Subduction dynamics as revealed by trench migration, *Tectonics*, *27*, TC3014, doi:10.1029/2007TC002212.

Li, C., R. D. van der Hilst, E. R. Engdahl, and S. Burdick (2008), A new global model for P wave speed variations in Earth's mantle, *Geochem. Geophys. Geosyst.*, *9*, Q05018, doi:10.1029/2007GC001806.

Mahadevan, L., R. Bendick, and H. Liang (2010), Why subduction zones are curved, *Tectonics*, *29*, TC6002, doi:10.1029/2010TC002720.

Morra, G., K. Regenauer-Lieb, and D. Giardini (2006), Curvature of oceanic arcs, *Geology*, *34*(10), 877–880, doi:10.1130/G22462.1.

Morra, G., P. Chatelain, P. Tackley, and P. Koumoutsakos (2007), Large scale three-dimensional boundary element simulation of subduction, in *Computational Science–ICCS 2007, Part III*, *Lect. Notes Comp. Sci.*, vol. 4489, pp. 1122–1129, Springer, Berlin.

Morra, G., P. Chatelain, P. Tackley, and P. Koumoutsakos (2009), Earth curvature effects on subduction morphology: Modeling subduction in a spherical setting, *Acta Geotechnica*, *4*, 95–105, doi:10.1007/s11440-008-0060-5.

Morra, G., L. Quevedo, and R. D. Müller (2012), Spherical dynamic models of top-down tectonics, *Geochem. Geophys. Geosyst.*, *13*, Q03005, doi:10.1029/2011GC003843.

OzBench, M., et al. (2008), A model comparison study of large-scale mantle–lithosphere dynamics driven by subduction, *Phys. Earth Planet. Inter.*, *171*(1–4), 224–234, doi:10.1016/j.pepi.2008.08.011.

Pozrikidis, C. (1992), *Boundary Integral and Singularity Methods for Linearized Viscous Flow*, Cambridge Univ. Press, Cambridge, U. K.

Ribe, N. M. (2001), Bending and stretching of thin viscous sheets, *J. Fluid. Mech.*, *433*, 135–160.

Ribe, N. M. (2003), Periodic folding of viscous sheets, *Phys. Rev. E*, *68*, 036305, doi:10.1103/PhysRevE.68.036305.

Ribe, N. M. (2010), Bending mechanics and mode selection in free subduction: A thin-sheet analysis, *Geophys. J. Int.*, *180*, 559–576, doi:10.1111/j.1365-246X.2009.04460.x.

Rodríguez-González, J., A. M. Negredo, and M. I. Billen (2012), The role of the overriding plate thermal state on slab dip variability and on the occurrence of flat subduction, *Geochem. Geophys. Geosyst.*, *13*, Q01002, doi:10.1029/2011GC003859.

Schellart, W. P. (2004), Quantifying the net slab pull force as a driving mechanism for plate tectonics, *Geophys. Res. Lett.*, *31*, L07611, doi:10.1029/2004GL019528.

Schellart, W. P. (2005), Influence of the subducting plate velocity on the geometry of the slab and migration of the subduction hinge, *Earth Planet. Sci. Lett.*, *231*, 197–219, doi:10.1016/j.epsl.2004.12.019.

Schellart, W. P. (2008a), Subduction zone trench migration: Slab driven or overriding-plate-driven?, *Phys. Earth Planet. Inter.*, *170*, 73–88, doi:10.1016/j.pepi.2008.07.040.

Schellart, W. P. (2008b), Kinematics and flow patterns in deep mantle and upper mantle subduction models: Influence of the mantle depth and slab to mantle viscosity ratio, *Geochem. Geophys. Geosyst.*, *9*, Q03014, doi:10.1029/2007GC001656.

Schellart, W. P., J. Freeman, D. R. Stegman, L. Moresi, and D. May (2007), Evolution and diversity of subduction zones

controlled by slab width, *Nature*, *446*, 308–311, doi:10.1038/nature05615.

Schellart, W. P., D. R. Stegman, R. Farrington, J. Freeman, and L. Moresi (2010), Cenozoic tectonics of western North America controlled by evolving width of farallon slab, *Science*, *329*, 316–319, doi:10.1126/science.1190366.

Schmeling, H., et al. (2008), A benchmark comparison of spontaneous subduction models–Towards a free surface, *Phys. Earth Planet. Inter.*, *171*, 198–223, doi:10.1016/j.pepi.2008.06.028.

Sdrolias, M., and R. D. Müller (2006), Controls on back-arc basin formation, *Geochem. Geophys. Geosyst.*, *7*, Q04016, doi:10.1029/2005GC001090.

Stegman, D. R., J. Freeman, W. P. Schellart, L. Moresi, and D. May (2006), Influence of trench width on subduction hinge retreat rates in 3-D models of slab rollback, *Geochem. Geophys. Geosyst.*, *7*, Q03012, doi:10.1029/2005GC001056.

Stegman, D. R., R. Farrington, F. A. Capitanio, and W. P. Schellart (2010a), A regime diagram for subduction styles from 3-d numerical models of free subduction, *Tectonophysics*, *483*, 29–45, doi:10.1016/j.tecto.2009.08.041.

Stegman, D. R., W. P. Schellart, and J. Freeman (2010b), Competing influences of plate width and far-field boundary conditions on trench migration and morphology of subducted slabs in the upper mantle, *Tectonophysics*, *483*, 46–57, doi:10.1016/j.tecto.2009.08.026.

Uyeda, S., and H. Kanamori (1979), Back-arc opening and the mode of subduction, *J. Geophys. Res.*, *84*(B3), 1049–1061, doi:10.1029/JB084iB03p01049.

van Dinther, Y., G. Morra, F. Funiciello, and C. Faccenna (2010), Role of the overriding plate in the subduction process: Insights from numerical models, *Tectonophysics*, *484*, 74–86, doi:10.1016/j.tecto.2009.08.038.

Wu, B., C. P. Conrad, A. Heuret, C. Lithgow-Bertelloni, and S. Lallemand (2008), Influence of the subducting plate velocity on the geometry of the slab and migration of the subduction hinge, *Earth Planet. Sci. Lett.*, *272*, 412–421, doi:10.1016/j.epsl.2008.05.009.

Yamato, P., L. Husson, J. Braun, C. Loiselet, and C. Thieulot (2009), Influence of surrounding plates on 3D subduction dynamics, *Geophys. Res. Lett.*, *36*, L07303, doi:10.1029/2008GL036942.

Zhong, S. (2001), Role of ocean-continent contrast and continental keels on plate motion, net rotation of lithosphere, and the geoid, *J. Geophys. Res.*, *106*(B1), 703–712.

3   Article 2

Butterworth, N. P., Müller, R. D., Quevedo, L., O'Connor, J. M., Hoernle, K., Morra, G., (2014), **Pacific Plate slab pull and intraplate deformation in the early Cenozoic**, *Solid Earth Discussions*, 6, 1–45, doi:10.5194/sed-6-1-2014.

Pacific Plate slab pull and intraplate deformation in the early Cenozoic

Butterworth, N.P.[1], Müller, R.D.[1], Quevedo, L.[1], O'Connor, J.M.[2], Hoernle, K.[3], and Morra, G.[4]

[1]EarthByte Group, School of Geosciences, The University of Sydney, New South Wales, 2006, Australia
[2]GeoZentrum Nordbayern, Erlangen and Alfred Wegener Institute for Polar and Marine Research, Bremerhaven, Germany
[3]GEOMAR Helmholtz Centre for Ocean Research Kiel, Germany
[4]Department of Physics and School of Geosciences, University of Louisiana at Lafayette, 70504, LA, USA

Correspondence to: N. P. Butterworth (nathaniel.butterworth@sydney.edu.au)

Abstract. Large tectonic plates are known to be susceptible to internal deformation, leading to a range of phenomena including intraplate volcanism. However, the space and time dependence of intraplate deformation and its relationship with changing plate boundary configurations, subducting slab geometries, and absolute plate motion is poorly understood. We utilise a buoyancy driven Stokes flow solver, BEM-Earth, to investigate the contribution of subducting slabs through time on Pacific Plate motion and plate-scale deformation, and how this is linked to intraplate volcanism. We produce a series of geodynamic models from 62 to 42 Ma in which the plates are driven by the attached subducting slabs and mantle drag/suction forces. We compare our modelled intraplate deformation history with those types of intraplate volcanism that lack a clear age progression. Our models suggest that changes in Cenozoic subduction zone topology caused intraplate deformation to trigger volcanism along several linear seafloor structures, mostly by reactivation of existing seamount chains, but occasionally creating new volcanic chains on crust weakened by fracture zones and extinct ridges. Around 55 Ma subduction of the Pacific-Izanagi ridge reconfigured the major tectonic forces acting on the plate by replacing ridge push with slab pull along its north-western perimeter, causing lithospheric extension along pre-existing weaknesses. Large scale deformation observed in the models coincides with the seamount chains of Hawaii, Louisville, Tokelau, and Gilbert during our modelled time period of 62 to 42 Ma. We suggest that extensional stresses between 72 and 52 Ma are the likely cause of large parts of the formation of the Gilbert chain and that localised extension between 62 and 42 Ma could cause late-stage volcanism along the Musicians Volcanic Ridges. Our models demonstrate that early Cenozoic changes in Pacific plate driving forces only cause relatively minor changes in Pacific absolute plate motions, and cannot be responsible for the Hawaii-Emperor Bend

(HEB), confirming previous interpretations that the 47 Ma HEB does not reflect an absolute plate motion event.

1 Introduction

The origin of intraplate volcanism without age progression and far away from plate boundaries is poorly understood (Lee and Grand, 2012; Koppers, 2011). Intraplate volcanism can be viewed as being due to hotspots within tectonic plates, which may be caused by a range of processes including mantle plumes, small-scale convection, or lithospheric extension of plates (Ito and van Keken, 2007). In an effort to categorize these phenomena Courtillot et al. (2003) distinguished three categories of hotspots. The first is the classic Wilson-Morgan type mantle plume (Morgan, 1971; Wilson, 1963), a thermal anomaly rising through the mantle due to the density difference between the core-mantle boundary and the surface. These are often long-lived and have a relatively stable source location. The second type is similar, but originates from the bottom of the transition zone, associated with superswells (Koppers et al., 2003; Romanowicz and Gung, 2002), and is comparatively short-lived. The third type (Liu and Stegman, 2012; Ito and van Keken, 2007; Hirano et al., 2006; Koppers et al., 2003) is the most broadly classified hotspot, potentially caused by many factors, and the use of the term hotspot to describe this type of volcanism can be a misnomer. The melting anomaly may not be necessarily hot (Bonatti, 1990) and may not be a singular spot (Sandwell and Fialko, 2004). It has been suggested (Ballmer et al., 2013; Conrad et al., 2011) that shear mantle flow within the asthenosphere mostly explains this type of intraplate volcanism. However, lithospheric extension driven by plate boundary forces, plate motion, and small-scale covection may be causing intraplate volcanism as well (Ballmer et al., 2009; Koppers et al., 2003; Sandwell et al., 1995). Lithospheric cracking due to plate flexure (Hirano et al., 2006) and thermal contraction (Sandwell and Fialko, 2004) is also a possible contributor to surface volcanics. The cracking hypothesis presumes pre-existing partial melt below the surface that may be erupted when stress is applied (Ballmer et al., 2009; Hieronymus and Bercovici, 2000). Intraplate magmatism may occur in conjunction with classic hotspot volcanism, and may be associated with highly strained areas overlapping pre-existing zones of weakness (Davis et al., 2002; Staudigel et al., 1991) or may create new weak zones that give rise to volcanism. Most intraplate volcanism occurs along pre-existing tectonic fabric or around highly stressed lithosphere (Clouard and Gerbault, 2008a).

Here we investigate how intraplate deformation in the oceanic lithosphere may be caused by sub-duction driven plate dynamics, how this deformation might contribute to the occurrence and timing of volcanic melting anomalies, and to what extent intraplate volcanism may leave the lithosphere more susceptible to the passage of future melts (Hillier, 2007), focussing on the Pacific Plate evolution in the early Cenozoic. This time period captures the major global tectonic plate reorganisation between 53–50 Ma (Cande and Stegman, 2011; Whittaker et al., 2007) during a period of

heterogeneous plate tessellation (Morra et al., 2013) whereby the ratio of large to small plates is low. Large plate accelerations have been shown to lead to increased volcanic flux (Hieronymus and Bercovici, 2000; Anderson, 1994), therefore the analysis of the early Cenozoic is a good candidate for a relatively active volcanic period. We analyse changes in plate motion around the Pacific ocean basin by considering slab-pull and mantle drag/suction forces and compare the results with absolute plate reconstructions (Seton et al., 2012; Doubrovine et al., 2012; Chandler et al., 2012; Wessel and Kroenke, 2008) and the occurrence of intraplate volcanics (e.g. Clouard and Bonneville, 2005).

2   Model setup

We apply a novel workflow utilising a Stokes flow solver, BEM-Earth (Quevedo et al., 2012a; Butterworth et al., 2012; Morra et al., 2012, 2007), to analyse the coupled plate-mantle dynamics in the Late Cretaceous and early Cenozoic. Our model is driven by upper mantle slab-pull buoyancy forces and by induced slab-suction from the down-going plates, similar to previous work (Faccenna et al., 2012; Conrad and Lithgow-Bertelloni, 2004, 2002). A BEM-Earth simulation requires a set of rheological isosurfaces (here represented by the lithospheric plates, the core, and the external Earth surface). Each isosurface bounds a homogenous region characterised by an effective density and viscosity. In our models these are defined by the surface location of the Pacific, Izanagi, Farallon, and Kula plates and their attached lithosphere and subducting slabs (Fig. 1).

The location of the plates and subducting slabs, used as an initial model starting condition, are determined using tectonic reconstructions from Seton et al. (2012) as implemented in the GPlates software (Boyden et al., 2011). We use reconstructed topologically closed plate boundaries through time, along with modelled plate lithospheric thickness to produce a three-dimensional representation of the Pacific Plate through time. Oceanic lithosphere thickness is derived from the reconstruction model along with oceanic paleo-age grids with a $1° \times 1°$ resolution (Müller et al., 2013). Ages are input into a half-space cooling model to determine plate thickness, as used previously in BEM-Earth (Morra et al., 2012, Appendix B).

We utilise 10 million years of subduction history, from plate kinematic reconstructions, to provide an estimate of slab material that drives the slab-pull force in BEM-Earth. A 10 million year interval reflects the approximate time for a slab to subduct to the lower mantle and thus represents the portion of the slab contributing to the slab-pull (Billen, 2008). To determine initially subducted slab morphology we advect subducting plates into the mantle using surface plate kinematics based on published plate rotations (Seton et al., 2012) starting 10 Myr before the geodynamic model starting time. The absolute and convergent velocities are determined for each point along the reconstructed subduction zone for each time period (Quevedo et al., 2012b). Absolute motions define the surface rotation of the slab's position and the convergence defines the upper mantle slab sinking rate. The initial dip of the slab does not affect the BEM-Earth simulation (Morra et al., 2012), but rather

having the correct amount of upper mantle slab material (Quevedo et al., 2012b; Billen, 2008; Schellart, 2004) is important for simulating driving forces. Nevertheless, resulting dips for a test case of present day slab material are comparable with Slab1.0 (Hayes et al., 2012, Appendix A). At each reconstructed point, we calculate the volume of the slab driving the model, as the convergence rate times the lithospheric thickness added up in 1 Myr time steps for the 10 Myr prior to the model start time.

The resulting modelled plate consists of a mantle viscosity and density structure that is post-processed to ensure smooth non-overlapping 3-D surfaces. This is required to maintain a consistent isostatic equilibrium between the model isosurfaces (Butterworth et al., 2012; Morra et al., 2012).

Rheology of the plate is defined by an isosurface bounding a region of homogenous density and viscosity (as described in Table 1). The simplified rheology structure is free to deform viscously, and is a fair representation for modelling plate-scale lithospheric processes (Li and Ribe, 2012; Capitanio et al., 2010). Each subducting plate is embedded in a homogenous mantle fluid surrounded by an adaptive external surface. A mantle with no viscosity layering simplifies our model, however the role of mantle layering influences the trench morphology (Morra et al., 2012) but would not affect the plate motions and intraplate deformation.

Resolution of the model is determined by the number of triangular elements (panels) making up each rheological isosurface, which is $\sim 50\,\mathrm{km}$. Evolution of the model is driven by the negative buoyancy of the already-subducted lithosphere. As no lithosphere is being replenished at the mid ocean ridges, we only run the model for a few million years at a time to obtain the intraplate deformation and velocities of the plates. The tapered lithospheric thickness at the ridges of the model isosurfaces prompts a ridge-push force to contribute to plate motion, however, the force is diminished by a "surface contact layer" (Butterworth et al., 2012; Morra et al., 2012). The contact layer keeps the plates in isostatic equilibrium by preventing the slab from detaching from the external Earth surface boundary and sinking vertically; rather the subducting plate advances in a more realistic fashion. There are several methods for providing this balancing buoyancy force in numerical models (Ribe, 2010; Stegman et al., 2010; Morra et al., 2007). Here we use a "lubrication layer" method, where the Earth surface boundary is described as an adaptive surface, whose dynamic behaviour is controlled partially by the distance between the model isosurfaces. The ridge-push force contributes less than 10 % (Lithgow-Bertelloni and Richards, 1998) to forces driving plate motions, in BEM-Earth models we find this force contributes less than 5 % due to the contact layer overwhelming the interaction (Butterworth et al., 2012).

2.1 Plate deformation

We extend the work of Clouard and Gerbault (2008a) into a 3-D spherical domain, where we examine intraplate deformation driven by plate-scale tectonics and its relationship to volcanism. However, we use a dynamic simulation with no external velocity forcing. The natural strains, ϵ, are calculated

Table 1. Reference model parameters.

Parameter	Symbol	Non-dimensional value	Natural value	Units
Earth Radius	r_E	1	6371	km
Mantle Viscosity	η_m	1	10^{21}	Pa s
Mantle Density	ρ_m	50	3300	$\mathrm{kg\,m^{-3}}$
Slab Viscosity	η_s	$100 \times \eta_\mathrm{m}$	$100 \times \eta_\mathrm{m}$	Pa s
Slab Density	ρ_s	80	3330	$\mathrm{kg\,m^{-3}}$
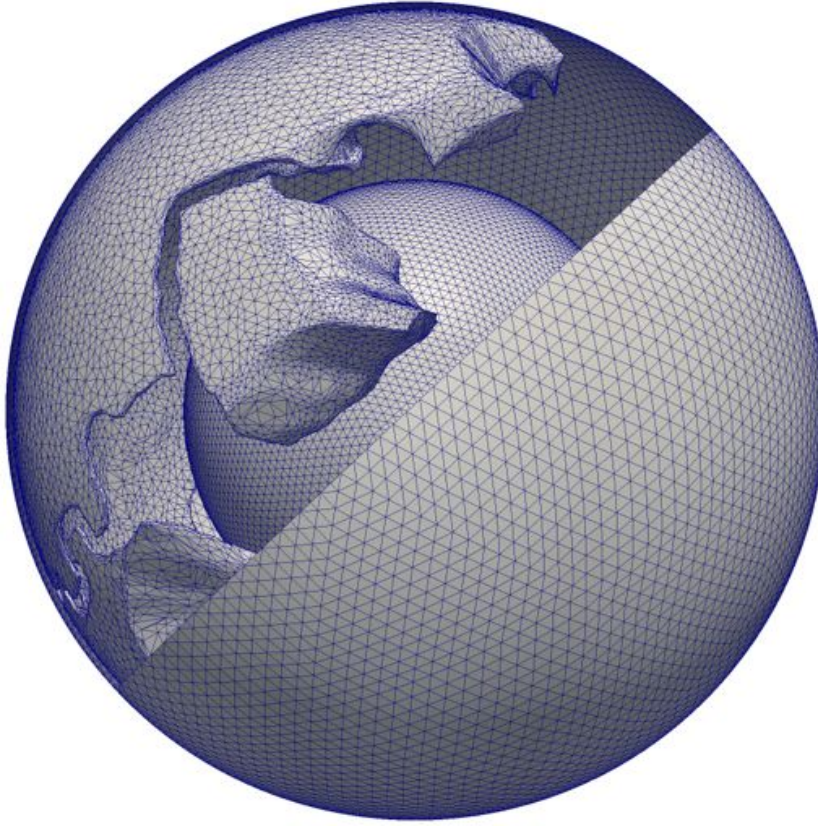
Fig. 1. The initial starting model used for input into BEM-Earth. Each isosurface bounds a region of discrete viscosity and density as described in Table 1. The external Earth surface has been peeled back to show the other core and plate isosurfaces. The modelled plates, here at 42 Ma, are the Kula, Farallon, and Pacific. The blue mesh is indicative of model resolution and shows the panels that are free to deform.

for each model panel through time using $\epsilon = \frac{L}{\ell} - 1$, where L and ℓ are the original and final lengths of model panels respectively. Principal axis stresses are then computed from the natural strains and strain rosette gauge transformation tensors. Finally, the von Mises Criterion, which is an effective or equivalent stress that can be used as an indication for likely regions of deformation (Gueydan et al.,

2008), is defined in three dimensions as $\sigma_e = \frac{1}{\sqrt{2}}\sqrt{(\sigma_1 - \sigma_2)^2 + (\sigma_2 - \sigma_3)^2 + (\sigma_3 - \sigma_1)^2}$, where σ is the principal stress in each of the 3 axes (Boresi and Schmidt, 2003).

The plate with a simplified rheology is free to deform viscously due to forces driving the natural evolution and transmission of stresses in the plate. Deformation is determined over a phase of steady model evolution after a period of initialisation. This delay in measurement allows the model to equilibrate. However, results are found to be similar when the deformation is measured early or later in the simulation. Pre-existing zones of weakness (e.g. fracture zones) likely act as conduits for melting anomalies (Davis et al., 2002), but plate-scale deformation due to subduction processes may provide the stresses required to promote volcanics. Volcanism is not expressed in the models, but we use ^{40}Ar/^{39}Ar dates for the relatively few samples available from seafloor volcanism edifices, to see if a link can be established in some places between subduction-driven plate deformation and spatio-temporal localisation of hotspot melting anomalies.

3   Model results

We run four subduction driven models which start with surface reconstructions at 62, 52, 47, and 42 Ma and include the previous 10 million years of subduction material as an initial condition. The resulting model deformation is correlated with age-dated volcanic structures, and the model kinematics are compared with alternative plate model reconstructions.

3.1   62 Ma reconstruction

The reconstructed Pacific Plate at 62 Ma (Fig. 2) only has one subducting slab mechanically attached to it, along the East Junction subduction zone, located to the north of Australia between the Tethys and Panthalassa (Seton and Müller, 2008). Slab-pull and basal drag (due to induced slab-suction) are the only significant model driving forces (Morra et al., 2012; Butterworth et al., 2012). At this time, the pull due to Junction slab attached to the Pacific only originates from $\sim 4\,\%$ global slab material. The subducting plates, Izanagi, Kula, and Farallon, that surround the Pacific have subduction zones with over 70 % of global slab material driving them. Reconstructed Pacific Plate velocities from Seton et al. (2012) show the plate heading toward the north-west (303°). The Doubrovine et al. (2012) reconstructions have the Pacific moving generally toward the north (15°). The Izanagi, Kula, and Farallon plates maintain the dominant subducting slabs around the Pacific. The direction of movement of the modelled Pacific (287°) is more inline with those predicted by the Seton et al. (2012) reconstructions. We observe the deformation on the plate at 62 Ma to be more contrasting across the plate with a large zone of focussed deformation running from the centre of the Pacific to the north-west intersection with the Izanagi plate.

3.2 52 Ma reconstruction

Between 62 and 52 Ma the Pacific Plate model undergoes a relatively major change in its kinematics and topology (Fig. 3). The Izanagi plate is now fully subducted and its subducting slab is fully coupled with the north-west portion of the Pacific Plate. Subducting slabs attached to the Pacific Plate now account for $\sim 24\,\%$ of global material being subducted. The Farallon and Kula plates have down-going material accounting for $\sim 24\,\%$ and $\sim 12\,\%$ of global material respectively. This induces high strain just behind the subduction zone in the down-going Pacific Plate. This high-strain region feeds into the same north-west trending feature seen at 62 Ma that tapers off toward the centre of the plate. There are also smaller zones of high-strain scattered around the plate. The modelled velocities show the Pacific moving westerly (280°), and rotating clockwise. As subduction is now the major driver of the Pacific Plate, the model velocity vectors are more consistent with the direction of the velocities of Seton et al. (2012) (293°). In the model the velocities are exaggerated close to the subduction zone. The Doubrovine et al. (2012) velocities have increased in magnitude and show the Pacific moving more westerly (337°), similar to the Seton et al. (2012) reconstructions during this epoch. Doubrovine et al. (2012) reconstructions favour a more northward trend to our model velocities and the Seton et al. (2012) reconstructions.

3.3 47 Ma reconstruction

The Pacific Plate approaches periods of rapid change in the Seton et al. (2012) reconstruction between 52 and 42 Ma. We run a model in the intervening period at 47 Ma to capture this change. At this time (Fig. 4) the major subduction zone attached to the Pacific is only along the west and north-west region, now accounting for $\sim 15\,\%$ of global slab material, topologically similar to the 52 Ma model. The other major dynamic influences come from the Kula and Farallon plates and their attached subducting slabs, which account for $\sim 16\,\%$ and $\sim 33\,\%$ of global slab material respectively. The Pacific Plate in our model is now moving in a predominantly westerly direction (283°) and has slowed corresponding with a decrease in assumed depth of initial slab material. The large subducting slab attached to the Pacific Plate is the main driver of plate motion in this epoch. The model and reconstructed velocity vectors of Seton et al. (2012) (288°) agree well overall. Doubrovine et al. (2012) plate velocities trend more to the north (341°) and the magnitude has decreased significantly since 52 Ma. Deformation in the plate has similar style to the 52 Ma model, with patches of high-strain appearing over the plate or propagating from the edges; however, the large region of deformation propagating from the north-west subduction zone has been greatly dissipated.

3.4 42 Ma reconstruction

The modelled Pacific at 42 Ma (Fig. 5) is kinematically and topologically similar to the 47 Ma model. The same subduction zones continue to drive the Pacific as from the 47 Ma model epoch. The model

direction vectors (288°) have the same north-west trend as the Seton et al. (2012) reconstructed plate motion vectors (294°). Doubrovine et al. (2012) reconstructions show the Pacific undergoing an apparent motion change, trending from north at 47 Ma to now north-west (310°). There is a correspondence between the two kinematic reconstructions and our model, with all models bearing predominately toward the west and north. The areas of high-strain are maintained in similar locations to 47 Ma.

4 Discussion

4.1 Kinematic vs. geodynamic model plate motions

From Seton et al. (2012) reconstructions, there are abrupt motion changes in the Pacific Plate between 60 and 59 Ma, 56 and 55 Ma, 50 and 49 Ma, and also between 48 and 47 Ma. These are captured between the 62 Ma and 52 Ma, and the 52 Ma and 47 Ma models respectively (Figs. 2–4). However, our models cannot capture changes over time periods in between model runs.

The plates in our geodynamic model are primarily driven by slab material pulling on a given attached plate. Contributions of induced mantle flow, expressed as a suction force, are secondary to this, but can still be appreciable, depending on the location of the slabs relative to the plates (Morra et al., 2012). The slab-suction force is driven from the slabs attached to the down-going plates, but we do not model the effect of tractions that may be induced by other density heterogeneities in the mantle (Ricard et al., 1993). The role of slab-suction is most evident in the motion of the 62 Ma Pacific, where the plate has no major subduction zones, but continues to move towards the north-west as predicted by kinematic reconstructions (Seton et al., 2012). At times when the large subduction zones bound the Pacific Plate, motion in our model is well constrained and our velocity directions are consistent with kinematically derived plate motions of Seton et al. (2012). However, the magnitudes of our modelled velocities are unrealistically amplified near major subduction trenches as that portion of the slab begins to rapidly descend, as such we normalise the vectors to the maximum velocity predicted by the kinematic reconstructions (Morra et al., 2012).

The correspondence between the model velocities favouring Seton et al. (2012) over Doubrovine et al. (2012) derived velocities, are in-part because the Doubrovine et al. (2012) plate model has been constructed to include Pacific hotspots that mimic the Hawaiian-Emperor bend. However, because this hotspot track is uniquely related to mantle flow (Sharp and Clague, 2006), perhaps involving ridge-plume capture (Tarduno et al., 2009), we find our subduction driven model better fits Seton et al. (2012) (based on the hotspot moving reference frame of O'Neill et al., 2005) reconstructions.

Furthermore, between 83.5 and 45 Ma the Seton et al. (2012) and Doubrovine et al. (2012) plate motions are constrained using different plate circuits. Between 50–70 Ma there is a large transition in the absolute plate motion of the Doubrovine et al. (2012) model attributed to the fast motion of the Indian plate. This could be a point of model velocity mismatch, as our models do not include
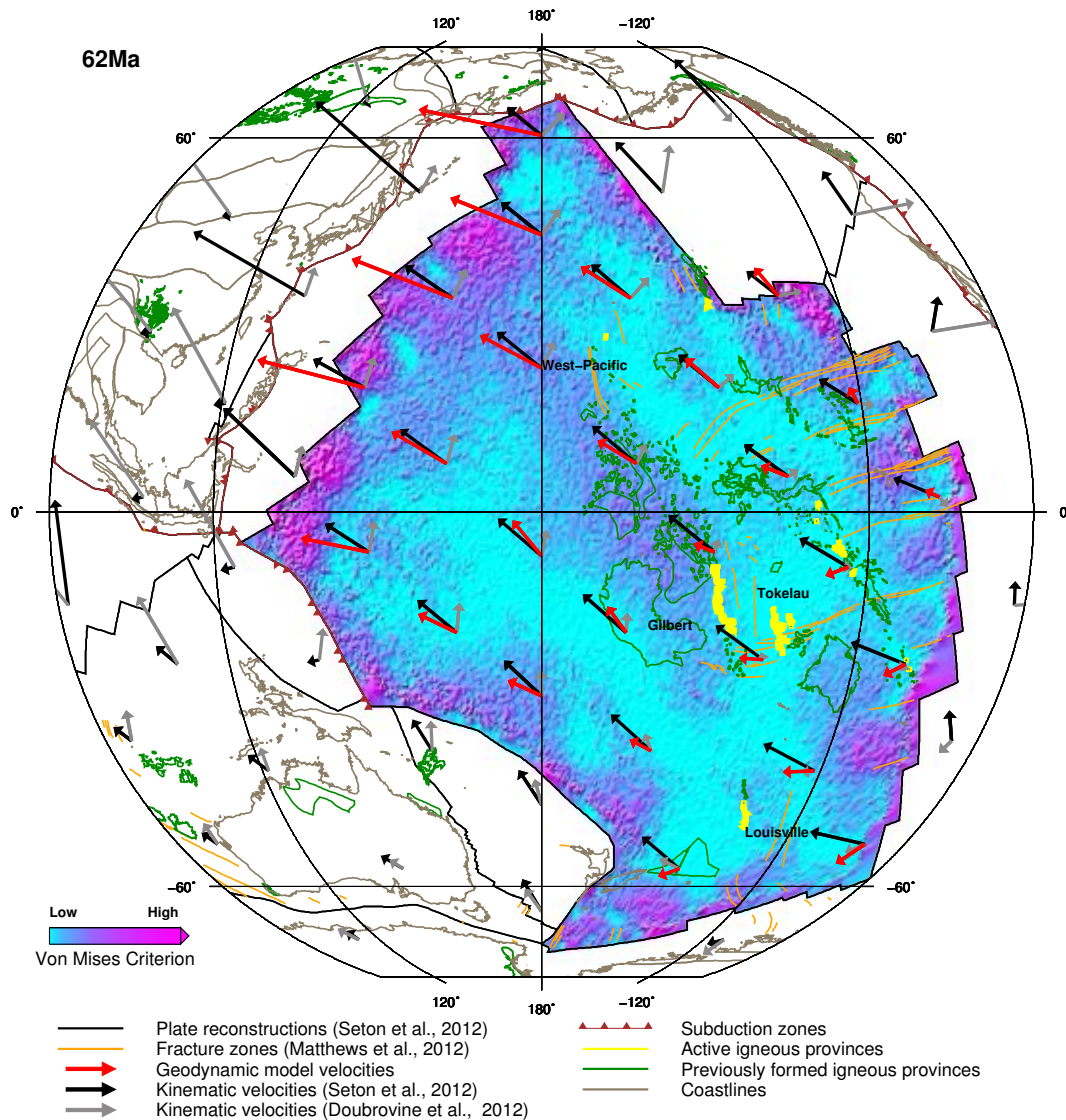
Fig. 2. Pacific Plate reconstruction at 62 Ma. Paleo-plate reconstructed positions (Seton et al., 2012) are outlined in black, with attached subduction zones in red. Velocities of kinematic plate reconstruction models are shown by the black (Seton et al., 2012) and grey arrows (Doubrovine et al., 2012). Our subduction model derived velocity vectors are shown by red arrows. The yellow features are the reconstructed positions of age-dated igneous provinces that have appeared in the 10 Myr preceding the model (see discussion for references). Existing igneous structures are outlined in green. Significant locations are labelled. Orange lines are the reconstructed fracture zone locations (Matthews et al., 2011). The brown outlines represent the reconstructed positions of the present day coastlines. The aqua to magenta logarithmic colour scale represents the non-dimensional von Mises Criterion of our model, with aqua representing minimal plate deformation and magenta representing the maximal deformation. The smooth, homogenous style of deformation is at the borders of divergent and passive margins is likely due to numerical noise.

plates far from the Pacific.

To further constrain the reliability of our plate motions we compare the Euler poles of the Pacific Plate for each model time with four different plate reconstructions along with our subduction driven BEM-Earth model (Fig. 6). The location of the Euler pole quantifies the direction of rotation for
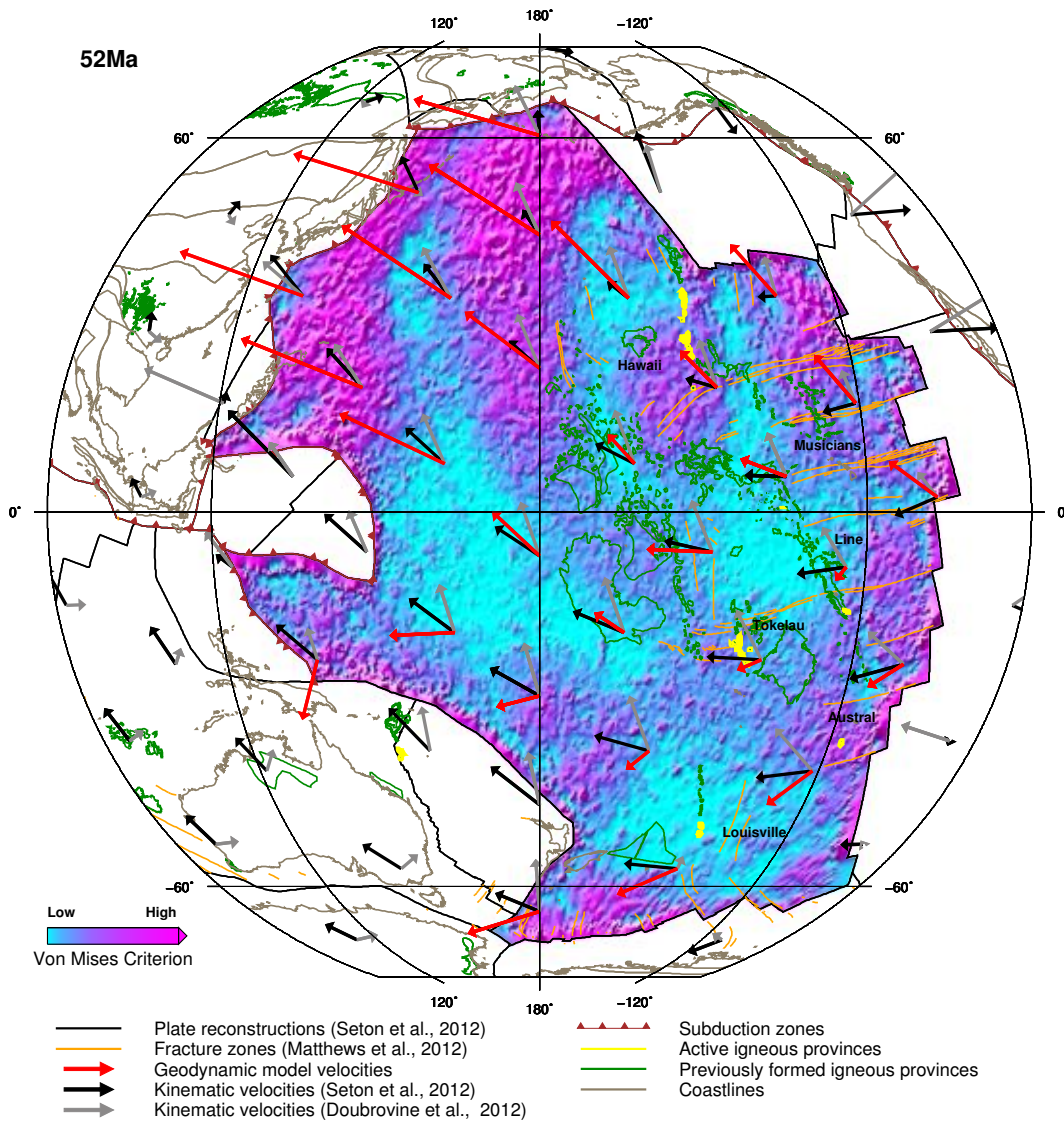
Fig. 3. Same as Fig. 2 but for the Pacific Plate reconstruction at 52 Ma.

a given plate and thus provides a good measure of correspondence between alternate models. For the time period modelled here (62–42 Ma) Wessel and Kroenke (2008) determines plate motions by assuming fixed hotspots in the Pacific. They determine Pacific rotations directly from an absolute reference frame. Alternatively Doubrovine et al. (2012) applies a moving Pacific, Atlantic, and Indian hotspot model, with rotations of the Pacific linked through a plate circuit to the absolute reference frame. Euler poles determined from Chandler et al. (2012) and Seton et al. (2012) are strikingly similar in absolute motion through time as both models rely on a moving Indian/Atlantic hotspot reference frame (O'Neill et al., 2005), and both link their plate circuits to Africa. They deviate from each other after 47 Ma as Chandler et al. (2012) interprets the rapid change in Pacific
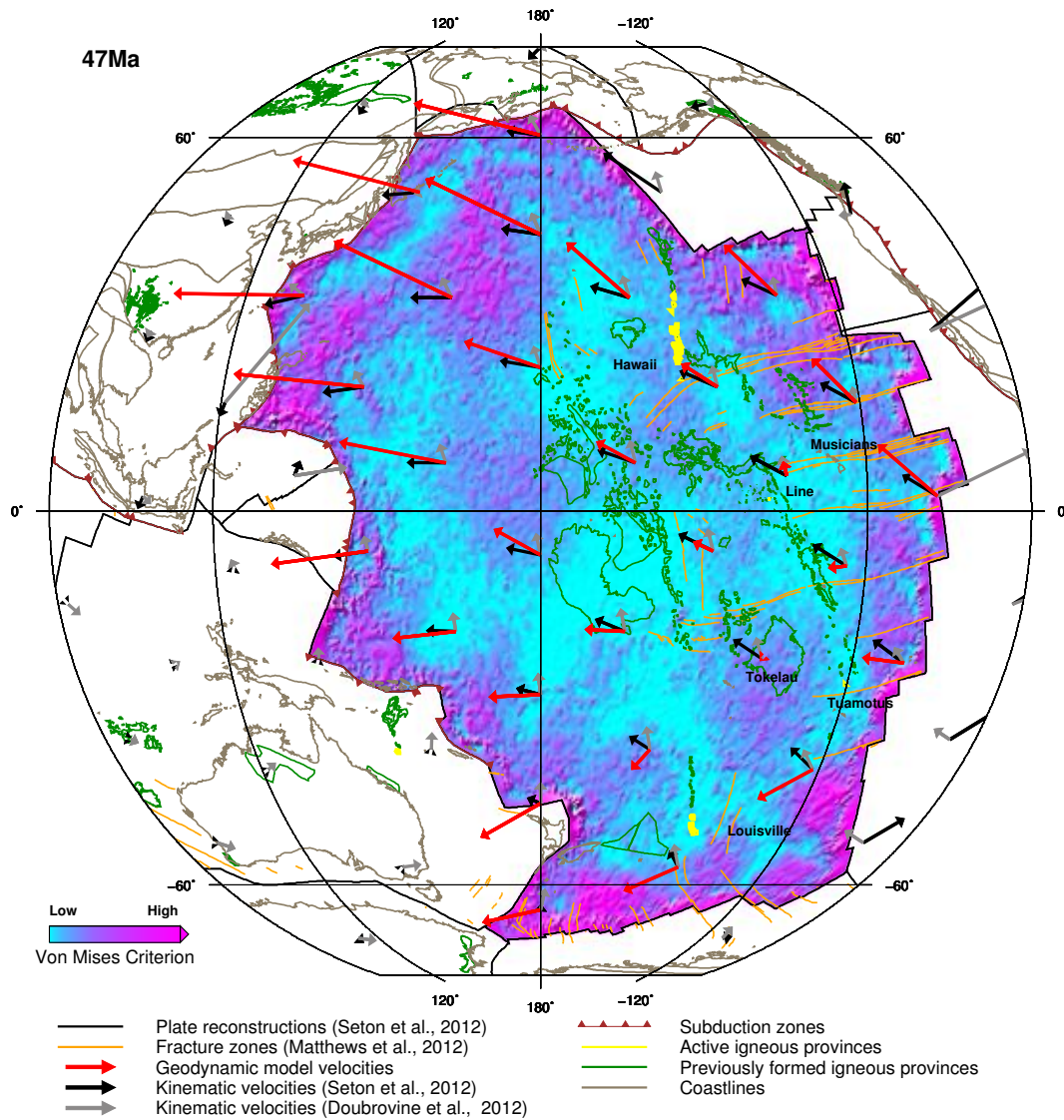
Fig. 4. Same as Fig. 2 but for the Pacific Plate reconstruction at 47 Ma.

plate motion expressed in the Hawaiian-Emperor bend as being due to a slowdown in drift of the Hawaiian plume.

Each of the four plate reconstruction models sustain a sharp transition between 52 and 62 Ma, indicating a significant motion change in the Pacific. The poles associated with the dynamically modelled Pacific also capture this motion change, revealing that the subducting slab topology is congruent in influencing plate motion changes. The disparity of the Wessel and Kroenke (2008) poles from the other models highlights the impact of including fixed Pacific hotspots in plate reconstructions without considering differential hotspot motion or seamounts offset from hotspot locations. Our dynamically modelled motions of the Pacific Plate, which are agnostic of mantle plumes and
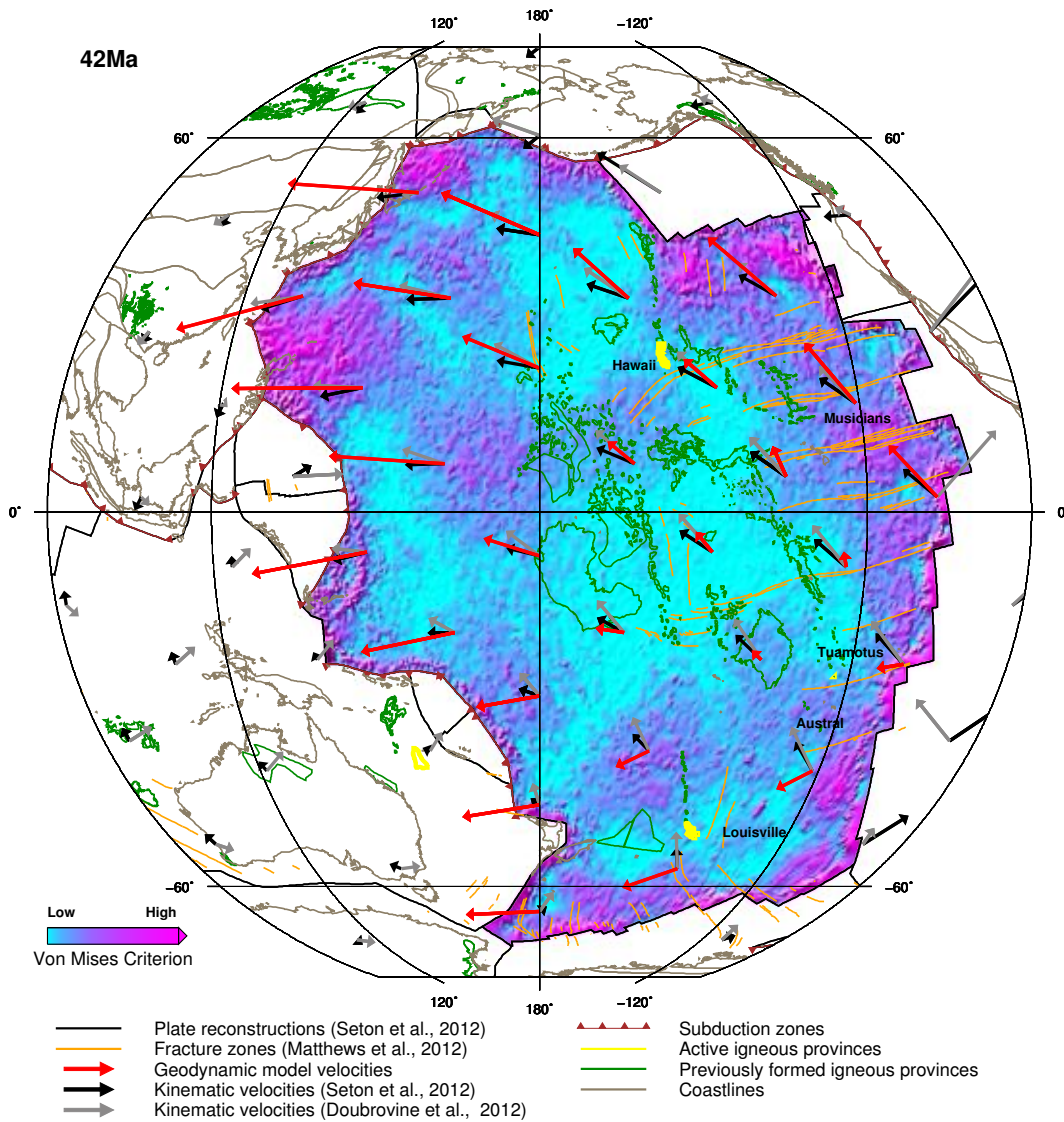
Fig. 5. Same as Fig. 2 but for the Pacific Plate reconstruction at 42 Ma.

plume drift, are reliant on the approach used for a given plate reconstruction methodology, as the plate model used determines the amount and location of slab material in the upper mantle. The overall good correspondence between the absolute plate velocities of the reconstruction used to build our simulation (Seton et al., 2012) and the slab driven model prediction provides the insight that a combined relative/absolute plate motion model built without relying on Pacific hotspot tracks, and particularly not the Hawaiian-Emperor chain, predicts kinematic absolute Pacific plate velocities that are plausible based on a subduction-driven dynamic model. This is consistent with the view that the Hawaiian-Emperor bend does not only reflect a change in absolute (or relative) plate motion, but that it is also due to the slowdown of the drift of the Hawaiian plume (Tarduno, 2007; Tarduno et al.,
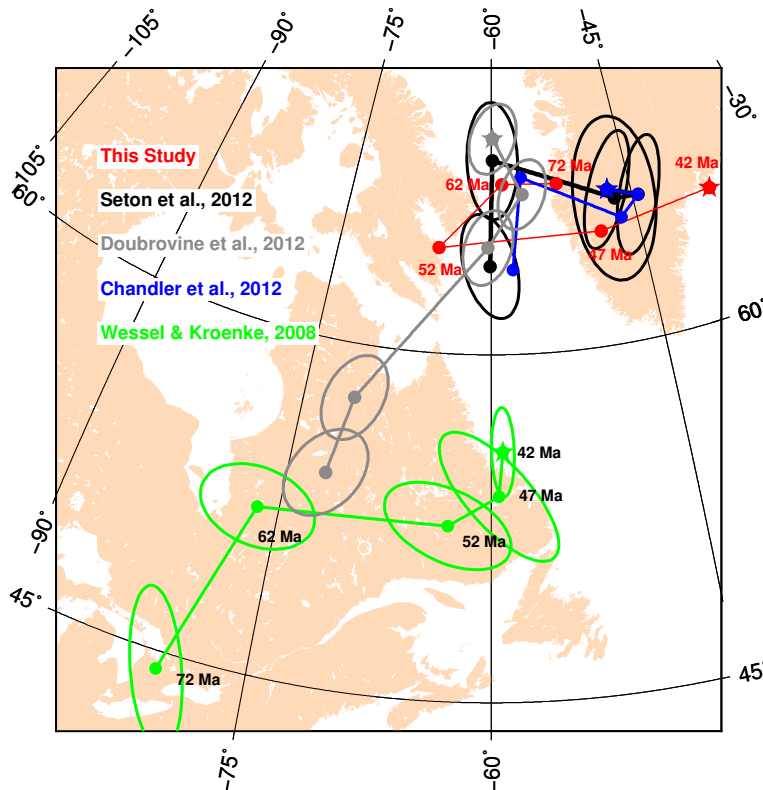
Fig. 6. Finite rotation Euler pole locations for the Pacific Plate at each of the model times. The five different models are coloured as in the legend. Stars represent the 42 Ma Euler poles and progressive points are the 47, 52, 62, and 72 Ma poles, these are only labelled for our model and the Wessel and Kroenke (2008) reconstructions for clarity. Present day continents are overlain in peach for reference. The BEM-Earth Euler poles are the addition of the finite poles from Seton et al. (2012) and the stage rotations of each model run. Projected error ellipses are determined from each source's published covariance matrix.

2009).

4.2   Subduction zone topologies driving plate deformation

Location and amount of slab material along subduction zones determines the direction and magnitude of plate motion. Tectonic plates do not move completely rigidly but are free to deform according to the interaction and relative contribution of the slab-pull force, induced suction forces, and basal drag forces over the entire plate. In our models magnitudes of the non-dimensional deformation, represented by the von Mises, are derived from the change in length of the plate panels and the interval of time steps that the model is run for. The higher the von Mises the more likely the plate will yield, in reality this will occur dependent on the rheological properties of the lithosphere.

At 62 Ma there is an absence of any major subduction zones driving Pacific Plate motion and deformation. For this modelled time significant deformation is due to nearby slabs (Kula, Izanagi,

Farallon) being strongly coupled to the plate through slab suction. The flow cell set-up by the Izanagi slab is dominant in controlling Pacific Plate kinematics at this time, because the trench-perpendicular length of the Izangai plate is relatively small (Morra et al., 2012). Induced flow in the model results in minimal surface uplift, so radial stress is not apparent. Instead, deformation is caused by induced flow, dragging sections of the plate with spatially varying tractions. As a result, deformation due to induced upwellings is minimally constrained. Smooth, homogenous style of coherent deformation is generally observed at the borders of divergent and passive margins in the models partly due to convection cells acting on the intervening space between plate boundaries (Butterworth et al., 2012).

There was a major tectonic plate reorganisation between 53–50 Ma (Whittaker et al., 2007; Cande and Stegman, 2011). This abrupt direction change has been linked to the subduction of the Pacific-Izanagi ridge (Whittaker et al., 2007). This tectonic reconfiguration is captured between the 62 and 52 Ma models. Between these times there is a significant increase in deformation across the entire Pacific Plate (Figs. 2 and 3). By 52 Ma the Pacific-Izanagi ridge is fully subducted and the volume of slab material controlling the pull force on the Pacific is at the maximum of all the epochs modelled. The model velocities capture a significant change in absolute plate motion during this time interval. The 52 Ma model reflects a peak amplitude in total lithospheric deformation over the Plate compared to the other modelled times. However, we do not see a marked increase in volcanic flux at this time (Hillier, 2007; Clouard and Bonneville, 2005). This is in contrast to an expected increase in volcanism during such a period of rapid plate motion change (Anderson, 1994; Hieronymus and Bercovici, 2000).

Between 52 and 47 Ma the Junction Plate in the western Pacific has fully subducted leaving a smoother plate boundary between the Pacific and Philippine Plates. In this time period the amount of total global slab material directly pulling the Pacific Plate has reduced from $\sim 24\,\%$ to $\sim 15\,\%$. Changing motions in the Pacific during the Cenozoic have previously been shown to be driven by the variations in slab-pull (Faccenna et al., 2012) and slab-suction (Conrad and Lithgow-Bertelloni, 2004). And, asymmetric distribution of slab material along the subduction zones partially controls the location of intraplate deformation (Clouard and Gerbault, 2008a).

The plate topology, subduction zone, and slab material configurations driving the 47 and 42 Ma models are relatively similar. In turn, the patterns of deformation across the Pacific Plate are similar.

4.3   Plate deformation correlated with magmatic events and evidence for non-plume related intraplate volcanism

A variety of age-dated volcanic structures formed across the Pacific Plate between 72 and 42 Ma (Fig. 7), which can be compared with the deformation predicted by our models. The complexity and abundance of seafloor features are highlighted by the use of the vertical gravity gradient in Fig. 7, however seafloor structures that have been sampled and dated to this time period are scarce (Hillier, 2007). Plate deformation does not necessarily generate volcanism, just as volcanism can take place

without plate deformation, e.g. small-scale convection that is not directly related to deformation. Although plate deformation may induce upwelling and decompression melting, the plate deformation (cracking) can also serve to simply facilitate the rise of melts that already exist or are produced by other mechanisms.

The northernmost area of Pacific intraplate volcanism in Fig. 7 are the Emperor Seamounts (Duncan and Keller, 2004), a product of plume-plate interaction (Sharp and Clague, 2006). However, throughout its formation history, subduction driven plate deformation is seen to overlap with the chain. A region of high-strain, between 15–30° N, encompasses the southern part of the Emperor chain in the 52 Ma model run (Fig. 3). Rather than produce new volcanism, deformation induced during the 52 Ma time period may impose small stress-bends in the pre-existing linear chain (Koppers and Staudigel, 2005). The 47 Ma model (Fig. 4) continues to show plate-strain, with a diminished magnitude, overlapping with the Hawaiian-Emperor chain. Volcanism is active during the 42 Ma model time period in Hawaii (Sharp and Clague, 2006) and the chain continues to show age-progressive volcanism after the bend at 47 Ma. But the 42 Ma model shows minimal plate deformation correlated with the location of the chain.

In the north-east of the Pacific Plate lies the Musicians Volcanic Ridges, that have active volcanism coeval with our model run epochs, between 72 and 42 Ma. This may be considered late-stage volcanism occurring after the initial formation from a hotspot interacting with a spreading ridge from 96 to 75 Ma (Pringle, 1993; Kopp et al., 2003). In the 62 and 52 Ma models in the Musicians seamounts there is increased deformation indicated by the model (Fig. 3). The 47 and 42 Ma models continue to show deformation around the Musicians ridge.

The Louisville seamount chain in the South Pacific documents a history of volcanism from 82 to 42 Ma (Koppers et al., 2010, 2011), associated with classical hotspot activity (Koppers et al., 2004). There is plate deformation toward the north of the chain in the 42 Ma model (Fig. 5). However, this deformation is likely not the main driver of magmatism, but would aide in decompressional melting of the hotspot material.

The Austral seamounts show volcanism between 62 and 52 Ma (Clouard and Bonneville, 2005). This region of seamounts is influenced by many hotspots (Clouard and Bonneville, 2005) and also shows correlation with highly deformed lithosphere at 52 Ma (Fig. 3). This suggests correlation between hotspots located under lithosphere weakened by previous volcanism (Hillier, 2007).

In the western Pacific (Fig. 7) there are several clusters of seamounts that together encompass the Western Pacific Seamount Province. This province shows weak age-progression in some areas (Ito and van Keken, 2007), suggesting some formation mechanism other than a plume. Koppers et al. (2003) show that there are in fact some age progressions in this region, but overall is a rather complex area with a spike in volcanism lasting until ∼ 70 Ma. This province includes the Japanese Seamounts (Ozima et al., 1983) in the north, the Mid-Pacific Mountains (Pringle, 1993) that show weak age progression in the central region, and the Magellan seamounts to the south. Between 82

and 62 Ma there are only four Japanese seamounts displaying volcanism, with no mapped features correlating with our modelled plate-strain.

The Line Islands in the central Pacific are considered to have formed through volcanism due to lithospheric extension (Davis et al., 2002). Their temporal appearance between 80 and 68 Ma is not correlated with subduction driven deformation observed in the 62 Ma model. The Line Islands show reduced volcanism after this time until 55 Ma without any deforming regions coinciding with their formation. The lack of coincidence between subduction driven deformation and Line Islands volcanism, suggest the magmatism is influenced by another process. Lithospheric extension in this region is possibly related to the upwarping of the Superswell in the eastern South Pacific (Davis et al., 2002).

The initial formation of the Gilbert Ridge can be extended back in time along the Marshall Islands to around 100 Ma (Konter et al., 2008; Koppers et al., 2003). Basement near the ridge was likely preconditioned to volcanism (Koppers et al., 2007) because of the emplacement of volcanic sills during the formation of the Ontong-Java and Hikurangi Plateaus around 125 Ma. The location of the Gilbert chain follows a likely zone of weakness extending north from the Manahiki-Chizca ridge, and running parallel to existing fracture zones (Fig. 2). The Gilbert ridge has been shown to have poor age progression and also shows signs of stress bends at times after formation (Koppers et al., 2007). Volcanism is expressed from 72 to 62 Ma at the Gilbert ridge and later at the Tuvalu-Ellice and Samoan seamount chain (Koppers and Staudigel, 2005). This chain trends and extends in the same north-west direction as the zone of high-strain banding in the central Pacific seen in Fig. 2. It has been shown that seamount chains are generally aligned with the direction of the most tensile principal tectonic stress (Hieronymus and Bercovici, 2000). The modelled Pacific Plate is experiencing tensional deformation along a zone aligned with the orientation of this feature (Fig. 2). The timing of the modelled lithospheric deformation correlates with the formation age of 67 Ma (Koppers and Staudigel, 2005), with continued stress likely influencing a long slow stress-bend after the Gilbert chain's formation. Deformation of the Pacific lithosphere overprinting pre-existing weaknesses seems to have been significant enough to activate the Gilbert chain around this time. Melt material may have already existed in the upper-mantle from the events around 100 Ma, only requiring the changing tectonic stresses, incited by the subducting Izangi slab, to initiate surface volcanism.

The Tokelau seamounts and Phoenix Islands are formed between 72 and 62 Ma in the eastern Pacific (Koppers and Staudigel, 2005), away from any significant tectonic deformation. The Tokelau seamounts are volcanically active between the 62 and 47 Ma models, correlating with a well-defined region of high-strain (Figs. 3–5). Formation of these structures are likely influenced by lithospheric extension (Koppers and Staudigel, 2005) on crust weakened by nearby fracture zones.

The Tarava seamounts become active for the 42 Ma model and are thought to have formed from a hotspot influenced by lithospheric stress (Clouard et al., 2003). This is consistent with the re-

gional deformed area overlapping the location of the reconstructed sample location (Fig. 5). An unknown source mechanism has produced volcanic activity along the poorly sampled and dated nearby Tuamotus seamounts, around 40–50 Ma, visible in the the 47 Ma and 42 Ma models (Figs. 4 and 5). There is minimal correlation between modelled plate deformation and the formation of these seamounts.

It has previously been shown that present day subduction zone forces on the Pacific Plate lead to internal deformation (Clouard and Gerbault, 2008a,b). Extensional mechanisms and lithospheric thickness variations can contribute to enhanced volcanism on ridges and hotspots, but neither mechanism is likely the sole source of seamount chains (Pilger, 2008). Lithospheric weaknesses (e.g. fracture zones, pre-existing magmatism) that override a source of melt material, possibly derived from mantle plumes too weak to penetrate the surface, may be perturbed by tectonic stresses due to plate motion changes, inturn exciting surface eruption. Age-dated Late Cretaceous and early Cenozoic seafloor structures across the Pacific show signs of Pacific-wide plate deformation. Intraplate volcanism sampled across the Pacific is partially indicative of a proposed global reorganisation (Whittaker et al., 2007; Cande and Stegman, 2011) between about 62 and 47 Ma and may be considered as a proxy for stress on the plate (Clouard and Gerbault, 2008a). Because the stress state of the lithosphere, plate deformation, and subsequent volcanism are inherently mixed, but are not necessarily mutually exclusive, it is difficult to extract a definitive location of volcanism based on stress or deformation alone, or vice-versa. This is even more so where there is pre-existing hotspot volcanism in reactivated seamount chains. However, deformation predicted by our models gives an indication of potential sites of intraplate volcanism that are related to anomalously stressed lithosphere.

4.4   Modelled lithospheric structure influencing plate deformation

There is competition between thermal contraction that strengthens the lithosphere during cooling as the lithosphere gets older and thicker (Koppers and Watts, 2010) and load-induced stress relaxation that weakens it. However, it is found that plate thickness seems to have no noticeable effect on plate deformation, driven by large-scale convection in our models, regardless of the tectonic configuration. This is likely because the plate rheology is homogenous and there is no heat flow in the model that would otherwise create a weakened crust (Shaw and Lin, 1996). Also the thickness variations are comparatively small to the major convective cells in the model domain.

The rheology of the modelled subducting plate and the mantle will influence the deformation of the plate. In the models, decreasing the lithosphere viscosity to $50 \times \eta_{\mathrm{m}}$ or increasing it to $200 \times \eta_{\mathrm{m}}$ will make the model evolve slower or faster, respectively. However, regions of deformation remain broadly consistent between models with a different viscosity lithosphere. Intraplate deformation resulting from the stresses imposed by the subduction and mantle drag/suction forces are a robust prediction of the model. Whether the stresses are sufficient to cause intraplate deformation depends
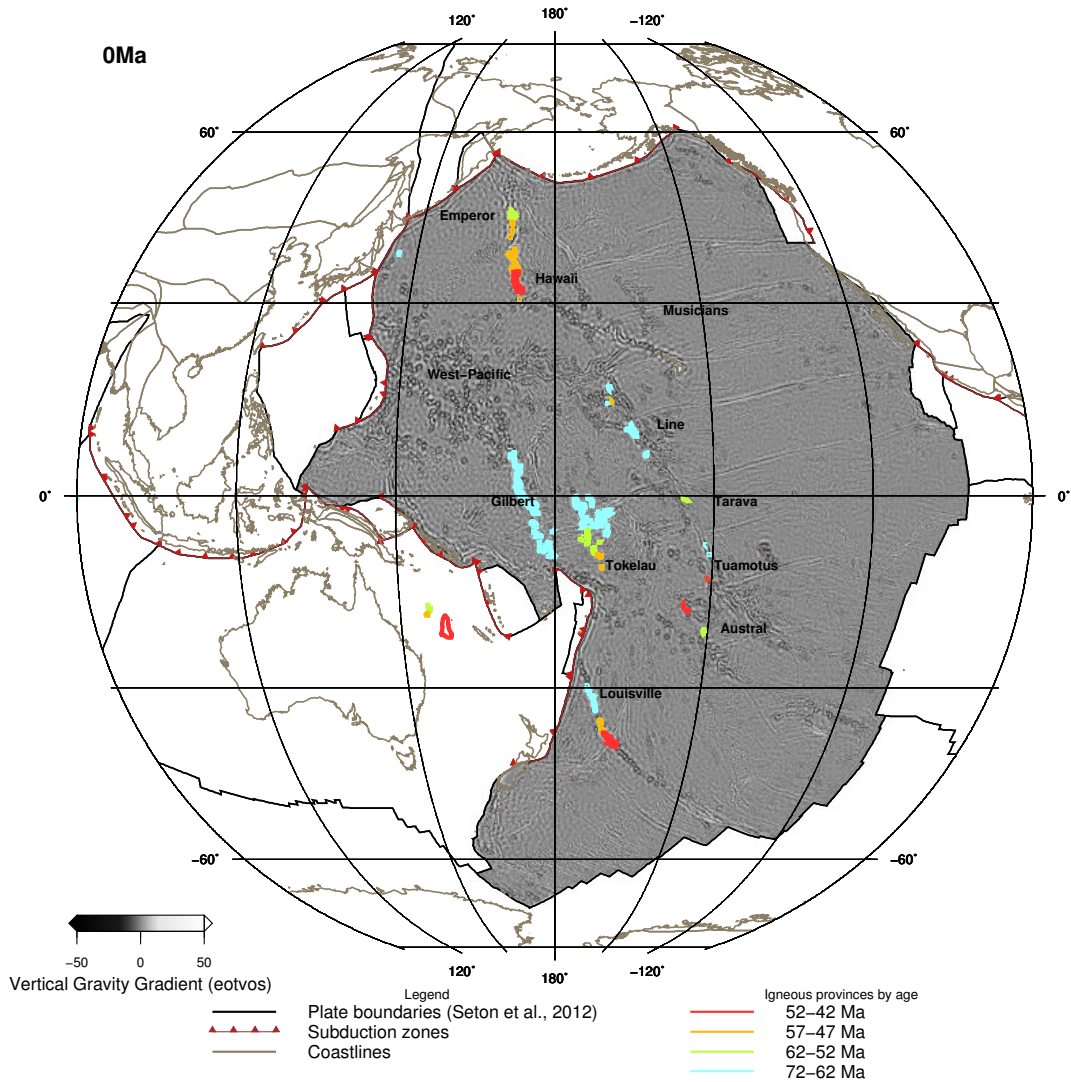
Fig. 7. Present day vertical gravity gradient of the Pacific Plate (Sandwell and Smith, 2009). Present day locations of volcanics dated between 72 and 42 Ma are binned in 10 Myr increments and coloured as in the legend.

on the actual rheological parameters of the Pacific Plate. A subsequent increase in deformation may result in volcanism only if melt material is available, and the lithosphere has pre-existing lines of weakness and/or is weak enough to fracture (Ballmer et al., 2009; Hieronymus and Bercovici, 2000).

5 Conclusions

During the Late Cretaceous and early Cenozoic the Pacific Plate underwent a major tectonic shift in its primary driving forces. In our models prior to 52 Ma, the Pacific was controlled by the Izanagi, Kula, and Farallon subducting plates surrounding it, and to a lesser extent by a small subducting

slab attached at the East Junction subduction zone. From 52 Ma onwards, following the subduction of the Pacific-Izanagi ridge, the Pacific Plate was primarily controlled by slab-pull in the northwest. The absolute motions of the Pacific derived from subduction driven forces correspond well with other modelled plate reconstructions (Seton et al., 2012; Chandler et al., 2012), when model assumptions and simplifications are taken into account. An overestimate of Pacific mantle plume motion constraints used in other absolute reference frames (Doubrovine et al., 2012; Wessel and Kroenke, 2008) is the likely reason for their inconsistencies with Pacific motion in our subduction driven model. The subsequent motion of the plate controls the deformation in the attached subducting plate. We find the regions of highest deformation occur directly adjacent to the most voluminous subducting slabs. Several areas of deformation across the Pacific can be linked to age-dated intraplate volcanism. The seamount chains of Hawaii-Emperor, Louisville, and Tokelau are subject to lithospheric deformation occurring the early Cenozoic. Plate-scale extensional stresses between our modelled time intervals correlate with a large section of the location and timing of formation of the Gilbert chain, suggesting an origin largely due to lithospheric extension at this time. The Musicians Volcanic Ridges, which likely formed by traditional plume mechanisms, spatially correlate with modelled lithospheric stress and is a likely candidate for late-stage volcanism between 52 and 42 Ma. Our simplified 3-D subduction simulations suggest stress-induced deformation in the Pacific during the Late Cretaceous and early Cenozoic is partially controlled by plate-scale kinematics. Our dynamic models, combined with kinematically reconstructed absolute plates motions, confirm the view that the Hawaiian-Emperor bend does not reflect a change in absolute plate motion, but that it reflects the slowdown of the Hawaiian plume drift.

Appendix A

Comparison of initial model condition with Slab1.0

We use 10 Myr of subduction history to build the slabs attached to the geodynamic model subducting plates. The kinematics of the plate model (Seton et al., 2012) determines the total volume of material, dip, and depth of the slab. We find these dips to be comparable to the available Slab1.0 (Hayes et al., 2012) present day slabs (Figs. 8–13).

Appendix B

Volume of subducted material

Plate convergent velocities are determined for each point along the reconstructed subduction zone for each time period. Oceanic lithosphere thickness is derived from the paleo-reconstruction model (Seton et al., 2012) along with sampling age grids with a $1° \times 1°$ resolution (Müller et al., 2013). Using a Half-Space Cooling model truncated at 95 km (after Chapter 4.2 Schubert et al., 2001) the thickness of the lithosphere, z, is determined as

$$z = \text{erf}^{-1}\left(\frac{T_\text{l} - T_\text{o}}{T_\text{m} - T_\text{o}}\right) 2\sqrt{\kappa}\sqrt{\text{age}}, \tag{B1}$$

where, erf^{-1} is the inverse of the error function, $T_\text{l} = 1300\,°\text{C}$ and is the isotherm of the lithosphere, $T_\text{o} = 0\,°\text{C}$ +and is the surface temperature, $T_\text{m} = 1600\,°\text{C}$ and is the temperature of the mantle, $\kappa = 8 \times 10^{-8}\,\text{m}\,\text{s}^{-1}$ and is the thermal diffusivity constant, and age is the age of the lithosphere sampled from the age grids. We calculate the volume of the slab as the convergence rate times the lithospheric thickness times each subduction segment length (from the resolution of the plate model). Figures 14–17 show the amount of globally subducted material for each of the model time periods.
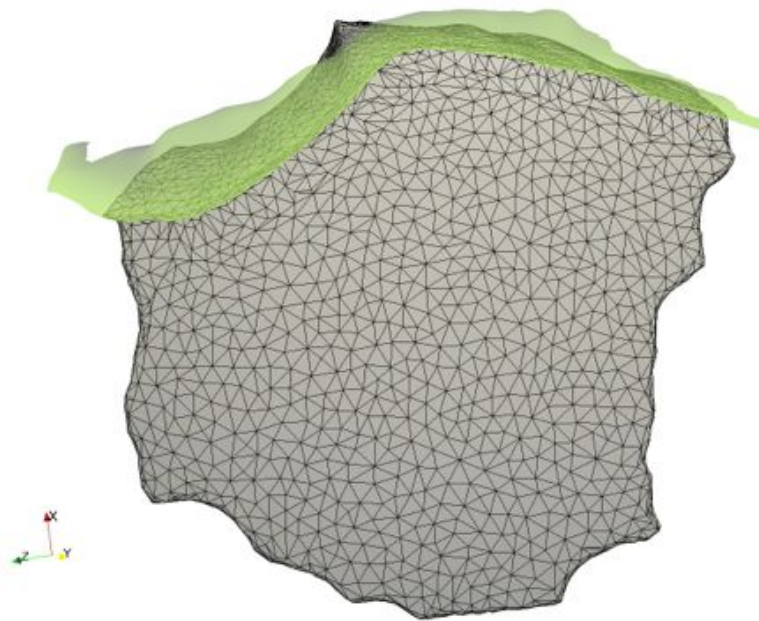
Fig. A 8. Top-down view of the Nazca Plate at present day for geodynamic model input. The green to purple colored topology represents the depth of the Nazca slab from the Slab1.0 (Hayes et al., 2012) interpretation. The black mesh over the plate indicates the resolution of the model. The Slab1.0 interpretation is made slightly transparent to see the extent of modelled plate.
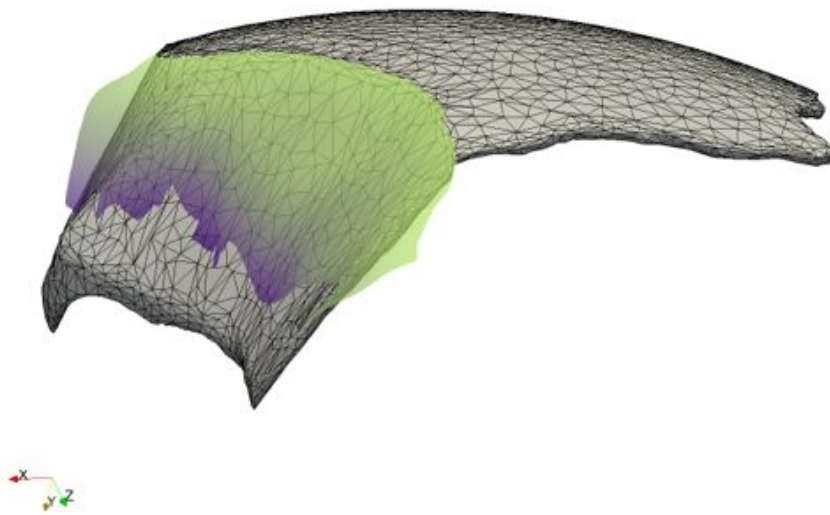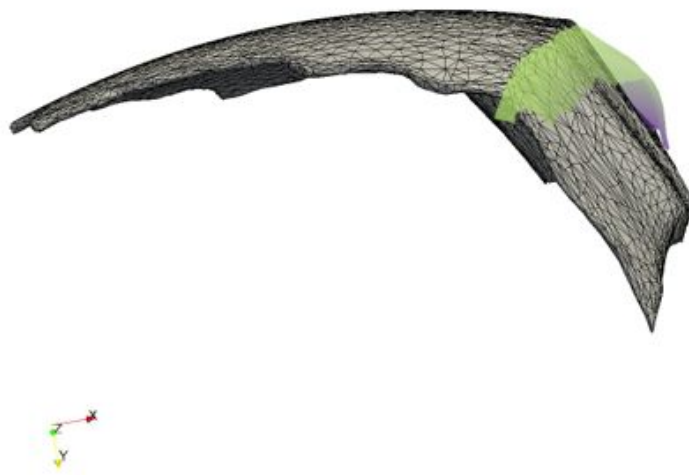
Fig. A 9. North side view of the Nazca Plate at present day for geodynamic model input. The green to purple colored topology represents the depth of the Nazca slab from the Slab1.0 (Hayes et al., 2012) interpretation. The black mesh over the plate indicates the resolution of the model. The Slab1.0 interpretation is made slightly transparent to see the extent of modelled plate.

Fig. A 10. South side view of the Nazca Plate at present day for geodynamic model input. The green to purple colored topology represents the depth of the Nazca slab from the Slab1.0 (Hayes et al., 2012) interpretation. The black mesh over the plate indicates the resolution of the model. The Slab1.0 interpretation is made slightly transparent to see the extent of modelled plate.
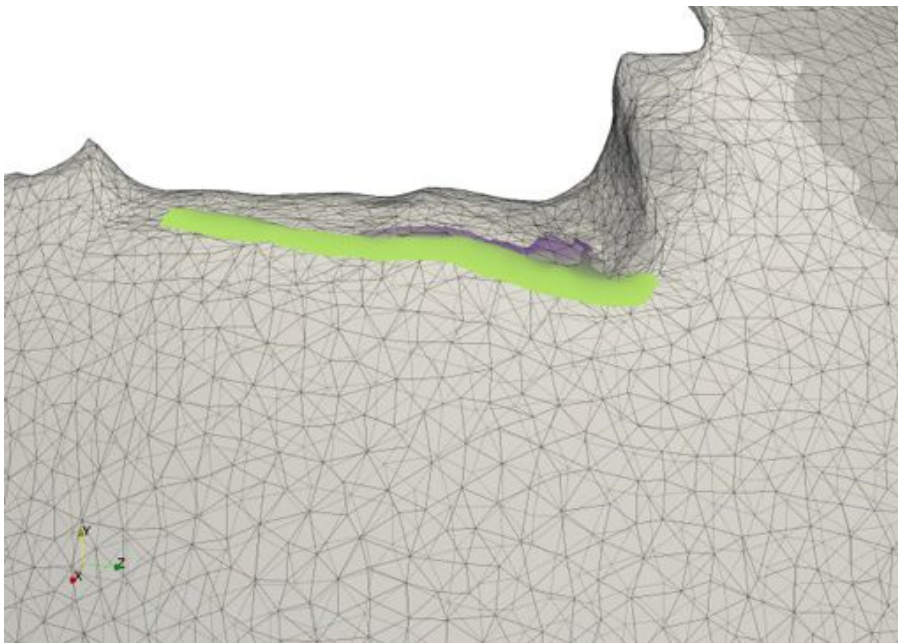
Fig. A 11. Top-down view of the Pacific Plate at present day for geodynamic model input, localized over the Tonga-Kermadec subduction zone. The green to purple colored topology represents the depth of the Kermadec slab from the Slab1.0 (Hayes et al., 2012) interpretation. The black mesh over the plate indicates the resolution of the model. The modelled plate is made slightly transparent to see the extent of the Slab1.0 interpretation.
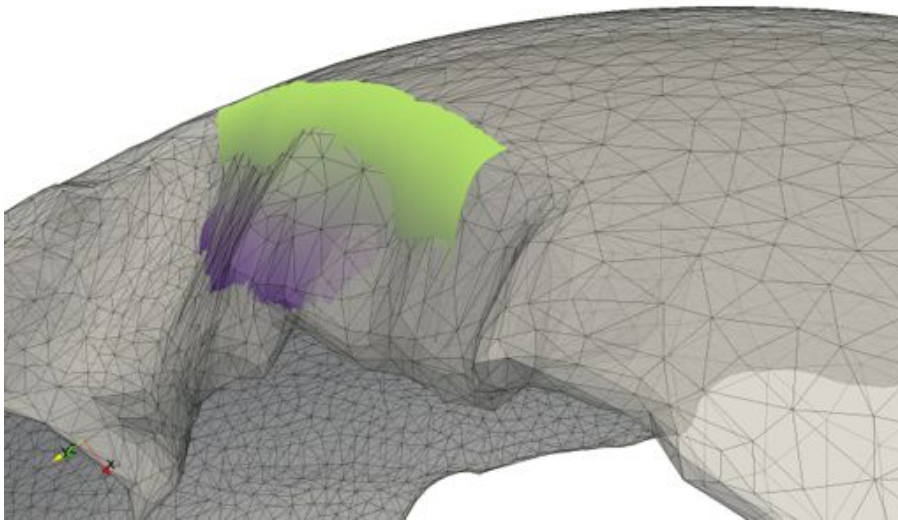
Fig. A 12. Side view of the Pacific Plate at present day for geodynamic model input, looking from the south at the Tonga-Kermadec subduction zone. The green to purple colored topology represents the depth of the Kermadec slab from the Slab1.0 (Hayes et al., 2012) interpretation. The black mesh over the plate indicates the resolution of the model. The modelled plate is made slightly transparent to see the extent of the Slab1.0 interpretation.
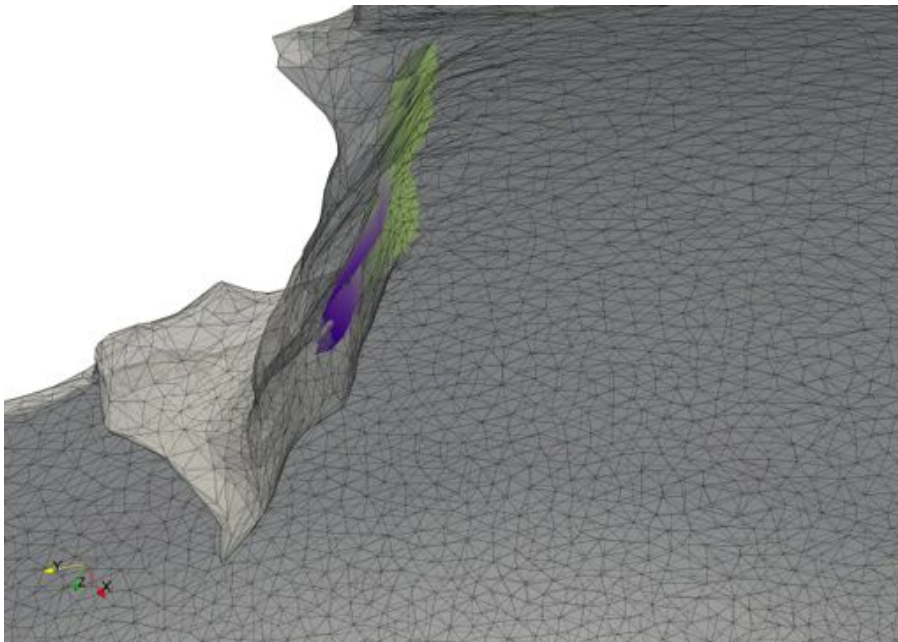
Fig. A 13. View of the Pacific Plate at present day for geodynamic model input, looking from beneath the plate at the Tonga-Kermadec subduction zone. The green to purple colored topology represents the depth of the Kermadec slab from the Slab1.0 (Hayes et al., 2012) interpretation. The black mesh over the plate indicates the resolution of the model.
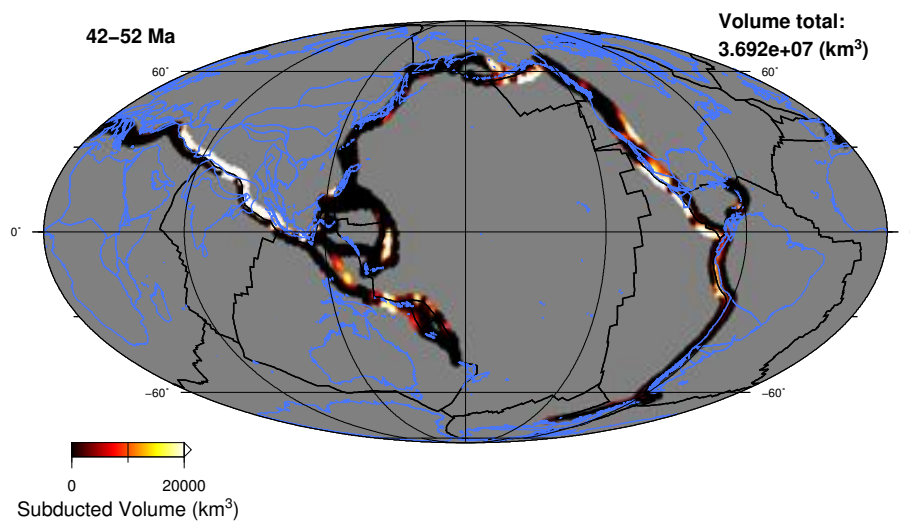

Fig. B 14. Integrated volume of subducted material between 52 and 42 Ma. The color scale represents the volume of material. The total amount of material for this time period is $3.7 \times 10^7 \, \mathrm{km}^3$.

Fig. B 15. Integrated volume of subducted material between 57 and 47 Ma. The color scale represents the volume of material. The total amount of material for this time period is $3.9 \times 10^7 \, \text{km}^3$.

Fig. B 16. Integrated volume of subducted material between 62 and 52 Ma. The color scale represents the volume of material. The total amount of material for this time period is $3.9 \times 10^7 \, \text{km}^3$.
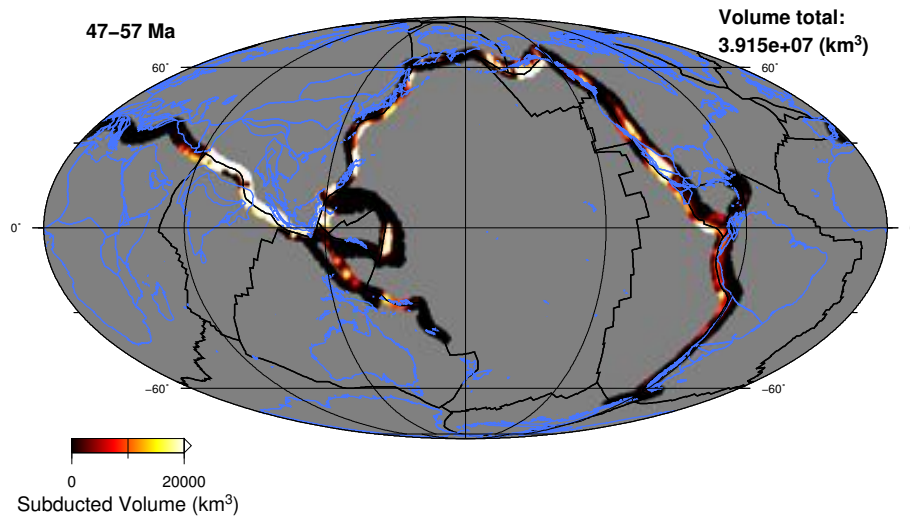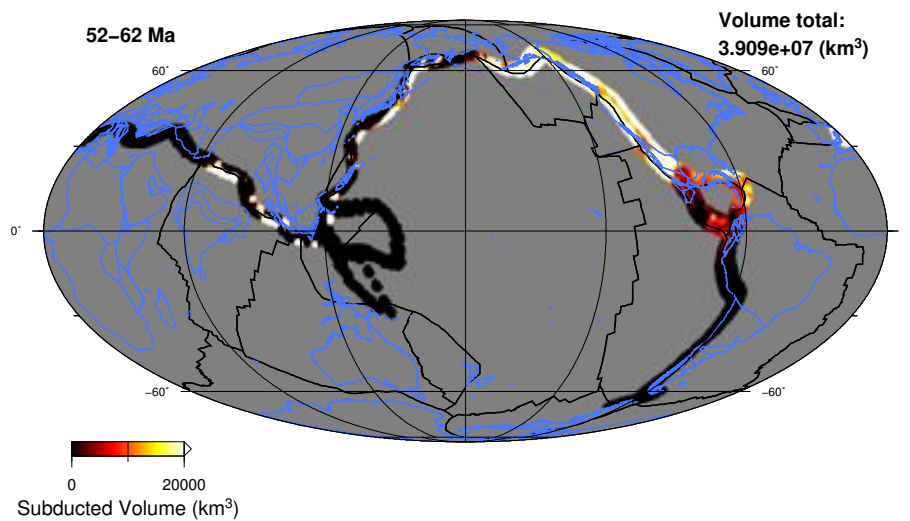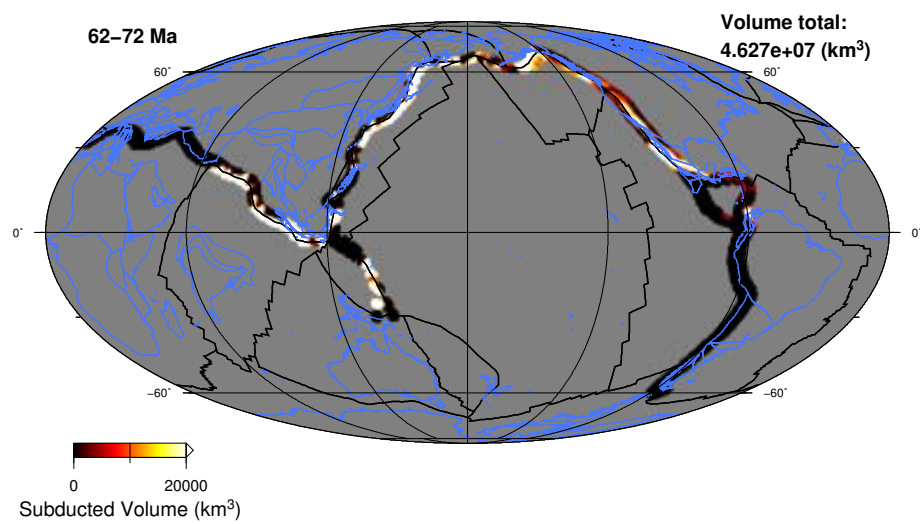
Fig. B 17. Integrated volume of subducted material between 72 and 62 Ma. The color scale represents the volume of material. The total amount of material for this time period is $4.6 \times 10^7 \ \mathrm{km}^3$.

References

Anderson, D.:   Superplumes or supercontinents?,   Geology,   22,   39–42,   doi:10.1130/0091-7613(1994)022<0039:SOS>2.3.CO;2, 1994.

Ballmer, M., van Hunen, J., Ito, G., Bianco, T., and Tackley, P.: Intraplate volcanism with complex age-distance patterns: a case for small-scale sublithospheric convection, Geochem. Geophy. Geosy., 10, Q06015, doi:10.1029/2009GC002386, 2009.

Ballmer, M. D., Conrad, C. P., Smith, E. I., and Harmon, N.: Non-hotspot volcano chains produced by migration of shear-driven upwelling toward the East Pacific Rise, Geology, 41, 479–482, doi:10.1130/G33804.1, 2013.

Billen, M.:   Modeling the dynamics of subducting slabs, Annu. Rev. Earth Pl. Sc., 36, 325–56, doi:10.1146/annurev.earth.36.031207.124129, 2008.

Bonatti, E.:   Not so hot "hot spots" in the oceanic mantle, Science, 250, 107–111, doi:10.1126/science.250.4977.107, 1990.

Boresi, A. P. and Schmidt, R. J.: Advanced Mechanics of Materials, John Wiley and Sons, 2003.

Boyden, J., Müller, R., Gurnis, M., Torsvik, T., Clark, J., Turner, M., Ivey-Law, H., Watson, R., and Cannon, J.: Next-generation plate-tectonic reconstructions using GPlates, in: Geoinformatics: Cyberinfrastructure for the Solid Earth Sciences, edited by: Keller, G. R. and Baru, C., Chap. 7, Cambridge University Press, 95–116, doi:10.1017/CBO9780511976308.008, 2011.

Butterworth, N., Quevedo, L., Morra, G., and Müller, R.: Influence of overriding plate geometry and rheology on subduction, Geochem. Geophy. Geosy., 13, Q06W15, doi:10.1029/2011GC003968, 2012.

Cande, S. C. and Stegman, D. R.: Indian and African plate motions driven by the push force of the Réunion plume head, Nature, 475, 47–52, doi:10.1038/nature10174, 2011.

Capitanio, F., Stegman, D., Moresi, L., and Sharples, W.:   Upper plate controls on deep subduction, trench migrations and deformations at convergent margins, Tectonophysics, 483, 80–92, doi:10.1016/j.tecto.2009.08.020, 2010.

Chandler, M. T., Wessel, P., Taylor, B., Seton, M., Kim, S.-S., and Hyeong, K.: Reconstructing Ontong Java Nui: implications for Pacific absolute plate motion, hotspot drift and true polar wander, Earth Planet. Sc. Lett., 331–332, 140–151, doi:10.1016/j.epsl.2012.03.017, 2012.

Clouard, V. and Bonneville, A.: Ages of seamounts, islands, and plateaus on the Pacific plate, Geol. Soc. Am. S., 388, 71–90, doi:10.1130/0-8137-2388-4.71, 2005.

Clouard, V. and Gerbault, M.: Break-up spots: Could the Pacific open as a consequence of plate kinematics?, Earth Planet. Sc. Lett., 265, 195–208, doi:10.1016/j.epsl.2007.10.013, 2008a.

Clouard, V. and Gerbault, M.: Reply to "Break-up spots: Could the Pacific open as a consequence of plate kinematics?" Comment by R. Pilger, Earth Planet. Sc. Lett., 275, 196–199, doi:10.1016/j.epsl.2008.08.008, 2008b.

Clouard, V., Bonneville, A., and Gillot, P.-Y.: The Tarava Seamounts: a newly characterized hotspot chain on the South Pacific Superswell, Earth Planet. Sc. Lett., 207, 117–130, doi:10.1016/S0012-821X(02)01143-3, 2003.

Conrad, C. and Lithgow-Bertelloni, C.:   How mantle slabs drive plate tectonics, Science, 298, 207, doi:10.1126/science.1074161, 2002.

Conrad, C. and Lithgow-Bertelloni, C.: The temporal evolution of plate driving forces: importance of "slab

suction" versus "slab pull" during the Cenozoic, J. Geophys. Res., 109, B10407, doi:10.1029/2004JB002991, 2004.

Conrad, C. P., Bianco, T. A., Smith, E. I., and Wessel, P.: Patterns of intraplate volcanism controlled by asthenospheric shear, Nat. Geosci., 4, 317–321, doi:10.1038/ngeo1111, 2011.

Courtillot, V., Davaille, A., Besse, J., and Stock, J.: Three distinct types of hotspots in the Earth's mantle, Earth Planet. Sc. Lett., 205, 295–308, doi:10.1016/S0012-821X(02)01048-8, 2003.

Davis, A. S., Gray, L. B., Clague, D. A., and Hein, J. R.: The Line Islands revisited: new ^{40}Ar/^{39}Ar geochronologic evidence for episodes of volcanism due to lithospheric extension, Geochem. Geophy. Geosy., 3, 1018, doi:10.1029/2001GC000190, 2002.

Doubrovine, P., Steinberger, B., and Torsvik, T.: Absolute plate motions in a reference frame defined by moving hot spots in the Pacific, Atlantic, and Indian oceans, J. Geophys. Res., 117, B09101, doi:10.1029/2011JB009072, 2012.

Duncan, R. A. and Keller, R. A.: Radiometric ages for basement rocks from the Emperor Seamounts, ODP Leg 197, Geochem. Geophy. Geosy., 5, Q08L03, doi:10.1029/2004GC000704, 2004.

Faccenna, C., Becker, T. W., Lallemand, S., and Steinberger, B.: On the role of slab pull in the Cenozoic motion of the Pacific plate, Geophys. Res. Lett., 39, L03305, doi:10.1029/2011GL050155, 2012.

Gueydan, F., Morency, C., and Brun, J.-P.: Continental rifting as a function of lithosphere mantle strength, Tectonophysics, 460, 83–93, doi:10.1016/j.tecto.2008.08.012, 2008.

Hayes, G. P., Wald, D. J., and Johnson, R. L.: Slab1.0: a three-dimensional model of global subduction zone geometries, J. Geophys. Res.-Sol. Ea., 117, B01302, doi:10.1029/2011JB008524, 2012.

Hieronymus, C. and Bercovici, D.: Non-hotspot formation of volcanic chains: control of tectonic and flexural stresses on magma transport, Earth Planet. Sc. Lett., 181, 539–554, doi:10.1016/S0012-821X(00)00227-2, 2000.

Hillier, J.: Pacific seamount volcanism in space and time, Geophys. J. Int., 168, 877–889, doi:10.1111/j.1365-246X.2006.03250.x, 2007.

Hirano, N., Takahashi, E., Yamamoto, J., Abe, N., Ingle, S. P., Kaneoka, I., Hirata, T., Kimura, J.-I., Ishii, T., Ogawa, Y., Machida, S., and Suyehiro, K.: Volcanism in response to plate flexure, Science, 213, 1426–1428, doi:10.1126/science.1128235, 2006.

Ito, G. and van Keken, P. E.: Hotspots and melting anomalies, in: Treatise on Geophysics, edited by: Bercovici, D., vol. 7, Mantle Dynamics, Elsevier, 371–435, 2007.

Konter, J. G., Hanan, B. B., Blichert-Toft, J., Koppers, A. A. P., Plank, T., and Staudigel, H.: One hundred million years of mantle geochemical history suggest the retiring of mantle plumes is premature, Earth Planet. Sc. Lett., 275, 285–295, doi:10.1016/j.epsl.2008.08.023, 2008.

Kopp, H., Kopp, C., Morgan, J. P., Flueh, E. R., Weinrebe, W., and Morgan, W.: Fossil hot spot-ridge interaction in the Musicians Seamount Province: geophysical investigations of hot spot volcanism at volcanic elongated ridges, J. Geophys. Res., 108, 2160, doi:10.1029/2002JB002015, 2003.

Koppers, A. A. P.: Mantle plumes persevere, Nat. Geosci., 4, 816–817, doi:10.1038/ngeo1334, 2011.

Koppers, A. A. P. and Staudigel, H.: Asynchronous bends in Pacific seamount trails: a case for extensional volcanism?, Science, 307, 904–907, doi:10.1126/science.1107260, 2005.

Koppers, A. A. P. and Watts, A. B.: Intraplate seamounts as a window into deep Earth processes, Oceanography,

23, 42–57, doi:10.5670/oceanog.2010.61, 2010.

Koppers, A. A. P., Staudigel, H., Pringle, M., and Wijbrans, J.: Short-lived and discontinuous intraplate volcanism in the South Pacific: hot spots or extensional volcanism?, Geochem. Geophy. Geosy., 4, 1089, doi:10.1029/2003GC000533, 2003.

Koppers, A. A. P., Duncan, R., and Steinberger, B.: Implications of a nonlinear ^{40}Ar/^{39}Ar age progression along the Louisville seamount trail for models of fixed and moving hot spots, Geochem. Geophy. Geosy., 5, Q06L02, doi:10.1029/2003GC000671, 2004.

Koppers, A. A. P., Staudigel, H., Morgan, J. P., and Duncan, R.: Nonlinear ^{40}Ar/^{39}Ar age systematics along the Gilbert Ridge and Tokelau Seamount Trail and the timing of the Hawaii-Emperor Bend, Geochem. Geophy. Geosy., 8, Q06L13, doi:10.1029/2006GC001489, 2007.

Koppers, A. A. P., Yamazaki, T., and Geldmacher, J.: Louisville Seamount Trail: implications for geodynamic mantle flow models and the geochemical evolution of primary hotspots, IODP Scientific Prospectus, 330, doi:10.2204/iodp.sp.330.2010, 2010.

Koppers, A. A. P., Gowen, M. D., Colwell, L. E., Gee, J. S., Lonsdale, P. F., Mahoney, J. J., and Duncan, R.: New ^{40}Ar/^{39}Ar age progression for the Louisville hot spot trail and implications for inter–hot spot motion, Geochem. Geophy. Geosy., 12, Q0AM02, doi:10.1029/2011GC003804, 2011.

Lee, C.-T. A. and Grand, S. P.: Intraplate volcanism, Nature, 482, 314–315, doi:10.1038/482314a, 2012.

Li, Z.-H. and Ribe, N. M.: Dynamics of free subduction from 3-D boundary element modeling, J. Geophys. Res., 117, B06408, doi:10.1029/2012JB009165, 2012.

Lithgow-Bertelloni, C. and Richards, M.: The dynamics of Cenozoic and Mesozoic plate motions, Rev. Geophys., 36, 27–78, doi:10.1029/97RG02282, 1998.

Liu, L. and Stegman, D. R.: Origin of Columbia River flood basalt controlled by propagating rupture of the Farallon slab, Nature, 482, 386–390, doi:10.1038/nature10749, 2012.

Matthews, K., Müller, R., Wessel, P., and Whittaker, J.: The tectonic fabric of the ocean basins, J. Geophys. Res., 116, B12109, doi:10.1029/2011JB008413, 2011.

Morgan, W.: Convection plumes in the lower mantle, Nature, 230, doi:10.1038/230042a0, 1971.

Morra, G., Chatelain, P., Tackley, P., and Koumoutsakos, P.: Large scale three-dimensional boundary element simulation of subduction, in: Computational Science – ICCS 2007, edited by: Shi, Y., Albada, G., Dongarra, J., and Sloot, P., Lecture Notes in Computer Science, Vol. 4489, 1122–1129, Springer, Berlin, Heidelberg, 1122–1129, doi:10.1007/978-3-540-72588-6_178, 2007.

Morra, G., Quevedo, L., and Muller, R. D.: Spherical dynamic models of top-down tectonics, Geochem. Geophy. Geosy. 13, 1–66, doi:10.1029/2011GC003843, 2012.

Morra, G., Seton, M., Quevedo, L., and Müller, R. D.: Organization of the tectonic plates in the last 200 Myr, Earth Planet. Sc. Lett., 373, 93–101, doi:10.1016/j.epsl.2013.04.020, 2013.

Müller, R., Dutkiewicz, A., Seton, M., and Gaina, C.: Seawater chemistry driven by supercontinent assembly, breakup, and dispersal, Geology, 41, 907–910, doi:10.1130/G34405.1, 2013.

O'Neill, C., Müller, D., and Steinberger, B.: On the uncertainties in hot spot reconstructions and the significance of moving hot spot reference frames, Geochem. Geophy. Geosy., 6, Q04003, doi:10.1029/2004GC000784, 2005.

Ozima, M., Kaneoka, I., Saito, K., Honda, M., Yanagisawa, M., and Takigami, Y.: Summary of geochrono-

logical studies of submarine rocks from the western Pacific Ocean, in: Geodynamics of the Western Pacific-Indonesian Region, edited by: Hilde, T. W. C., and Uyeda, S., AGU, vol. 11, 137–142 doi:10.1029/GD011p0137, 1983.

Pilger, R.: Discussion of "Break-up spots: could the Pacific open as a consequence of plate kinematics?" by Clouard and Gerbault, Earth Planet. Sc. Lett., 275, 193–195, doi:10.1016/j.epsl.2008.08.005, 2008.

Pringle, M. S.: Age progressive volcanism in the Musicians seamounts: a test of the hot spot hypothesis for the late Cretaceous Pacific, in: The Mesozoic Pacific: Geology, Tectonics, and Volcanism: A Volume in Memory of Sy Schlanger, Geophys. Monogr. Ser, AGU, Washington, D.C., vol. 77, 187–216, doi:10.1029/GM077p0187, 1993.

Quevedo, L., Hansra, B., Morra, G., Butterworth, N., and Müller, R. D.: Oblique mid ocean ridge subduction modelling with the parallel fast multipole boundary element method, Comput. Mech., 51, 455–463, doi:10.1007/s00466-012-0751-5, 2012a.

Quevedo, L., Morra, G., and Müller, R. D.: Global paleo-lithospheric models for geodynamical analysis of plate reconstructions, Phys. Earth Planet. In., 212–213, 106–113, doi:10.1016/j.pepi.2012.09.007, 2012b.

Ribe, N. M.: Bending mechanics and mode selection in free subduction: a thin-sheet analysis, Geophys. J. Int., 180, 559–576, doi:10.1111/j.1365-246X.2009.04460.x, 2010.

Ricard, Y., Richards, M., Lithgow-Bertelloni, C., and Le Stunff, Y.: A geodynamic model of mantle density heterogeneity, J. Geophys. Res.-Sol. Ea., 98, 21895–21909, doi:10.1029/93JB02216, 1993.

Romanowicz, B. and Gung, Y.: Superplumes from the core-mantle boundary to the lithosphere: implications for heat flux, Science, 296, 513–516, doi:10.1126/science.1069404, 2002.

Sandwell, D. and Fialko, Y.: Warping and cracking of the Pacific plate Warping and cracking of the Pacific plate by thermal contraction, J. Geophys. Res., 109, B10411, doi:10.1029/2004JB003091, 2004.

Sandwell, D. and Smith, W. H. F.: Global marine gravity from retracked Geosat and ERS-1 altimetry: ridge segmentation versus spreading rate, J. Geophys. Res., 114, B01411, doi:10.1029/2008JB006008, 2009.

Sandwell, D., Winterer, E., Mammerickx, J., Duncan, R., Lynch, M., Levitt, D., and Johnson, C.: Evidence for diffuse exension of the Pacific plate from Pukapuka ridges and cross-grain gravity lineations, J. Geophys. Res., 100, 15087–15099, doi:10.1029/95JB00156, 1995.

Schellart, W.: Quantifying the net slab pull force as a driving mechanism for plate tectonics, Geophys. Res. Lett., 31, L07611, doi:10.1029/2004GL019528, 2004.

Schubert, G., Turcotte, D. L., and Olson, P.: Mantle Convection in the Earth and Planets, Cambridge University Press, 2001.

Seton, M. and Müller, R.: Reconstructing the junction between Panthalassa and Tethys since the Early Cretaceous, Eastern Australian Basins III. Petroleum Exploration Society of Australia. Special Publication, 263–266, 2008.

Seton, M., Müller, R., Zahirovic, S., Gaina, C., Torsvik, T., Shephard, G., Talsma, A., Gurnis, M., Turner, M., Maus, S., and Chandler, M.: Global continental and ocean basin reconstructions since 200 Ma, Earth-Sci. Rev., 113, 212–270, doi:10.1016/j.earscirev.2012.03.002, 2012.

Sharp, W. and Clague, D.: 50-Ma initiation of Hawaiian-Emperor bend records major change in Pacific plate motion, Science, 313, 1281, doi:10.1126/science.1128489, 2006.

Shaw, W. J. and Lin, J.: Models of ocean ridge lithospheric deformation: dependence on crustal thickness,

spreading rate, and segmentation, J. Geophys. Res., 101, 17977–17993, doi:10.1029/96JB00949, 1996.

Staudigel, H., Park, K.-H., Pringle, M., Rubenstone, J., Smith, W., and Zindler, A.: The longevity of the South Pacific isotopic and thermal anomaly, Earth Planet. Sc. Lett., 102, 24–44, doi:10.1016/0012-821X(91)90015-A, 1991.

Stegman, D., Farrington, R., Capitanio, F., and Schellart, W.: A regime diagram for subduction styles from 3-D numerical models of free subduction, Tectonophysics, 483, 29–45, doi:10.1016/j.tecto.2009.08.041, 2010.

Tarduno, J., Bunge, H.-P., Sleep, N., and Hansen, U.: The Bent Hawaiian-Emperor hotspot track: inheriting the mantle wind, Science, 324, 50–53, doi:10.1126/science.1161256, 2009.

Tarduno, J. A.: On the motion of Hawaii and other mantle plumes, Chem. Geol., 241, 234—247, doi:10.1016/j.chemgeo.2007.01.021, the Great Plume Debate: Testing the Plume Theory, 2007.

Wessel, P. and Kroenke, L. W.: Pacific absolute plate motion since 145 Ma: an assessment of the fixed hot spot hypothesis, J. Geophys. Res., 113, B06101, doi:10.1029/2007JB005499, 2008.

Whittaker, J. M., Muller, R. D., Leitchenkov, G., Stagg, H., Sdrolias, M., Gaina, C., and Goncharov, A.: Major Australian-Antarctic plate reorganization at Hawaiian-Emperor Bend Time, Science, 318, 83–86, doi:10.1126/science.1143769, 2007.

Wilson, J.: A possible origin of the Hawaiian Islands, Can. J. Phys., 41, 863–870, doi:10.1139/p63-094, 1963.

4 Article 3

Butterworth, N. P., Talsma, T., Müller, R. D., Seton, M., Bunge, H-P., Schuberth, B., Shephard, G., (2014), **Geologic, tomographic, kinematic and geodynamic constraints on the dynamics of sinking slabs**, *Journal of Geodynamics*, 73, 1–13, doi:10.1016/j.jog.2013.10.006.

Geological, tomographic, kinematic and geodynamic constraints on the dynamics of sinking slabs

N.P. Butterworth [a,*], A.S. Talsma [a], R.D. Müller [a], M. Seton [a], H.-P. Bunge [b], B.S.A. Schuberth [b], G.E. Shephard [a], C. Heine [a]

[a] EarthByte Group, School of Geosciences, The University of Sydney, New South Wales 2006, Australia
[b] Department of Earth and Environmental Science, Ludwig-Maximilians-Universität München, Germany

ARTICLE INFO

ABSTRACT

We use geodynamic models with imposed plate velocities to test the forward-modeled history of subduction based on a particular plate motion model against alternative seismic tomography models. We utilize three alternative published reference frames: a hybrid moving hotspot-palaeomagnetic, a hybrid moving hotspot-true polar wander corrected-palaeomagnetic, and a Subduction Reference Frame, a plate model including longitudinal shifts of subduction zones by matching subduction volumes imaged by P-wave tomography, to assess which model best predicts present day mantle structure compared with seismic tomography and volumetrically derived subduction history. Geodynamic modeling suggests paleo-longitudinal corrections applied to the Subduction Reference Frame result in lower mantle slab material beneath North America and East Asia accumulating up to 10–15° westward of that imaged by tomography, whereas the hybrid models develop material offset by 2–9°. However, the Subduction Reference Frame geodynamic model produces slab material beneath the Tethyan Domain coinciding with slab volumes imaged by tomography, whereas the hybrid reference frame models do not, suggesting regional paleo-longitudinal corrections are required to constrain slab locations. We use our models to test inferred slab sinking rates in the mantle focusing on well-constrained regions. We derive a globally averaged slab-sinking rate of 13 ± 3 mm/yr by combining the ages of onset and cessation of subduction from geological data and kinematic reconstructions with images of subducted slabs in the mantle. Our global average slab-sinking rate overlaps with the 15–20 mm/yr rate implied by mantle convection models using a lower mantle viscosity 100 times higher than the upper mantle.

© 2013 Elsevier Ltd. All rights reserved.

1. Introduction

Plate tectonic absolute reference frames are essential for linking plate motions and the history of subduction to mantle dynamics—yet they are subject to substantial ambiguities, reflecting uncertainties in paleomagnetic and hotspot track data. Additional constraints on absolute plate motion can be derived by considering the inherent connection between plate boundaries and the history of subduction reflected by tomographically interpreted subducted slabs in the mantle. Over the last decade, our knowledge about relative motion between the major tectonic plates has increased substantially, primarily due to advances in seafloor mapping and data coverage. Absolute plate motions, which anchor relative plate motions to a fixed reference frame in the Earth's interior, are still controversial as different approaches advocate alternative absolute plate positions through time. Previous

attempts to construct absolute reference frames have fallen into two primary camps: those based on palaeomagnetic data (e.g. Torsvik et al., 2008b) and those based on hotspots (e.g. O'Neill et al., 2005). Paleomagnetic data can be used to determine the paleo-meridian orientation and paleolatitude of a plate, which together can be used to derive total reconstruction poles. However, since the Earth's magnetic dipole field is radially symmetric, no paleo-longitudinal information can be deduced from paleomagnetic data (Torsvik et al., 2008a). Seamount chains with a linear age progression (i.e. hotspot tracks) can be used to restore plates to their paleo-positions with the assumption that hotspots are either fixed or nearly fixed relative to each other ("fixed hotspot hypothesis") (Morgan, 1983). Continuous hotspot chains that extend beyond 100 Ma are rare, and there is observational and geodynamic modeling evidence suggesting hotspots have moved relative to each other (Steinberger and O'Connell, 1997; Tarduno et al., 2003; O'Neill et al., 2005). Numerous paleomagnetic datasets and models for the "absolute" motions of the North American, African and Eurasian plates during the Mesozoic and Cenozoic have been published and they reveal various inconsistencies between different apparent polar

* Corresponding author. Tel.: +61 293518093.
E-mail address: nathaniel.butterworth@sydney.edu.au (N.P. Butterworth).

wander (APW) paths, some corrected for true polar wander, and hotspot models, especially for times older than about 100–80 Ma (Steinberger and Torsvik, 2008; Torsvik et al., 2008b).

Discriminating between alternative approaches is difficult without a series of tie-points between the surface and the underlying mantle. The idea that the inferred location of subduction zones through time could be reconciled with tomographically imaged locations of subducted slab material in the Earth's lower mantle ("slab graveyards" Richards and Engebretson, 1992) led to a new generation of absolute plate motion model called Subduction Reference Frames (Van der Meer et al., 2010). Seismic tomography models allow visualization of subducted slabs, and can be used to validate geodynamic models of mantle convection. In order to utilize the history of subduction in the mantle as a constraint on absolute plate motions it is required to understand the regionally dependent sinking histories of so-called 'anchor' slabs. Information from the geological record that indicates beginning and cessation of subduction, as well as from geodynamic modeling, can be used together to unravel the history and dynamics of sinking lithospheric slabs and to construct and test the accuracy of Subduction Reference Frames (Sigloch and Mihalynuk, 2013).

We test three published hybrid models of absolute plate motion while keeping the relative plate motion model and geodynamic model parameters constant. This is done by imposing alternative absolute reference frame models as surface boundary conditions for a series of finite element forward geodynamic models. The models of plate motion tested included a hybrid moving hotspot-paleomagnetic reference frame (O'Neill et al., 2005; Torsvik et al., 2008a), a hybrid moving hotspot-paleomagnetic reference frame corrected for true polar wander (TPW) (O'Neill et al., 2005; Steinberger and Torsvik, 2008), and a Subduction Reference Frame (Van der Meer et al., 2010). Key subduction zones are examined to quantify regional latitudinal/longitudinal differences between absolute rotation models. Geodynamic model output is compared to four recent seismic tomography models for validation of stable features. Identification of tomographically imaged "reference" slabs, which are visible in many tomographic models regardless of inversion technique, as well as the slabs' relationship to surface kinematics is tantamount to further developing robust surface-deep mantle reference points. We examine age-depth relationships of subducted material and slab sinking rates within the mantle in order to use the record of subduction provided by seismic tomography as a constraint for absolute plate motion.

2. Methods

2.1. Plate kinematic models

To assess the implications of alternative reference frames, we use a coupled plate kinematic-mantle convection modeling approach, whereby the predicted present-day mantle structure is compared to seismic tomography models. We use a plate motion model as input into the geodynamic mantle convection code.

A plate motion model comprises relative motions between plates linked via a plate circuit to an absolute reference frame. The hierarchical nature of our plate model links the global plate circuit through Africa to the absolute reference frame. For the purposes of constructing the three alternate absolute reference frames, the relative plate rotation model from Müller et al. (2008) is used. This rotation hierarchy contains Euler poles describing motions of all major tectonic elements. One complication in using absolute plate motion models before 83.5 Ma is that the Pacific plate cannot be linked to the plate circuit via relative plate motions before this time, as the Pacific Ocean was entirely surrounded by subduction zones. Therefore the Pacific plate is reconstructed between 83.5 and 140 Ma based on the absolute plate rotation model by Wessel et al. (2006), which is based on fixed Pacific hotspots, and moves independently to the hotspots in the Indian-Atlantic realm. A recent paper by Doubrovine et al. (2012) attempted to create a global reference model to overcome this limitation and this will be tested as part of a further study.

We use realistic, evolving plate boundaries and motions, termed "dynamically closing" or "continuously closing" plate polygons through time (Gurnis et al., 2012) and utilize a set of plate topologies, which consist of paleo and current mid ocean ridges, subduction zones and transform plate boundaries, constructed using the GPlates software package (www.gplates.org). The same set of topological plate boundaries is used for all three alternate models, and as such, only the relative position of the plates differs between models (Fig. 1).

2.1.1. Hybrid moving hotspot and paleomagnetic reference frame model

This model utilizes the moving Indo-Atlantic hotspots of O'Neill et al. (2005) to constrain absolute plate motion between 100–0 Ma, while paleomagnetic constraints of Torsvik et al. (2008a) were used between 140 and 100 Ma. For the purpose of this model, Africa
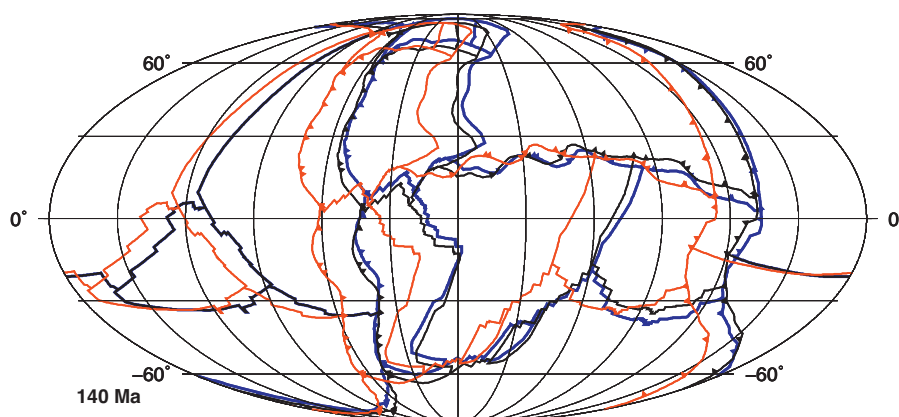

Fig. 1. Longitudinal differences between the three alternate models of absolute plate motion at 140 Ma, showing the initial plate configuration for each Terra model input, with red lines corresponding to reconstructed plate boundaries using the subduction Reference Frame, black lines are the Hybrid TPW Paleomagnetic reference frame, and blue lines are the Hybrid Paleomagnetic reference frame. TPW is only applied to the African hemisphere as there is no link to the Pacific prior to 83.5 Ma, hence the two paleomagnetic reference frames are identical inside the Pacific basin. Triangles on the lines represent subduction zones. (For interpretation of the references to color in this figure legend, the reader is referred to the web version of the article.)

is held as longitudinally fixed between 140 and 100 Ma, which is based on the assumption that Africa has been surrounded by mid ocean ridges during this time. Geodynamic output based on this reference frame will referred to as the Hybrid Paleomagnetic model.

2.1.2. Hybrid moving hotspot and TPW corrected paleomagnetic reference frame model

The moving Indo-Atlantic hotspot model of O'Neill et al. (2005) was used in order to constrain the absolute rotations of Africa from the period of 100–0 Ma. For times between 140 and 100 Ma, a true polar wander corrected paleomangetic reference frame was used derived from Steinberger and Torsvik (2008). As the motion of the poles is known to be quite stable for the past 100 Myr, due to a general decrease in the amount of subduction at polar latitudes and increase at equatorial latitudes (Steinberger and Torsvik, 2010), corrections are not applied from 100 Ma to the present. Even so, use of the hotspot reference frame after 100 Ma negates the requirement for true polar wander correction in this time period. The geodynamic model resulting from this reference frame will henceforth be called the Hybrid TPW Paleomagnetic model.

2.1.3. Subduction Reference Frame model

The rotations of Van der Meer et al. (2010) were used in order to construct a Subduction Reference Frame model. The Subduction Reference Frame is based on the same TPW corrected paleomagnetic absolute reference frame used in this study (O'Neill et al., 2005; Steinberger and Torsvik, 2008) but with additional absolute longitudinal corrections to the absolute position of Africa between 140 Ma and present day. The model utilizes tomographic model UU-P07 (Amaru, 2007), a global P-wave tomography model, to isolate positive velocity anomalies in the lower mantle interpreted as subducted slabs. It longitudinally corrects Africa's absolute rotations by correlating deep mantle tomographic anomalies with surficial geological evidence of past subduction events, assuming that material sinks vertically in both the upper and lower mantle. It uses three primary anchor slabs in order to correct for this longitudinal mismatch: the Aegean Tethys, the Mongol-Okhotsk and the Farallon slab, to correct rotations from the Permo-Triassic to the present day. Their analysis found longitudes to be most offset from the TPW paleomagnetic reference frame during the mid Mesozoic, requiring corrections of up 18° during this time. We note that the applied longitudinal shift removes the fit to the hotspot record. The geodynamic model resulting from this reference frame will be referred to as the Subduction Reference Frame model.

2.2. Global mantle convection models

In order to simulate mantle convection through time, we use the parallel 3D finite element code, Terra (Bunge and Baumgardner, 1995; Bunge et al., 1996, 1997; Oeser et al., 2006). Terra solves the equations that govern the conservation of mass, momentum and energy for a highly viscous fluid (appropriate for the mantle) at infinite Prandtl number in a 3D spherical shell in a compressible form. The modeling domain is discretized with a mesh derived from the icosahedron to assure an almost uniform grid spacing at each radial level with a grid resolution of 30 km at the surface and ~25 km in the radial direction. The high numerical resolution allows us to model mantle flow at Earth-like convective vigor, expressed by a thermal Rayleigh number of ~10$\hat{9}$ based on internal heating. Input parameters, given in Table 1, are equivalent to Schuberth et al. (2009a).

We divide the Earth's mantle into three layers; the lithosphere, and the upper and lower mantle, in order to represent its radially varying material properties. The assigned viscosities are 10^{23}, 10^{21} and 10^{23} Pa s, respectively. The layers are separated at 100 km and 660 km, numbers inferred as first order rheological stratification

Table 1
Variables kept constant between model runs.

Variable	Value	Units
Outer shell radius	6370	km
Inner shell radius	3480	km
Surface temperature	300	K
Basal temperature	4200	K
Internal heating rate	6.0×10^{-12}	W kg^{-1}
Heat capacity	1.134×10^3	J kg^{-1} K^{-1}
Thermal expansivity (surface)	4.011×10^{-5}	K^{-1}
Thermal expansivity (CMB)	1.256×10^{-5}	K^{-1}
Thermal Conductivity	3.0	W m^{-1} K^{-1}
Reference Viscosity	1.0×10^{21}	Pa s
Rayleigh number	$\sim 10^9$	

boundaries in the mantle based on geoid studies and post-glacial rebound (Hager and Richards, 1989; Paulson et al., 2007). We use only radial viscosity layering, with no lateral variation. Including temperature dependant viscosity was beyond the scope of this study, but would serve to localize the coherency of slabs, increasing upper mantle sinking speed by a few 10's of percent. In the lower mantle however, it would have negligible effect on slab sinking rates, but might affect slab morphology leading to less internal deformation and thus more accurate comparisons with tomography.

Temperature is kept constant at the surface (300 K) and the CMB (4200 K), with the CMB temperature chosen to yield global mantle flow with strong plume flux (Bunge, 2005). A dynamic regime dominated by thermal structure provides a good match to seismic tomography in terms of heterogeneity strength (Schuberth et al., 2009a,b) and radial profiles (Styles et al., 2011). Mechanical boundary conditions are free slip at the CMB. At the surface, velocities are imposed using pre-generated plate kinematic models. Velocities are specified at the surface and assimilated using a sequential data assimilation method (Talagrand, 1997). This is done in order to allow material to be input into the mantle at reasonable rates known from present day plate velocities (Schuberth et al., 2009b). Subduction zones therefore evolve at areas of convergence through time, where linear downwellings are pulling on the overriding cold material. Sinking is dynamically computed following from solving the conservation equations. As the structure of the mantle in the geological past is essentially unknown, the choice of initial mantle condition is necessarily arbitrary. Here, the unknown conditions of mantle heterogeneity at the model start time are approximated by running convection with global plate configurations fixed to the 140 Ma reconstruction of each absolute plate motion model until a quasi steady thermal state is reached (Bunge et al., 2002). The relative location for each model's plate boundaries and subduction zones at 140 Ma is shown in Fig. 1.

Endothermic phase transitions at 660 km are not included in this study, as the appropriate parameters (i.e. Clapeyron slopes) to use are not obvious due to the effects of different mineralogies, complex multiphase components and the presence of water. Phase transitions would likely have the net affect of increasing mantle residence time of sinking slabs, including them was beyond the scope of this study.

2.3. Tomography models

Seismic tomography provides a means of imaging the deep earth based on heterogeneities in seismic wave speed received at the Earth's surface. As numerous inversion methods exist for constructing tomographic models we compare our model output to multiple tomography models based on different approaches and data to emphasize common stable features between models and avoid over interpretation of any one model. We utilize two P-wave models,

MIT-P08 (Li et al., 2008) and Montelli-P (Montelli et al., 2004), and two S-wave models, GyPSuM-S (Simmons et al., 2010) and s40rts (Ritsema et al., 2010).

2.3.1. MIT-P08

The MIT-P08 seismic tomography model of Li et al. (2008) utilizes P-wave travel time residuals computed from ak135 (Kennett et al., 1995). As it is based on P-wave data, MIT-P08 displays the best resolution near seismic receiver-rich areas (i.e. well instrumented subduction zones). It is appropriate for imaging upper mantle structures such as subducting lithospheric slabs, but lacks resolution in receiver-poor ocean basins and in the deeper mantle (Li et al., 2008).

2.3.2. Montelli-P

The Montelli-P tomographic model utilizes finite-frequency sensitivity kernels to account for the effects of wavefront healing on low frequency P-waves in order to better resolve small-scale (i.e. slab and plume, sub-Frensel zone, sized) structures in the deep mantle (Montelli et al., 2004). Being a P-wave model, data coverage is best near subduction zones and receiver rich areas; however it includes both long and short period P-wave data sets.

2.3.3. GyPSuM-S

The GyPSum-S model utilizes data from a wide range of geophysical sources. It simultaneously inverts S and P wave seismic data as well as geodynamic constraints (i.e. constraints from free-air gravity, plate motions, dynamic topography and core ellipticity) in order to better account for non-thermal heterogeneity (Simmons et al., 2010).

2.3.4. s40rts

s40rts is an S-wave based tomographic model that focuses on maximizing data coverage in the mantle, especially over receiver poor areas, utilizing 3D perturbations of isotropic shear velocity with respect to the Preliminary Reference Earth Model (Ritsema et al., 2010). s40rts differs from previous approaches in that it uses a data set larger by an order of magnitude compared to s20rts, hence offering higher spatial resolution than previous models. This leads to an improved resolution in areas away from subduction zones (i.e. in the oceans, stable areas distal from active plate margins, receiver poor areas).

3. Results

Our aims are two fold—to examine the implications of different absolute reference frame models in a global geodynamic model, and to use geodynamic model results to constrain the relationship between tomographically imaged slabs and surface plate kinematics. In order to examine how well different absolute reference frames reproduce observations made from alternative tomographic images of the mantle, three modeled scenarios of absolute plate motion and the four alternate tomography models are compared and analyzed. The relationship between kinematics and tomographically identified slabs inherently provides information about slab sinking (Steinberger et al., 2012), thus providing an important constraint for absolute plate motion by demonstrating visible tie points between the subducting lithosphere at Earth's surface and the deep mantle. Furthermore, inferences about slab sinking rates and mantle viscosity can be made, allowing a more accurate comparison between geodynamic models and tomography models.

We follow the approach of Van der Meer et al. (2010) and correlate areas where the onset and cessation of subduction are relatively well constrained by geological data, such as ophiolite obduction and arc magmatism, to seismic anomalies interpreted as

Table 2

Reinterpreted age assignments for the base and top of subducted slabs interpreted in Van der Meer et al. (2010). Depths are those listed in Van der Meer et al. (2010) derived from tomography model UU-P07 (Amaru, 2007).

Model	UU-P07					
	Age (Ma)		Base (km)		Top (km)	
Slab name	Base	Top	Min	Max	Min	Max
Aegean Tethys	170	0	2100	1900	0	0
Aleutian	50	0	810	710	0	0
Beaufort	200	155	2650	2480	2300	2100
Chukchi	160	130	1900	1700	1325	1175
East China	200	158	2900	2815	1900	1700
Farallon	185	60	2650	2480	920	710
Himalayas	80	30	1175	1040	500	440
Kamchatka	60	0	920	810	0	0
Maldives	180	80	2300	2100	920	810
Manchuria	50	0	920	810	0	0
Mesopotamia	165	80	2300	2100	1175	1040
Mongol Okhotsk	–	150	2900	2815	1900	1700
Mongolia	165	80	1900	1700	1175	1040
Sakhalin	65	50	1175	1040	810	710

subducted slabs common in multiple tomography models. Depths are derived from four alternate tomography models, two P-wave models MIT-P08 (Li et al., 2008) and Montelli-P (Simmons et al., 2010) and two S-wave models GyPSum-S (Simmons et al., 2010) and s40rts (Grand, 1994), plus we include the interpretations of Van der Meer et al. (2010) determined with UU-P07 (Amaru, 2007). Derived slab depths can be seen in Tables 2–4. 'Slabs' are picked from where there is a sharp change in the positive seismic anomalies evident in the tomography models (Supplementary Information). We define this as being one standard deviation away from the median seismic velocity anomaly in each tomography model. We determine these contour values to be +0.6% for s40rts, +0.2% for MIT-P08, +0.6% for GyPSum-S, and +0.3% for Montelli-P. Slabs in the Terra models are determined in a similar fashion, resulting in a -200 K temperature anomaly contour. Ages are reinterpreted where the base plate kinematic model (Müller et al., 2008) differed substantially from the interpretation of Van der Meer et al. (2010) (Table 2). While Van der Meer et al. (2010) included a total of 28 slabs, only those which are relatively well constrained in our models are reinterpreted. An effort was made to avoid slabs that lay along the CMB, as lateral spreading here would serve to artificially decrease a whole mantle sinking rate average. Even with the choice of well-constrained slabs and a quantitative approach to define a slab, the depth and location variation between models is apparent. We state the depth uncertainty (Tables 2–4) between an assumed max and minimum value based on each tomography model's published depth slices, however the uncertainty is likely to be poorer than the errors we have stated. This is due to a number of reasons; firstly, determining model resolution is not straightforward (Lévêque et al., 1993). Slab dip and slab thickening will also influence the apparent slab depth (Van der Meer et al., 2010). Finally, matching the correct latitudinal subducted slab point with the surface timing point is impossible without a thorough understanding of the slab's evolution. To minimize these issues, we use a process of determining slab depths in an iterative manner to qualitatively correlate the surface geological constraints and the corresponding point on the subducted slab. This was achieved by analysing the location of geological constraints, plate boundary surface kinematics, subduction volume history, tomographically imaged slab locations, and geodynamic model slab location results (Supplementary Information).

We initially discuss the subduction history of each region and relate it to tomography, and then discuss the geodynamic modeling results.

Table 3
Reinterpreted depths of slabs from S-wave tomography models s40rts and GyPSuM-S. Min and Max values are inferred from an iterative interpretation (Supplementary Information) and are precise to the model's published depth slices.

Model	GyPSuM-S				s40rts			
	Base (km)		Top (km)		Base (km)		Top (km)	
Slab name	Min	Max	Min	Max	Min	Max	Min	Max
Aegean Tethys	2050	1900	0	0	2020	2000	0	0
Aleutian	850	750	0	0	440	420	0	0
Beaufort	2200	2050	1300	1150	2280	2260	1340	1320
Chukchi	2050	1900	1000	850	1680	1660	1260	1240
East China	2900	2650	1900	1750	2800	2800	1640	1620
Farallon	2500	2350	750	650	2200	2180	380	360
Himalayas	1150	1000	750	650	1000	980	480	460
Kamchatka	–	–	–	–	660	640	0	0
Maldives	2350	2200	1150	1000	2080	2060	1000	980
Manchuria	750	650	0	0	780	760	0	0
Mesopotamia	2200	2050	1300	1150	1980	1960	1020	1000
Mongol Okhotsk	2900	2650	2500	2350	2800	2800	2020	2000
Mongolia	1750	1600	1300	1150	2260	2240	1520	1500
Sakhalin	400	325	325	250	1000	980	440	420

Table 4
Reinterpreted depths of slabs from P-wave tomography models MIT-P08 and Montelli-P. Min and Max values are inferred from an iterative interpretation (Supplementary Information) and are precise to the model's published depth slices.

Model	MIT-P08				Montelli-P			
	Base (km)		Top (km)		Base (km)		Top (km)	
Slab name	Min	Max	Min	Max	Min	Max	Min	Max
Aegean Tethys	1649	1604	0	0	2020	2000	0	0
Aleutian	836	791	0	0	780	760	0	0
Beaufort	–	–	–	–	2160	2140	1380	1360
Chukchi	1830	1785	1468	1423	1920	1900	1080	1060
EastChina	2869	2869	1830	1785	2900	2900	1640	1620
Farallon	1830	1785	384	339	1800	1780	520	500
Himalayas	926	881	384	339	1080	1060	500	480
Kamchatka	1017	971	0	0	1500	1480	0	0
Maldives	2191	2146	926	881	2200	2180	840	820
Manchuria	746	700	0	0	880	860	0	0
Mesopotamia	2011	1965	1107	1062	2120	2100	880	860
Mongol Okhotsk	2869	2869	2191	2146	2900	2900	2240	2200
Mongolia	2011	1965	1107	1062	1940	1920	920	900
Sakhalin	1197	1152	474	429	880	860	440	420

3.1. Subduction initiation/cessation age interpretation

In the following regions, we interpret the ages of subduction initiation/cessation, based on a variety of published geological and geophysical observations.

3.1.1. North America

The western North American margin has seen long-lived subduction of the Farallon oceanic plate since at least the mid Mesozoic resulting in a myriad of accreted volcanic arc terranes along the west coast (DeCelles et al., 2009; Nokleberg et al., 2000; Ward, 1995). A number of detailed seismic tomographic studies show the slab material beneath the continent (Grand, 1994; Liu et al., 2008; Sigloch, 2011; Sigloch et al., 2008). The margin has been subject to various periods of subduction and back arc spreading as well as periods of flat slab subduction leading to a complicated geometry of subducted slab material (Sigloch and Mihalynuk, 2013). Subduction has been occurring since the late Triassic/early Jurassic, with the continued accretion of the Talkeentna, Bonanaza and Stikinia-Quesnellia arcs and formation of their associated subduction zones (Nokleberg et al., 2000). We take the approach of placing the base of the Farallon slab at between 195 and 175 Myr old (Nokleberg et al., 2000). This differs slightly from Van der Meer et al. (2010) who place its age between 208 and 180 Ma.

The North American profile (Figs. 2 and 3) highlights west dipping subducted Farallon oceanic lithosphere and was used by Van der Meer et al. (2010) as a key slab in order to constrain absolute plate motion. The Farallon slab (anomaly 1 in Figs. 2 and 4) is visible in all tomography models and reproduced in all three geodynamic model runs. The Hybrid Paleomagnetic and Hybrid TPW Paleomagnetic models reproduce the present day mantle structure observed in seismic tomography models better at the first order than the Subduction Reference Frame model, especially around lower mantle depths ($\sim$2000–2500 km). The Subduction Reference Frame model produces subducted material too far (10–15°) west of that imaged by tomography, especially in the mid to lower mantle. Given model sinking rates ($\sim$15–20 mm/yr), this material represents subduction occurring at around 100–130 Ma, where the corrections applied for longitude were between 14–18°. This suggests that longitudinal corrections to the absolute rotations are most-likely too great for the time period that corresponds to these depths, the surface subduction location from the plate model is offset, or the geodynamic model sinking rate is too high.

3.1.2. East Asia

The East Asian margin represents the location of long-lived subduction from the Mesozoic to the present day. Van der Meer et al. (2010) interpret at least 3 major phases of subduction corresponding to seismically fast anomalies within the mantle, which
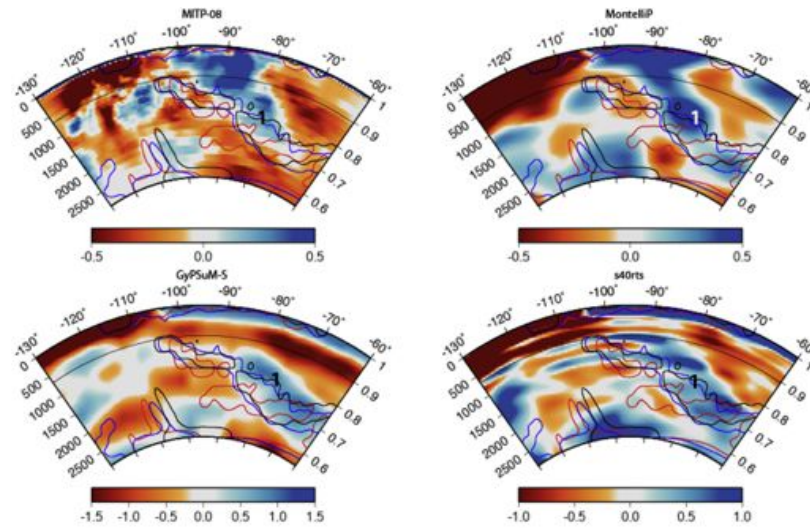
Fig. 2. Vertical cross section at 35° N. Anomaly 1 reflects subducted Farallon oceanic plate. Contours are the −200 K Terra temperature field output; blue contours represent the Hybrid Paleomagnetic model, black contours represent the Hybrid TPW Paleomagnetic model and red contours represent the subduction Reference Frame model. (For interpretation of the references to color in this figure legend, the reader is referred to the web version of the article.)

they term the Manchuria (upper, anomaly 1 in Fig. 4) Mongolian (mid-mantle, anomaly 2 in Fig. 4) and East China (lower mantle, anomaly 3 in Fig. 4) slabs. We interpret gaps in the tomography record as representing back arc spreading and the subduction of the Izanagi-Pacific ridge generating a visible slab window in the seismic tomography. Episodic magmatism within the Korean peninsula provides onshore geological constraints of this subduction, with three primary phases occurring (248–210 Ma, 197–158 Ma and 110–50 Ma) (Sagong et al., 2005). The 197–158 Ma phase and the 110–50 Ma phase are interpreted as being related to the East China and Mongolia slabs respectively, with the ~50 Myr gap from 158 Ma to 110 Ma representing back arc spreading and a shifting of volcanism offshore. Following subduction of the mid-mantle anomaly, interpreted as being Izanagi oceanic material, the Pacific-Izanagi ridge was subducted around 60–55 Ma (Whittaker et al., 2007), which led to a large scale plate reorganization and to a ~10 Myr

gap in the subduction record in the vicinity of subduction. The Manchuria slab is interpreted as Pacific lithosphere that has subducted since the Izanagi ridge subduction (50 Ma–present). The ages of slab material in East Asia cited (248–168 Ma for the East China Slab, 178–110 Ma for the Mongolia Slab and 80–present day for the Manchuria) by Van der Meer et al. (2010) were found to disagree with the ages cited by the record of episodic, subduction related magmatism in the Korean Peninsula (Sagong et al., 2005).

Latitudinal profiles through geodynamic model results and tomography models (Figs. 4 and 5) in East Asia show that the Subduction Reference Frame model produces the most inconsistent fit between model output and observed slab locations based on tomography out of the three scenarios tested, emplacing material too far (10–15°) to the west and in a much more discontinuous fashion, especially in the lower mantle (2000–2500 km). From the P-wave models, both the Hybrid Paleomagnetic and the Hybrid
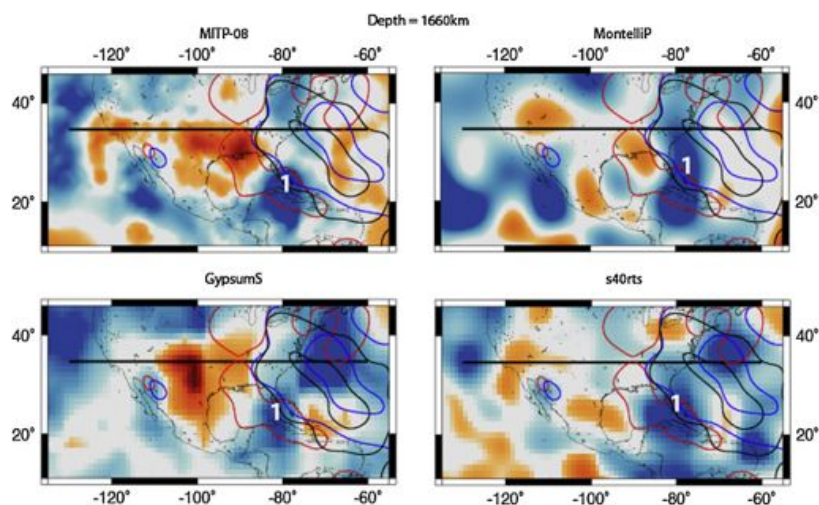

Fig. 3. Horizontal depth slices through tomography in the North American region at 1658 km depth. Contours same as Fig. 2. Anomaly 1 represents subducted Farallon oceanic lithosphere. The subduction reference frame model places material too far to the west compared to the other models and tomography.
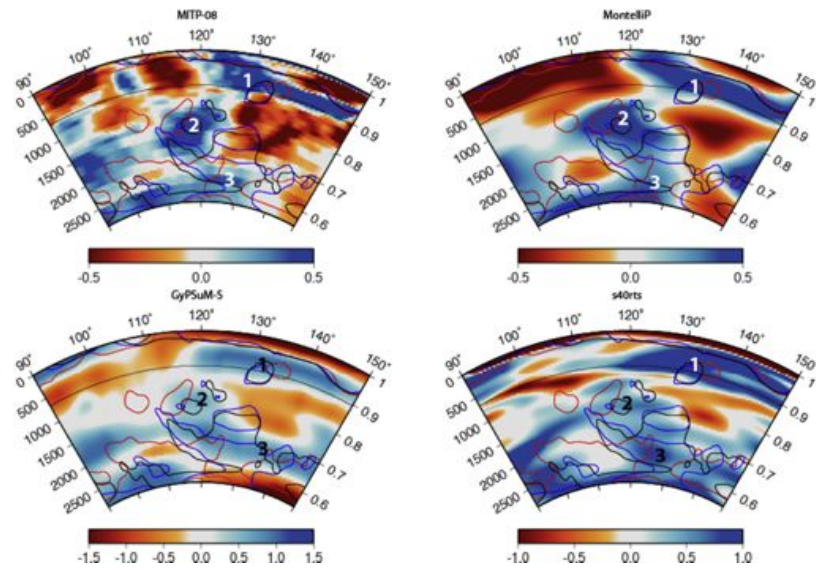
Fig. 4. Vertical cross sections at 48° N. Contours same as Fig. 2. Anomaly 1 represents Pacific material subducted after the Izanagi slab window formation (the Manchuria slab). Anomalies labeled 2 represent Izanagi material subducted prior to ridge subduction (the Mongolian slab). Anomalies labeled 3 represent older Izanagi material subducted between 197 and 158 Ma (the East China slab).

TPW Paleomagnetic model appear to emplace material slightly too far westward (~2–5°) at mid-mantle depths (1500–2000 km). However the S-wave models image fast anomalies here, indicating that relying on one tomography model can lead to erroneous conclusions.

3.1.3. Tethyan domain

The onset of subduction of the Neo-Tethyan Ocean slabs in the Mediterranean region is relatively well constrained. Initiation of subduction (i.e. the base of the Aegean Tethys slab) is dated using the obduction of the Vardar ophiolite complex in Greece at 168.5 ± 2.4 to 172.9 ± 3.1 Ma (Liati et al., 2004), the same geological

evidence used by Van der Meer et al. (2010). While the area is characterized by long-lived subduction, the regional mantle is quite heterogeneous, representing many different slab segments, with the slab associated with the Vardar ophiolites being spatially linked. As subduction is still currently ongoing in this area, dating the top of the slab is not required.

Van der Meer et al. (2010) identifies three independent slabs, the Himalayan, Maldives and Mesopotamia slabs, to represent subducted Neo-Tethyan lithosphere. The Himalayan slab is composed of material subducted between the docking of Burma (Heine et al., 2004) (~80 Ma) and the India Eurasia collision (~30 Ma). Our interpretation does not differ significantly from that of Van der
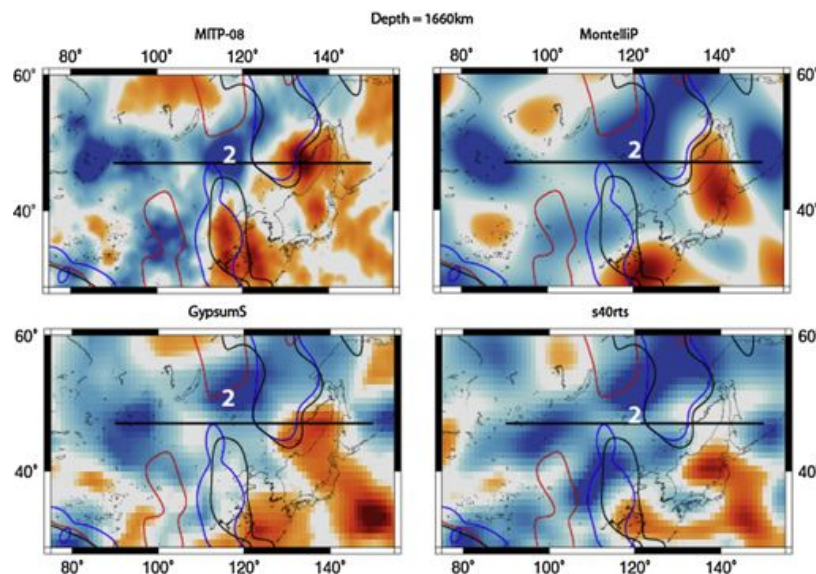

Fig. 5. Horizontal depth slices from tomography in the East Asian region at 1658 km depth. Contours same as Fig. 2. The Subduction Reference Frame model places material too far to the west compared to the other models and tomography.

Meer et al. (2010), who place inception at 85–79 Ma and cessation at 44–20 Ma. The Maldives slab formed from subduction of Meso-Tethyan lithosphere commencing with the docking of Tibet (~180 Ma) and ceasing with the docking of Burma and possible back arc spreading (Aitchison et al., 2007) prior to the India–Eurasia collision (~90–75 Ma). Previous interpretations place subduction inception at 220–200 Ma and cessation between 71 and 57 Ma (Van der Meer et al., 2010). The Mesopotamian slab formed from subducted Meso-Tethyan material that subducted to the northeast of the Maldives slab. We suggest that subduction began later here, with inferred subduction inception occurring ~165 Ma, based on the kinematic model by Müller et al. (2008), which differed from the Van der Meer et al. (2010) interpretation (subduction beginning between 220 and 200 Ma). The cessation of subduction is dated based on the obduction of the Semail ophiolite complex at approximately 79 Ma (Warren et al., 2003).

The central Indian Ocean profile (Figs. 6 and 7) images northward subducted Tethyan oceanic lithosphere, previously studied by Van der Voo et al. (1999a). The exact tectonic evolution of this area remains disputed (Aitchison et al., 2007; Lee and Lawver, 1995; Zahirovic et al., 2012), with alternate scenarios advocating fundamentally different pre-collision margin geometries. While this makes direct comparison of modeled slabs to tomography difficult, comparison of the distribution of material in the deep/mid mantle produced by different absolute rotations is possible. The Subduction Reference Frame model fits the tomography best, with the Hybrid Paleomagnetic model and Hybrid TPW Paleomagnetic model emplacing no material in the southern portion of the mid mantle (between 1000 and 2000 km and −10°S to 0°). When the horizontal extent of geodynamic model slab material at 2090 km is considered, it becomes apparent that the southern lower mantle material present in the Subduction Reference Frame model profile (anomaly 1, Fig. 7) originates from subduction along the western margin of the junction between the eastern Neo-Tethys and the Panthalassic Ocean (Seton and Müller, 2008). The geometry of this plate is poorly constrained as no geological evidence remains, so this match between slab positions resulting from the Subduction Reference Frame model with tomography provides valuable insights in determining paleo plate positions.

3.1.4. Central Asia

The deep mantle beneath central Asia is host to well constrained subducted material from the ancient Mongol-Okhotsk ocean basin that existed during the early-mid Mesozoic between the Siberia craton and the North and South China blocks. The slabs underneath central Asia have been studied previously (Van der Voo et al., 1999b). The timing of closure for the Mongol-Okhotsk ocean is constrained by the suture zone between Siberia and the North China block, placing the cessation of subduction at approximately 150 Ma Kravchinsky et al., 2002; Van der Voo et al., 1999b, later than that inferred by Van der Meer et al. (2010) (180–155 Ma). However, onset of subduction of the Mongol-Okohtsk ocean remains elusive and, and as slab material lies along the CMB, age estimates inferred from sinking rates are likely to be erroneous due to cessation of sinking and lateral spreading along this chemical boundary.

3.1.5. North Pacific

The Circum North Pacific is the location of complex long-lived subduction. Van der Meer et al. (2010) interpret 5 different slabs in this area: The Aleutian, Beaufort, Chuckchi, Kamchatka and Sakhalin slabs. The Aleutian slab is composed of Pacific material subducted northwards since approximately ~50 Ma (Gorbatov et al., 2000; Qi et al., 2007). This interpretation differs slightly from the 84 to 52 Ma subduction beginning inferred by Van der Meer et al. (2010). The Beaufort slab formed due to subduction along the northeastern Eurasian margin, between ~200 and ~155 Ma

(Nokleberg et al., 2000), roughly the same as inferred by Van der Meer et al. (2010). The Chuckchi slab formed from material subducted between the inception of the Koyukuk arc (~160 Ma Nokleberg et al., 2000) and the subduction of the Izanagi-Farallon ridge and subsequent transform margin formation at ~130 Ma. Previous interpretations of subduction cessation were between 120 and 100 Ma (Van der Meer et al., 2010). The Sakhalin and Kamchatka slabs are the result of spatially linked subduction events along the Asian-Arctic margin, with subduction beginning at ~65 Ma for the Sakhalin slab and ~60 Ma for the Kamchatka slab (inferred from the convergence history based on the topological plate polygons/rotations for this region (Clark and Müller, 2008; Gurnis et al., 2012). The Sakhalin slab terminated subduction shortly after this with the subduction of the northernmost portion of the Izanagi-Pacific ridge at ~50 Ma (Whittaker et al., 2007), while the Kamchatka subduction continues to the present day. This differs substantially from previous interpretations, which placed subduction initiation between 100 and 84 Ma for both slabs (Van der Meer et al., 2010).

Unintentionally, the reinterpreted slabs are mostly confined to the northern hemisphere and under continental crust. Most likely this is due to the better-resolved tomography in the northern hemisphere and the geological constraints available in these regions. There is no reason for a significant difference between north and south hemisphere sinking rates.

4. Discussion of geodynamic models

Agreement between geodynamic model output and seismic tomography in both the upper and lower mantle is only moderate-low (Figs. 2–7). This is most likely due to both the complexity of the tomography and the relative simplicity of the modeling code, where downwellings are modeled symmetrically. This is especially evident along the East Asia Subduction zone (Fig. 4). As we aim to assess the global models however, moderate-low agreement is sufficient. It is also evident along the Farallon Subduction zone, where none of the models emplace material where it is observed in the mid-mantle (Fig. 2). This could be due to the effects of flat slab subduction, which has not been included in the model. Another thing which contributes to the mismatch between the model output and tomography is errors in the input plate kinematic reference frame, suggesting that reference frame refinement is necessary. This is also possibly evident below East Asia (Figs. 4 and 5), where the modeled results don't reproduce the extent of the tomographically inferred slabs very well. However, because geodynamic model results do reproduce the location to some extent, this indicates that kinematic model refinement is required, especially in the pre-83.5 Ma Pacific basin.

The primary difference between geodynamic model output stems from the different input absolute reference frame paleo-longitude of subduction zone locations. This is apparent in the geodynamic model output, as the locations of subduction zones mark the areas of convergence and hence slab sinking. The heterogeneity in subduction zone paleo-longitudinal position at 140 Ma, the age at which our plate models begin, can be seen in Fig. 1.

The locations of subducted material in the upper mantle resulting from modeling all three absolute reference frames are very similar. Using an intersecting polygon analysis (Shephard et al., 2012, SOM) we quantify the relative location of geodynamic model slab material. We find overlap of slab material for the Hybrid Paleomagnetic and the Hybrid TPW geodynamic models with the Subduction Reference Frame model to be 77% and 75%, respectively. Similarities are expected because longitudinal differences between the alternate absolute reference frames in the Cenozoic are not large. During the Cenozoic, both the Hybrid Paleomagnetic and
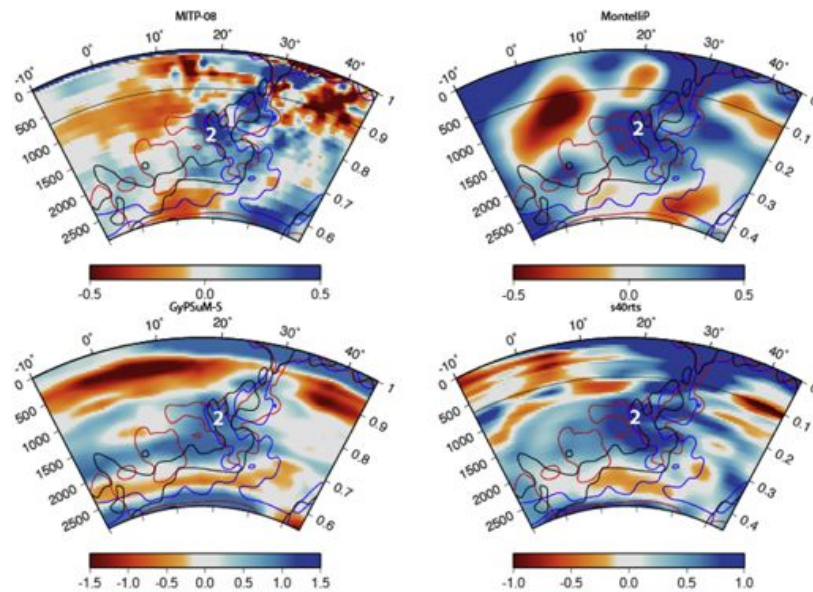
Fig. 6. Vertical cross sections at 80° E. Anomaly 2 represents material subducted prior to the closing of the Tethys Ocean. Contours same as Fig. 2.

Hybrid TPW Paleomagnetic model utilize moving hotspots, while the Subduction Reference Frame model uses the same rotations only slightly corrected to place surficial geological data above the anchor slabs. Further back in time (i.e. 80–140 Ma), in several areas with sufficiently well resolved plate kinematic constraints, such as East Asia and Western North America, the Subduction Reference Frame model fails to reproduce first order tomographic observations accurately (Figs. 2 and 4). The longitudinal corrections resulting from the Van der Meer et al. (2010) approach during the mid-late Cretaceous are likely too large, as such the Subduction Reference Frame model places anchor slab material between 8–12° too far westward compared to the equivalent slab positions from seismic tomography. The Hybrid Paleomagnetic and Hybrid TPW Paleomagnetic model result in an average of 6–9° westerly offsets from seismic tomography.

By considering subduction in a fully convecting mantle we build upon simple correlation of subduction/paleo subduction zones and tomographically interpreted slabs. Lateral slab motion induced by this flow would be greatest in the upper-mantle low-viscosity zone, and the lowermost mantle due to slab pile-up and spreading along the CMB. Similar studies on the effect of variable viscosity on 3 dimensional convection show that rms velocities (and thus lateral slab migration) are highest in the lowermost and uppermost mantle (Tackley, 1996).

Evidently, the plate reconstruction input into the geodynamic models dictates the evolution of the slabs. The apparent agreement between tomography and geodynamic modeling suggests that the comparison between the two can help us understand slab dynamics. However, the mismatch between the two in some locations implies that the initial reconstructions may require amendment.

5. Slab sinking

While deep mantle anomalies interpreted as subducted slabs do offer the best possible constraint on absolute plate motion, errors can easily arise if the wrong sinking velocities are used. This becomes readily apparent when maps of mantle tomography and plate reconstructions are superimposed. If regional sinking rates differ from global average rates, as is the case in many regions

(Fukao et al., 2009; Sigloch, 2011; Supplementary Information), no one depth slice accurately represents a particular geological time. The Subduction Reference Frame we tested relied on rotating surficial evidence of subduction over interpreted mantle velocity anomalies, relying on three primary anchor slabs, the Farallon, Aegean Tethys and Mongol-Okhotsk slabs (Van der Meer et al., 2010). Subduction history at each of these areas is complicated and associated with different sinking rates ranging from 8 to 15 mm/yr. As the Mongol-Okhotsk slab lies along the CMB, it is likely to have a slower than average sinking rate due to it being basally supported, and is likely to have spread laterally along the CMB. Previous studies also indicate that sinking rates in this area are lower than average (~10 mm/yr) (Van der Voo et al., 1999b). The Aegean Tethys slabs location and age of subduction initiation indicates a sinking rate of ~12 mm/yr, while the Farallon slabs depth and age implies a sinking rate of ~14 mm/yr (Tables 2–4). While these sinking rates are based on a simple age-depth correlation, they illustrate the possible differences in age of any single depth slice.

Inferences about slab sinking are apparent when considering tomography and our modeling results. Owing to the large viscosity contrast between the upper and lower mantle, at least two different depth-dependent sinking rates are evident (Conrad and Lithgow-Bertelloni, 2002; Goes et al., 2008; Hafkenscheid et al., 2006; Jarvis and Lowman, 2007; Marton et al., 1999; Morra et al., 2010; Stegman et al., 2010a,b,a,b,a,b). Under ideal conditions, initial slab sinking velocity is determined by negative buoyancy and viscosity of the surrounding mantle. Therefore the velocity at which a plate advances at the surface is close to the density-driven sinking velocity (Goes et al., 2008; Hafkenscheid et al., 2006; Lithgow-Bertelloni and Richards, 1998; Ricard et al., 1993; Schellart, 2004). However, observations from seismic tomography indicate that slabs sinking vertically and penetrating into the lower mantle through the transition zone without delay is commonly not the case, with both partial penetration and build up of material (slab stagnation) being observed (Fukao et al., 2009; Sigloch, 2011; Stegman et al., 2010a,b). Modeling suggests that trench migration is a key factor influencing slab penetration into the lower mantle (Christensen, 1996; Griffiths et al., 1995; Guillou-Frottier et al., 1995) and that material can stagnate along this boundary for tens of millions of years until
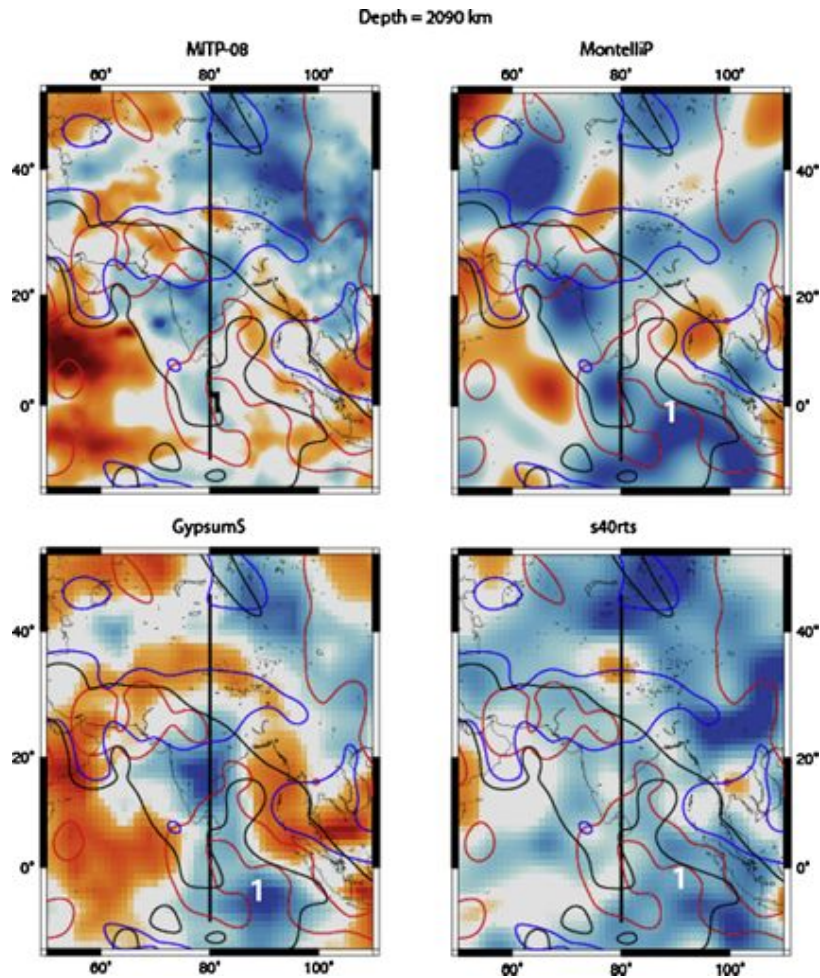
Fig. 7. Horizontal slices from tomography of the Indian region at 2093 km depth. Anomaly 1, representing material subducted beneath the east dipping Junction Subduction zone, is far more offset to the east in the Subduction Reference Frame model. Anomaly 2 is placed at a similar position in all three models. Contours same as Fig. 2.

enough material builds up and a 'mantle avalanche' occurs (Tackley et al., 1993; Pysklywec and Mitrovica, 1998). Differential sinking in adjacent areas has been noted in the North American mantle, with interpreted younger slab segments being observed deeper than older fragments due to the bistable nature of the transition zone (Sigloch, 2011). Numerous mechanisms have been proposed to cause heterogeneity of slab morphology in the upper mantle, from the Stokes buoyancy and flexural stiffness of the subducting plate (Stegman et al., 2010a,b,a,b,a,b), trailing edge boundary conditions and slab width (Stegman et al., 2010a,b,a,b), slab dip angle, possible lateral differences in rheological strength (Sigloch, 2011) and plume slab interaction (Obrebski et al., 2010).

Sinking velocities in the mantle are strongly influenced by a viscosity jump of between 1 and 3 orders of magnitude between the upper and lower mantle (Goes et al., 2008; Hafkenscheid et al., 2006; Jarvis and Lowman, 2007; Marton et al., 1999; Morra et al., 2010; Ricard et al., 1993; Stegman et al., 2010a,b,a,b,a,b; Van der Meer et al., 2010). Numerous techniques have been used to approximate the effect of this viscosity jump on plate sinking velocity. Lithgow-Bertelloni and Richards (1998) use a relationship between upper and lower mantle sinking velocity, where lower mantle sinking velocities were obtained from the formula $v_T = (1/s)v_C$, where v_T is the slab's terminal velocity, s is the slowing factor, and v_C is

the plate convergence rate. The slowing factor, s, is taken as proportional to the natural logarithm of the viscosity contrast between the upper/lower mantle based on theoretical convection studies with depth dependent viscosity (Gurnis and Davies, 1986; Richards et al., 1991; Ricard et al., 1993). This commonly leads to lower mantle slab sinking rates on the order of 10–30 mm/yr, which agrees with other approaches (Goes et al., 2008; Hafkenscheid et al., 2006; Lithgow-Bertelloni and Richards, 1998; Ricard et al., 1993; Stegman et al., 2010a,b,a,b,a,b). Higher rates of slab sinking are associated with areas of abundant subduction (Stegman et al., 2010a,b,a,b,a,b). Steinberger (2000) uses seismic heterogeneity in the lowermost mantle in concordance with Mesozoic and Cenozoic Subduction history to conclude that it takes on the order of 120 Myr for slabs to reach the core mantle boundary (CMB), suggesting lower mantle sinking rates of around 17 mm/yr. A reduction of sinking speed by a factor of 4 upon entering the lower mantle is used by Schellart et al. (2009) to compute sinking rates in accordance with Lithgow-Bertelloni and Richards (1998) and a rate of 15 mm/yr was obtained. As a separate test, the velocity of a sinking oblate ellipsoid, $v_E = ((SD^2g(\rho_S - \rho_M))/(18\mu_{LM}))$ (Kerr and Lister, 1991), can be used to evaluate mantle sinking rates (where v_E is the velocity of an oblate spheroid, $D = (abc)^{1/3}$ where a, b, and c are the ellipsoid axes, S is a shape factor relating to the physical dimensions of the ellipsoid also
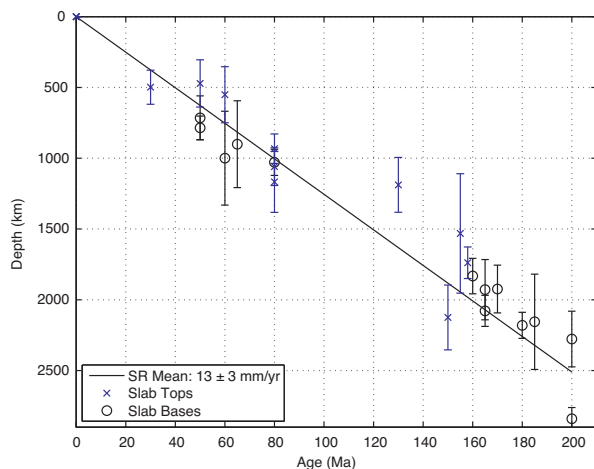
Fig. 8. Age-depth plot of reinterpreted slab depths and ages (Tables 2–4) in the lower mantle. The line of best fit reflects an average fit to all model interpretations, leading to an average sinking rate of 13 ± 3 mm/yr, slightly faster than the rate of 12 mm/yr proposed by Van der Meer et al. (2010). Depth errors are standard deviations of all the tomography models' slab depths (Supplementary Information). Age errors are poorly constrained by the literature, and thus are not considered.

depending on a, b, and c, $\rho_S - \rho_M$ is the density contrast between slab and mantle, and μ_{LM} is the viscosity of the lower mantle). Schellart et al. (2009) applied this relationship to the South Loyalty slab, yielding a sinking velocity of 13 mm/yr, which is close to that based on the Lithgow-Bertelloni and Richards (1998) method.

5.1. Sinking rates from geological evidence

Numerous authors have attempted to estimate average sinking velocities using the spatial distributions of deep mantle slabs and their relation to surface geology features (Hafkenscheid et al., 2006; Van der Meer et al., 2010; Van der Voo et al., 1999a,b). Examination of the tomgraphically imaged and geologically constrained slabs (Tables 2–4) yields a global average sinking rate in the entire mantle of 13 ± 3 mm/yr (Fig. 8). The error presented is the standard deviation of individual slab sinking rates. Stratified sinking rates that depend on a sinking rate reduction of approximately 4 at the upper/lower mantle transition zone (e.g. 52 mm/yr in the upper mantle compared to 13 mm/yr in the lower mantle) (Lithgow-Bertelloni and Richards, 1998; Schellart et al., 2009) place material far deeper than what is observed, especially in the upper to upper-mid mantle. This implies that either sinking rates in the upper mantle do not approximate plate convergence rates as commonly proposed in the literature (Goes et al., 2008; Hafkenscheid et al., 2006; Lithgow-Bertelloni and Richards, 1998; Ricard et al., 1993; Schellart, 2004) or more likely that slab stagnation in the transition zone has a significant effect on slab transit (Marton et al., 1999). This slab stagnation is apparent from examining many mantle provinces, especially the western Pacific and under North America (Fukao et al., 2009; Sigloch, 2011). While material may be sinking at rates comparable to plate velocity at the surface, the stalling and bending observed in high resolution tomography suggests significant resistance in slab transit. This has implications for attempting to use lower mantle slabs to constrain absolute plate motion: only slabs with a well-constrained history of sinking should be utilized for applying longitudinal corrections.

Upper/lower mantle viscosity contrast and initial slab geometry have the largest effect on increasing slab survival time within the mantle (Jarvis and Lowman, 2007). It follows that if there is a significant viscosity contrast between the upper and lower

mantle then slabs at least as old as 140 Myr could be visible. Thermal equilibration of slabs with adjacent mantle must also be taken into consideration. Van der Meer et al. (2010) also consider tomographic visibility and based on their reconstructions of past subduction zones, come to the conclusion that there are no slabs in the mantle older than approximately 300 Ma. When attempting to infer sinking rates from geological information, it is important to take into account the time it takes for slabs to sink all the way to the core mantle boundary (CMB). If mantle overturn time is shorter than the equilibration time, slabs will spread laterally along the core mantle boundary. Ricard et al. (1993) assume that thermal diffusion will not alter the long wavelength scale of mantle rocks on their timescale of interest (100–200 Myr) as the thermal diffusive length scale for 100 Myr is only on the order of 100 km.

The apparent misfit of higher upper mantle sinking rates, especially in the upper to upper-mid mantle (i.e. in the Tethys and Circum North Pacific) could be a manifestation of a number of processes. Slab material stalling at the transition zone is not accounted for in sinking rate calculations and could lead to a significant delay in sinking, possibly masking the faster upper mantle sinking rate. For example, if material were to stall in the transition zone for 10 Myr, this would imply subducted material of a given age would be 130 km shallower as compared to material passing through the transition zone without retardation (assuming a lower mantle sinking rate of 13 mm/yr). If material were to stall for 20 Myr, a plausible estimate given prior modeling (Pysklywec and Mitrovica, 1998), this would place material 260 km higher in the mantle. Our geodynamic models place slab material on the order of 100–300 km deeper than corresponding slabs inferred from tomography, suggesting that these stalling times need to be taken into account.

A possible viscosity change in the lower mantle between 1200 and 1500 km has been proposed, caused by a chemical phase transition of ferropericlase (Forte and Mitrovica, 2001; Morra et al., 2010). If this exists, we would expect to see a bend in the age-depth plot at this depth. Our results indicate that if this boundary exists it is not offering significant resistance to sinking slabs. To increase the robustness of this observation, more slabs in this proposed transition zone area would need to be studied.

The apparent fit of a globally uniform mantle sinking rate of 12 mm/yr in both the upper and lower mantle as proposed by Van der Meer et al. (2010) is due to the selection of dates used for the base and tops of slabs. The age-depth curve of Van der Meer et al. (2010) assigns ages of greater than 240 Myr to eight slabs that lie along the CMB. As material along this boundary stops sinking and flows laterally once reached, assigning older dates of deep material will skew the average sinking rate. Fig. 8 shows an age-depth curve, with only reinterpreted slabs used (Tables 2–4). This interpretation shows that average mantle sinking rates inferred from geological data alone are slightly greater than Van der Meer et al. (2010). That being said, due to complex sinking histories of well-imaged slabs (i.e. the Farallon, East Asian etc) global averages are insufficient for constraining absolute plate motion. Rather regional sinking rates should be used.

Other studies support the view that sinking rates need to be assessed on a regional basis, showing that lower mantle sinking varies regionally between approximately 10–20 mm/yr (Schellart et al., 2009; Van der Voo et al., 1999a,b). Indeed Schellart and Spakman (2012) use tomography and reconstructions to infer that sinking rates can vary even along individual subduction zones with upper mantle rates varying between 30 and 70 mm/yr and lower mantle sinking rates varying between 8 and 18 mm/yr along the Solomon-Vitiaz-Tonga-Kermadac-Hikurangi subduction zone. 13 mm/yr is a good approximation for a whole mantle sinking rate, as 20 mm/yr implies a much quicker mantle turnover (on the order of 130 Myr, compared to approximately 200 Myr inferred by a slower sinking rate). Geodynamic modeling using a viscosity

contrast of two orders of magnitude between the upper and lower mantle implies that mantle turnover of 130 Myr is not realistic, as modeling results using 130 Ma of plate history suffer from artifacts in the lowermost mantle, and inferences from using a mantle sinking rate derived from geological data alone indicate that 20 mm/yr is too high, placing material significantly deeper than observed. While sinking is sub-vertical due to the global flow dynamics, it is largely representative of natural sinking behaviors. Following this, sinking velocities from the geodynamic model used in this study were found to be on average ~50 mm/yr in the upper mantle and between ~15–20 mm/yr in the lower mantle. These values imply that material aged 140 Myr will be found between ~2600 km – CMB, thus depth comparisons with models starting at 140 Ma and tomography is suitable. Lateral slab motion introduced by considering slab sinking in a fully convecting mantle is known to be negligible, especially in the mid mantle. In the upper mantle, due to a low viscosity asthenosphere, and in the lowermost mantle due to slab pileup and spreading along the CMB, some lateral motion is expected (Bunge et al., 1997).

While including variable effects such as phase transitions at 410 and 660 km will potentially lead to more slab stagnation, they are deliberately not included in this study as the appropriate Clapeyron slopes for a global model are not trivial due to the multiphase nature of downwelling material (Marton et al., 1999). Both the geological evidence and the flow dynamics inherent in our geodynamic models are consistent with a lower mantle two orders of magnitude more viscous than the upper mantle, and that a factor of 30 increase in viscosity between the upper and lower mantles previously used is not enough (Becker and Boschi, 2002; Liu et al., 2008). This is also consistent with geoid modeling studies of mantle viscosity structures (Lee et al., 2010; Schaber et al., 2009), which also indicate that a two order of magnitude difference between upper and lower mantle and a lower mantle viscosity of 10^{23} Pa s is realistic.

6. Conclusions

Three plate kinematic models have been used as input for three alternative geodynamic mantle convection simulations. The resulting output has been compared with four present-day mantle tomography models with the intention of improving our understanding of slab sinking dynamics in the mantle. All three geodynamic models produce westerly offsets compared with seismic tomography, with offsets increasing with depth, with the Subduction Reference Frame model producing the greatest misfits in the lower mantle. However, disagreement of slab material location between tomography, geodynamic models, and kinematic models, may imply poor absolute and relative plate motion constraints, slabs not sinking vertical, and poor resolution tomography, or a combination of these. Model results indicate that while subduction zone location is important in determining modeled mantle structure, plate velocity and hence slab input rates into the mantle are critical. Deciphering the depth of any particular slab is not straightforward, as the evolution of the slab since subduction is complicated; thus regional variations in slab sinking rates must be taken into account to avoid spurious global age-depth relationships. We have evaluated subducted slab sinking rates by combining alternative plate kinematic models, geological observations, mantle tomography, and geodynamic models. Our results converge on a globally averaged mantle sinking rate of 13 ± 3 mm/yr. Sinking rates from geodynamic modeling of 15–20 mm/yr indicate that rates of this magnitude are reasonable. Both the results from the geological data and modeling indicate that a viscosity contrast of two orders of magnitude between the upper and lower mantle is reasonable.

Appendix A. Supplementary data

Supplementary data associated with this article can be found, in the online version, at http://dx.doi.org/10.1016/j.jog.2013.10.006.

References

Aitchison, J.C., Ali, J.R., Davis, A.M., 2007. When and where did India and Asia collide. J. Geophys. Res. 112, B05423.

Amaru, M., 2007. Global travel time tomography with 3-D reference models. Utrecht University, pp. 1–174 (Ph.D. Thesis).

Becker, T.W., Boschi, L., 2002. A comparison of tomographic and geodynamic mantle models. Geochem. Geophys. Geosyst. 3, 1003.

Bunge, H.-P., 2005. Low plume excess temperature and high core heat flux inferred from non-adiabatic geotherms in internally heated mantle circulation models. Phys. Earth Planet. Inter. 153, 3–10.

Bunge, H.-P., Baumgardner, J.R., 1995. Mantle convection modeling on parallel virtual machines. Comput. Phys. 9, 207–215.

Bunge, H.-P., Richards, M.A., Baumgardner, J.R., 1996. Effect of depth-dependent viscosity on the planform of mantle convection. Nature 379, 436–438.

Bunge, H.-P., Richards, M.A., Baumgardner, J.R., 1997. A sensitivity study of three-dimensional spherical mantle convection at 108 Rayleigh number: effects of depth-dependent viscosity, heating mode, and an endothermic phase change. J. Geophys. Res. 102, 11991–12007.

Bunge, H.-P., Richards, M.A., Baumgardner, J.R., 2002. Mantle-circulation models with sequential data assimilation: inferring present-day mantle structure from plate-motion histories. Philos. T. R. Soc. A 360, 2545–2567.

Christensen, U.R., 1996. The influence of trench migration on slab penetration into the lower mantle. Earth Planet. Sci. Lett. 140, 27–39.

Clark, S.R., Müller, R.D., 2008. Convection models in the Kamchatka region using imposed plate motion and thermal histories. J. Geodyn. 46, 1–9.

Conrad, C.P., Lithgow-Bertelloni, C., 2002. How mantle slabs drive plate tectonics. Science 298, 207–209.

DeCelles, P.G., Ducea, M.N., Kapp, P., Zandt, G., 2009. Cyclicity in Cordilleran orogenic systems. Nat. Geosci. 2, 251–257.

Doubrovine, P.V., Steinberger, B., Torsvik, T.H., 2012. Absolute plate motions in a reference frame defined by moving hot spots in the Pacific, Atlantic, and Indian Oceans. J. Geophys. Res. 117, B09101.

Forte, A.M., Mitrovica, J.X., 2001. Deep-mantle high-viscosity low and thermo-chemical structure inferred from seismic and geodynamic data. Nature 410, 1049–1056.

Fukao, Y., Obayashi, M., Nakakuki, T., 2009. Stagnant slab: a review. Annu. Rev. Earth Planet. Sci. 37, 19–46.

Goes, S., Capitanio, F.A., Morra, G., 2008. Evidence of lower-mantle slab penetration phases in plate motions. Nature 451, 981–984.

Gorbatov, A., Widiyantoro, S., Fukao, Y., Gordeev, E., 2000. Signature of remnant slabs in the North Pacific from P wave tomography. Geophys. J. Int. 142, 27–36.

Grand, S.P., 1994. Mantle shear structure beneath the Americas and surrounding oceans. J. Geophys. Res. 99, 11591–11621.

Griffiths, R.W., Hackney, R.I., van der Hilst, R.D., 1995. A laboratory investigation of effects of trench migration on the descent of subducted slabs. Earth Planet. Sci. Lett. 133, 1–17.

Guillou-Frottier, L., Buttles, J., Olson, P., 1995. Laboratory experiments on the structure of subducted lithosphere. Earth Planet. Sci. Lett. 133, 19–34.

Gurnis, M., Davies, G.F., 1986. The effect of depth dependent viscosity on convective mixing in the mantle and the possible survival of primitive mantle. Geophys. Res. Lett. 13, 541–544.

Gurnis, M., Turner, M., Zahirovic, S., DiCaprio, L., Spasojevic, S., Müller, R., Boyden, J., Seton, M., Manea, V., Bower, D., 2012. Plate Tectonic Reconstructions with Continuously Closing Plates. Comput. Geosci. 38, 35–42.

Hafkenscheid, E., Wortel, M.J.R., Spakman, W., 2006. Subduction history of the Tethyan region derived from seismic tomography and tectonic reconstructions. J. Geophys. Res. 111, B08401.

Hager, B.H., Richards, M.A., 1989. Long-wavelength variations in Earth's geoid: physical models and dynamical implications. Philos. T. R. Soc. Lond. A 328, 309–327.

Heine, C., Mülller, R.D., Gaina, C., 2004. Reconstructing the lost eastern Tethys ocean basin: convergence history of the SE Asian margin and marine gateways. Geoph. Monogr. Ser. 149, 37–54.

Jarvis, G.T., Lowman, J.P., 2007. Survival times of subducted slab remnants in numerical models of mantle flow. Earth Planet. Sci. Lett. 260, 23–36.

Kennett, B.L.N., Engdahl, E.R., Buland, R., 1995. Constraints on seismic velocities in the Earth from traveltimes. Geophys. J. Int. 122, 108–124.

Kerr, R.C., Lister, J.R., 1991. The effects of shape on crystal settling and on the rheology of magmas. J. Geol. 99, 457–467.

Kravchinsky, V.A., Cogne, J.P., Harbert, W.P., Kuzmin, M.I., 2002. Evolution of the Mongol-Okhotsk Ocean as constrained by new palaeomagnetic data from the Mongol-Okhotsk suture zone, Siberia. Geophys. J. Int. 148, 34–57.

Lee, C.K., Han, S.C., Steinberger, B., 2010. Influence of variable uncertainties in seismic tomography models on constraining mantle viscosity from geoid observations. Phys. Earth. Planet. In. 184, 51–62.

Lee, T.Y., Lawver, L.A., 1995. Cenozoic plate reconstruction of Southeast Asia. Tectonophysics 251, 85–138.

Lévêque, J.J., Rivera, L., Wittlinger, G., 1993. On the use of the checker-board test to assess the resolution of tomographic inversions. Geophys. J. Int. 115, 313–318.

Li, C., van der Hilst, R.D., Engdahl, E.R., Burdick, S., 2008. A new global model for P wave speed variations in Earth's mantle. Geochem. Geophys. Geosyst. 9, 1–21.

Liati, A., Gebauer, D., Fanning, C.M., 2004. The age of ophiolitic rocks of the Hellenides (Vourinos, Pindos, Crete): first U–Pb ion microprobe (SHRIMP) zircon ages. Chem. Geol. 207, 171–188.

Lithgow-Bertelloni, C., Richards, M.A., 1998. The dynamics of Cenozoic and Mesozoic plate motions. Rev. Geophys. 36, 27–78.

Liu, L., Spasojevic, S., Gurnis, M., 2008. Reconstructing Farallon plate subduction beneath North America back to the Late Cretaceous. Science 322, 934–938.

Marton, F.C., Bina, C.R., Stein, S., Rubie, D., 1999. Effects of slab mineralogy on subduction rates. Geophys. Res. Lett. 26, 119–122.

Montelli, R., Nolet, G., Masters, G., Dahlen, F.A., Hung, S.H., 2004. Global P and PP traveltime tomography: rays versus waves. Geophys. J. Int. 158, 637–654.

Morgan, J.W., 1983. Hotspot tracks and the early rifting of the Atlantic. Tectonophysics 94, 123–139.

Morra, G., Yuen, D.A., Boschi, L., Chatelain, P., Koumoutsakos, P., Tackley, P.J., 2010. The fate of the slabs interacting with a density/viscosity hill in the mid-mantle. Phys. Earth Planet. Inter. 180, 271–282.

Müller, R.D., Sdrolias, M., Gaina, C., Roest, W., 2008. Age, spreading rates, and spreading asymmetry of the world's ocean crust. Geochem. Geophys. Geosyst. 9, Q04006.

Nokleberg, W.J., Parfenov, L.M., Monger, J.W.H., Norton, I.O., Khanchuk, A.I., Stone, D.B., Scotese, C.R., Scholl, D.W., Fujita, K., 2000. Phanerozoic tectonic evolution of the Circum-North Pacific. USGS Professional Paper 1626.

O'Neill, C., Müller, R.D., Steinberger, B., 2005. On the uncertainties in hot spot reconstructions and the significance of moving hot spot reference frames. Geochem. Geophys. Geosyst. 6, Q04003.

Obrebski, M., Allen, R.M., Xue, M., Hung, S.H., 2010. Slab-plume interaction beneath the Pacific Northwest. Geophys. Res. Lett. 37, 1987–2004.

Oeser, J., Bunge, H.-P., Mohr, M., 2006. Cluster design in the Earth Sciences Tethys. In: Gerndt, M., Kranzlmüller, D. (Eds.), High Performance Computing and Communications 4208. Springer, Berlin Heidelberg, pp. 31–40.

Paulson, A., Zhong, S., Wahr, J., 2007. Inference of mantle viscosity from GRACE and relative sea level data. Geophys. J. Int. 171, 497–508.

Pysklywec, R.N., Mitrovica, J.X., 1998. Mantle flow mechanisms for the large-scale subsidence of continental interiors. Geology 26, 687–690.

Qi, C., Zhao, D., Chen, Y., 2007. Search for deep slab segments under Alaska. Phys. Earth Plan. Inter. 165, 68–82.

Ricard, Y., Richards, M., Lithgow-Bertelloni, C., Le Stunff, Y., 1993. A geodynamic model of mantle density heterogeneity. J. Geophys. Res. 98, 21895–21909.

Richards, M.A., Engebretson, D.C., 1992. Large-scale mantle convection and the history of subduction. Nature 355, 437–440.

Richards, M.A., Jones, D.L., DePaolo, D.J., Duncan, R.A., 1991. A Mantle Plume Initiation Model for the Wrangellia Flood Basalt and Other Oceanic Plateaus. Science 254, 263–267.

Ritsema, J., Deuss, A., van Heijst, H.J., Woodhouse, J.H., 2010. S40RTS: a degree 40 shear velocity model for the mantle from new Rayleigh wave dispersion, teleseismic traveltime and normal mode splitting function measurements. Geophys. J. Int. 184, 1223–1236.

Sagong, H., Kwon, S.T., Ree, J.H., 2005. Mesozoic episodic magmatism in South Korea and its tectonic implication. Tectonics 24, TC5002.

Schaber, K., Bunge, H.-P., Schuberth, B.S.A., Malservisi, R., Horbach, A., 2009. Stability of the rotation axis in high-resolution mantle circulation models: Weak polar wander despite strong core heating. Geochem. Geophys. Geosyst. 10, Q11W04.

Schellart, W.P., 2004. Kinematics of subduction and subduction-induced flow in the upper mantle. J. Geophys. Res. 109, 1–19.

Schellart, W.P., Kennett, B.L.N., Spakman, W., Amaru, M., 2009. Plate reconstructions and tomography reveal a fossil lower mantle slab below the Tasman Sea. Earth. Planet. Sci. Lett. 278, 143–151.

Schellart, W.P., Spakman, W., 2012. Mantle constraints on the plate tectonic evolution of the Tonga-Kermadec-Hikurangi subduction zone and the South Fiji Basin. Aust. J. Earth. Sci. 59, 933–952.

Schuberth, B.S.A., Bunge, H.-P., Ritsema, J., 2009a. Tomographic filtering of high-resolution mantle circulation models: Can seismic heterogeneity be explained by temperature alone? Geochem. Geophys. Geosys. 10, Q05W03.

Schuberth, B.S.A., Bunge, H.-P., Steinle-Neumann, G., Moder, C., Oeser, J., 2009b. Thermal versus elastic heterogeneity in high-resolution mantle circulation models with pyrolite composition: High plume excess temperatures in the lowermost mantle. Geochem. Geophys. Geosys. 10, Q01W01.

Seton, M., Müller, R.D., 2008. Reconstructing the junction between Panthalassa and Tethys since the Early Cretaceous. Eastern Australasian Basins III, 263–266.

Shephard, G.E., Bunge, H.-P., Schuberth, B.S.A., Müller, R., Talsma, A., Moder, C., Landgrebe, T.C.W., 2012. Testing absolute plate reference frames and the implications for the generation of geodynamic mantle heterogeneity structure. Earth Planet. Sci. Lett. 317, 204–217.

Sigloch, K., 2011. Mantle provinces under North America from multifrequency P wave tomography. Geochem. Geophy. Geosyst. 12, Q02W08.

Sigloch, K., McQuarrie, N., Nolet, G., 2008. Two-stage subduction history under North America inferred from multiple-frequency tomography. Nat. Geosci. 1, 458–462.

Sigloch, K., Mihalynuk, M.G., 2013. Intra-oceanic subduction shaped the assembly of Cordilleran North America. Nature 496, 50–56.

Simmons, N.A., Forte, A.M., Boschi, L., Grand, S.P., 2010. GyPSuM: A joint tomographic model of mantle density and seismic wave speeds. J. Geophys. Res. 115, 1–14.

Stegman, D.R., Farrington, R., Capitanio, F., Schellart, W.P., 2010a. A regime diagram for subduction styles from 3-D numerical models of free subduction. Tectonophysics 483, 29–45.

Stegman, D.R., Schellart, W.P., Freeman, J., 2010b. Competing influences of plate width and far-field boundary conditions on trench migration and morphology of subducted slabs in the upper mantle. Tectonophysics 483, 46–57.

Steinberger, B., 2000b. Slabs in the lower mantle-results of dynamic modelling compared with tomographic images and the geoid. Phys. Earth Plan. Inter. 118, 241–258.

Steinberger, B., O'Connell, R.J., 1997. Changes of the Earth's rotation axis owing to advection of mantle density heterogeneities. Nature 387, 169–173.

Steinberger, B., Torsvik, T.H., 2008. Absolute plate motions and true polar wander in the absence of hotspot tracks. Nature 452, 620–623.

Steinberger, B., Torsvik, T.H., 2010. Toward an explanation for the present and past locations of the poles. Geochem. Geophys. Geosyst. 11, Q06W06.

Steinberger, B., Torsvik, T.H., Becker, T.W., 2012. Subduction to the lower mantle – a comparison between geodynamic and tomographic models. Solid Earth 3, 415–432.

Styles, E., Davies, D.R., Goes, S., 2011. Mapping spherical seismic into physical structure: biases from 3 D phase transition and thermal boundary layer heterogeneity. Geophys. J. Int. 184, 1371–1378.

Tackley, P.J., Stevenson, D.J., Glatzmaier, G.A., Schubert, G., 1993. Effects of an endothermic phase transition at 670 km depth in a spherical model of convection in the Earth's mantle. Nature 361, 699–704.

Tackley, P.J., 1996. Effects of strongly variable viscosity on three-dimensional compressible convection in planetary mantles. J. Geophys. Res. 101, 3311–3332.

Talagrand, O., 1997. Assimilation of observations: An introduction. J. Meteorol. Soc. Jpn. 75, 191–209.

Tarduno, J.A., Duncan, R.A., Scholl, D.W., Cottrell, R.D., Steinberger, B., Thordarson, T., Kerr, B.C., Neal, C.R., Frey, F.A., Torii, M., 2003. The Emperor Seamounts: southward motion of the Hawaiian hotspot plume in Earth's mantle. Science 301, 1064–1069.

Torsvik, T.H., Müller, R.D., Van der Voo, R., Steinberger, B., Gaina, C., 2008a. Global plate motion frames: toward a unified model. Rev. Geophys. 46, RG3004.

Torsvik, T.H., Steinberger, B., Cocks, L.R.M., Burke, K., 2008b. Longitude: linking Earth's ancient surface to its deep interior. Earth Planet. Sci. Lett. 276, 273–282.

Van der Meer, D.G., Spakman, W., van Hinsbergen, D.J.J., Amaru, M., Torsvik, T.H., 2010. Towards absolute plate motions constrained by lower-mantle slab remnants. Nat. Geosci. 3, 36–40.

Van der Voo, R., Spakman, W., Bijwaard, H., 1999a. Mesozoic subducted slabs under Siberia. Nature 397, 246–249.

Van der Voo, R., Spakman, W., Bijwaard, H., 1999b. Tethyan subducted slabs under India. Earth Planet. Sci. Lett. 171, 7–20.

Ward, P.L., 1995. Subduction cycles under western North America during the Mesozoic and Cenozoic eras. In: Miller, D.M., Busby, C. (Eds.), Jurassic Magmatism and Tectonics of the North American Cordillera. Geol. Soc. Am. Spec. Pap. 299. , pp. 1–45.

Warren, C.J., Parrish, R.R., Searle, M.P., Waters, D.J., 2003. Dating the subduction of the Arabian continental margin beneath the Semail ophiolite, Oman. Geology 31, 889–892.

Wessel, P., Harada, Y., Kroenke, L.W., 2006. Toward a self-consistent, high-resolution absolute plate motion model for the Pacific. Geochem. Geophys. Geosyst. 7, Q03L12.

Whittaker, J.M., Müller, R.D., Leitchenkov, G., Stagg, H., Sdrolias, M., Gaina, C., Goncharov, A., 2007. Major Australian-Antarctic plate reorganization at Hawaiian-Emperor bend time. Science 318, 83–86.

Zahirovic, S., Muller, R.D., Seton, M., Flament, N., Gurnis, M., Whittaker, J., 2012. Insights on the kinematics of the India-Eurasia collision from global geodynamic models. Geochem. Geophys. Geosyst. 13, Q04W11.

Supplementary material for:

Geological, tomographic, kinematic and geodynamic constraints on the dynamics of sinking slabs

Butterworth, N.P., Talsma, A.S., Müller, R.D., Seton, M, Bunge, H.-P., Schuberth, B.S.A., Shephard, G.E., Heine, C.

Qualitative approach to picking slabs

The correlation of surface geological features indicative of subduction with sub-surface seismic tomography anomalies is a difficult process. To constrain the location of slabs, we used an iterative process as follows. We start by defining a slab to be one standard deviation away in the positive direction from any tomography model's median velocity perturbation. This provides us with a quantitative set of positive seismic velocity anomalies, indicative of a subducted slab. We then reconstruct paleo-subduction zones, using age ranges derived from assuming approximate sinking speeds, and correlate voluminous subduction zones with locations of slabs in tomography. Now we use our forward geodynamic models to also infer the location of slab material, and correlate this with slabs in tomography. Where all parcels intersect we may deduce that it is the approximate location of a slab (Figure S1, S2, S3). We perform each step in a 3D environment to constrain the lateral and radial location of a slab (Figure S4). We use 2D cross-sections for all available depth slices to constrain the maximum and minimum location of the slab. Disagreement of slab material location between tomography, geodynamic models, and kinematic models, may imply incorrect assumed sinking rate, poor absolute and relative plate motion constraints, slabs not sinking vertical, and poor resolution tomography, or a combination of these.

To provide subduction volume constraints on apparent slab locations we utilise plate convergence velocities along with an estimate for lithospheric thickness. Convergence velocity is derived from the relative motion of an overriding and subducting plate at each time step in the plate model. Oceanic lithosphere thickness is derived from the paleo-reconstruction model along with sampling age grids with a $1° \times 1°$ resolution (Müller et al., 2008). Using a Half-Space Cooling model truncated at 95 km (after Chapter 4.2 Schubert et al., 2001) the thickness of the lithosphere, z, is determined as

$$z = erf^{-1}\left(\frac{T_l - T_o}{T_m - T_o}\right) 2 \sqrt{\kappa} \sqrt{age},$$ (1)

where, erf^{-1} is the inverse of the error function, $T_l = 1300°C$ and is the isotherm of the lithosphere, $T_o = 0°$ and is the surface temperature, $T_m = 1600°C$ and is the temperature of the mantle, $\kappa = 8 \times 10^{-8}$m/s and is the thermal diffusivity constant, and *age* is the age of the lithosphere sampled from the age grids. We calculate the volume of slab material as the convergence rate times the lithospheric thickness times each subduction segment length (from the resolution of the plate model). This provides a kinematic estimate on the amount of material that is entering the mantle at any given time. Correlation of kinematically estimated slab material and seismic tomography helps to constrain the evolution of a slab (Figure S1, S2, S3).
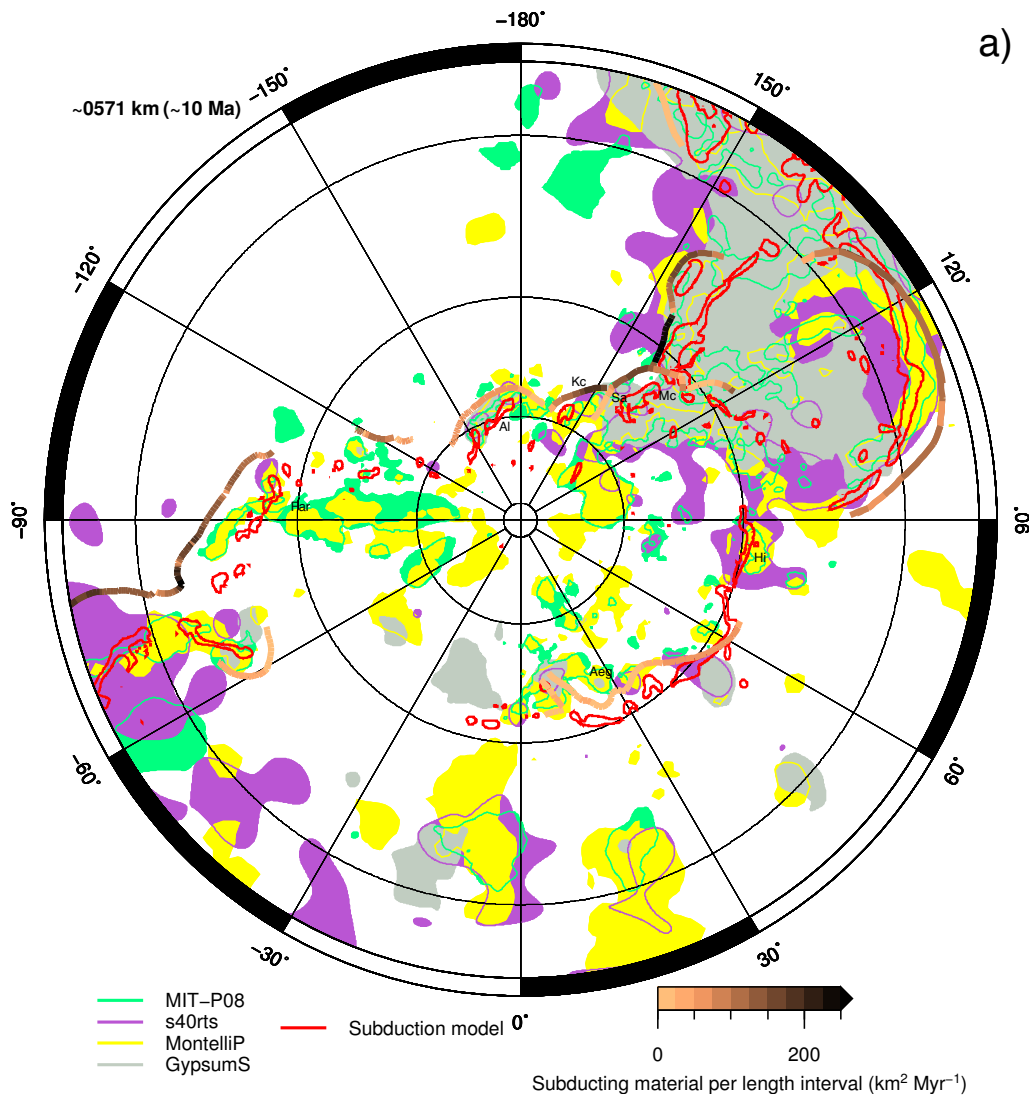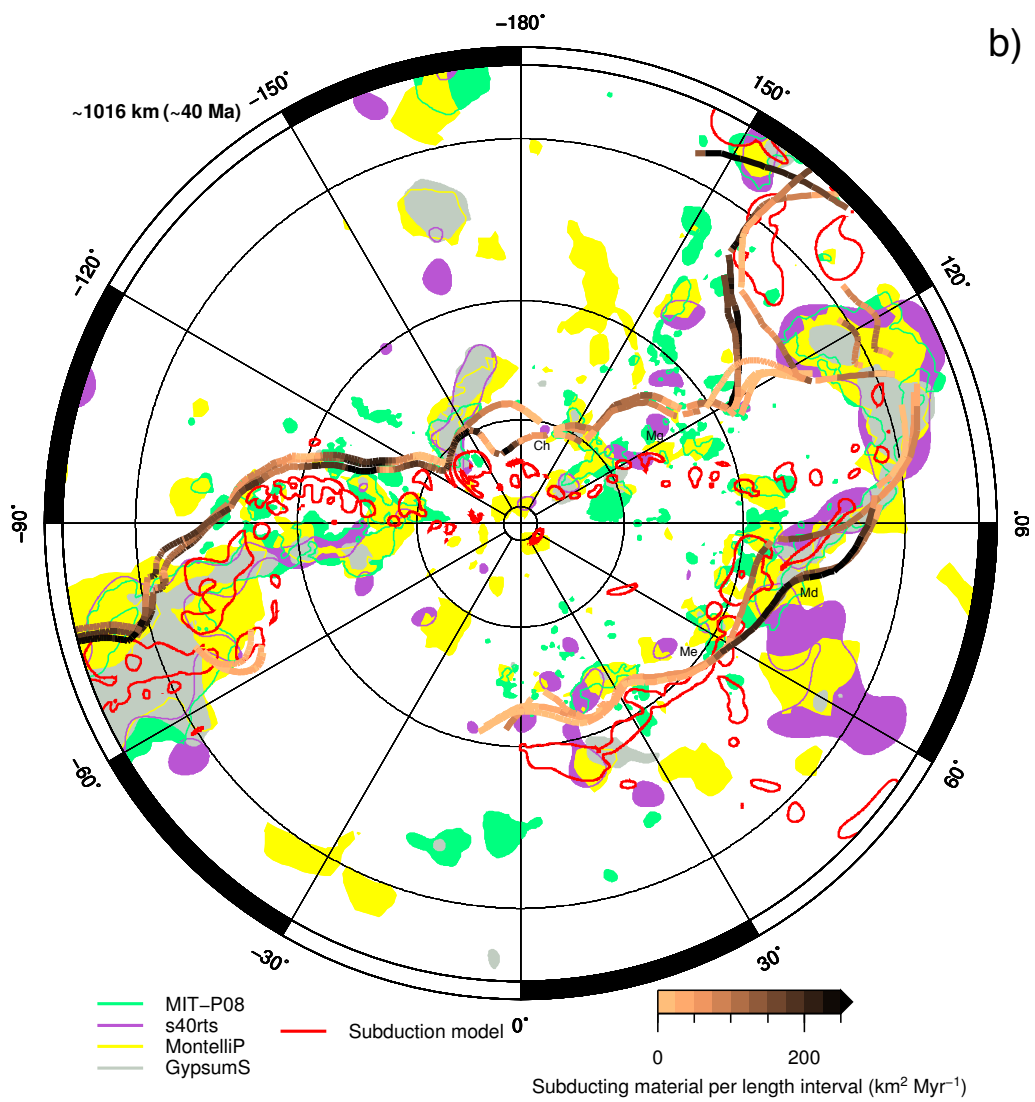
Supplementary figures
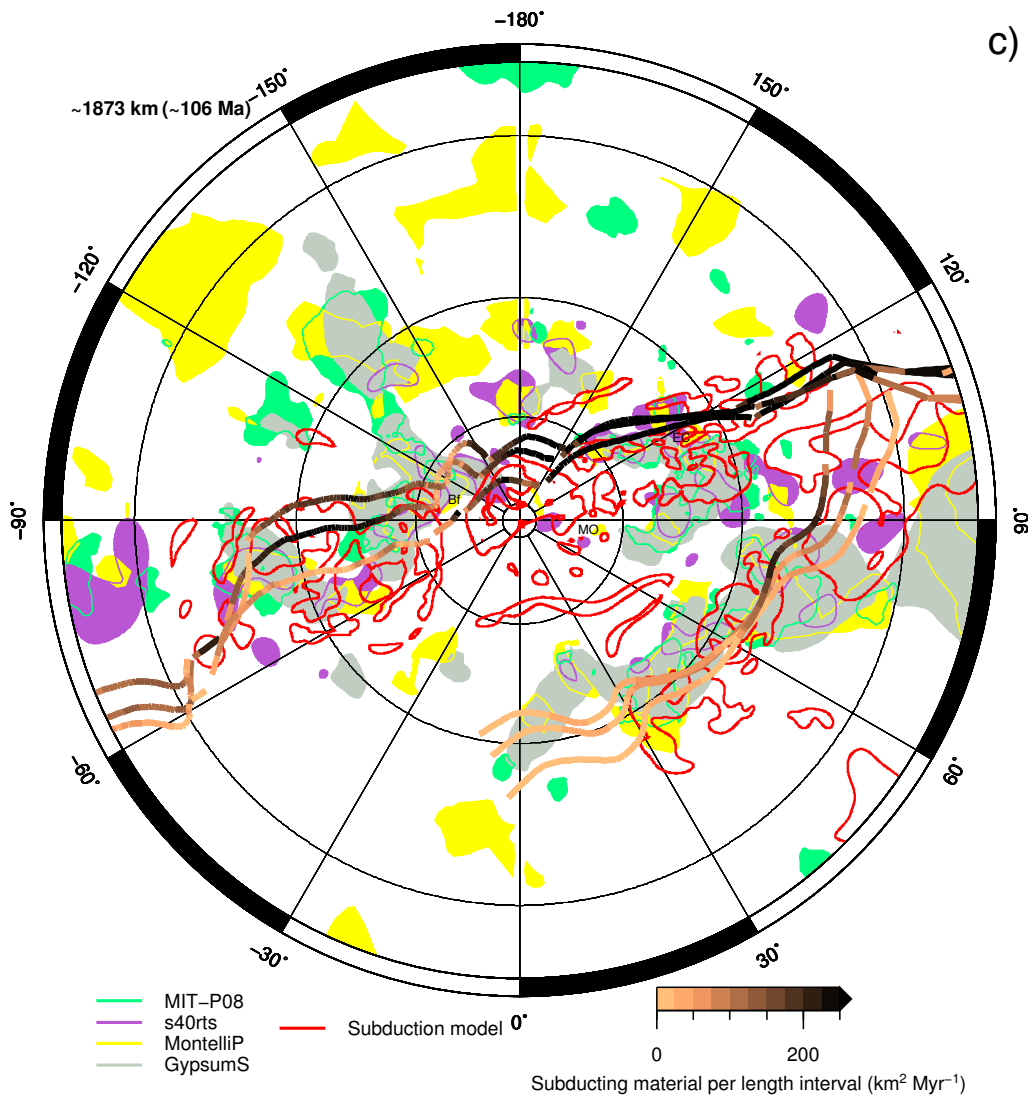

Figure S 1 cont.

Figure S 1 cont.

Figure S 1 cont.

Figure S 1: Horizontal depth slice comparing tomography models, Subduction reference frame kinematic information, and the Subduction reference frame model geodynamic output. The stereographic projection is centred on the North Pole, with gridlines every 30°. Depth in a) is 571 km for the geodynamic model and each tomography model slice corresponding to the closest depth available. Depth in b) is 1016 km for the geodynamic model and each tomography model slice corresponding to the closest depth available. Depth in c) is 1873 km for the geodynamic model and each tomography model slice corresponding to the closest depth available. Approximate slab location interpretations are represented by the text, Aeg (Aegean Tethys), Al (Aleutian), Bf (Beaufort), Ch (Chukchi), EC (East China), Far (Farallon), Hi (Himalayas), Kc (Kamchatka), Mc (Manchuria), Md (Maldives), Me (Mesopotamia), MO (Mongol-Okhotsk), Mg (Mongolian), and Sa (Sakhalin). The colors of each tomography model are shown in the legend, and represent the locations of statistically significant positive velocity perturbations. These values are +0.6% for GyPSum-S, +0.2% for MITP-08, +0.6% for s40rts, and +0.3% for Montelli-P. The -200 K temperature contour of the geodynamic model is overlain for comparison. The subducting material volume corresponds to kinematic reconstructions using the Subduction reference frame at a) 11 Ma, b) 48 Ma, 40 Ma, and 35 Ma, c) 134 Ma, 106 Ma, and 89 Ma. Here, the equivalent ages are derived from assuming a sinking rate of 52 mm/yr in the upper mantle, and 13±3 mm/yr in the lower mantle. Multiple times are used to provide an indication for the error in slab surface location in space and time.
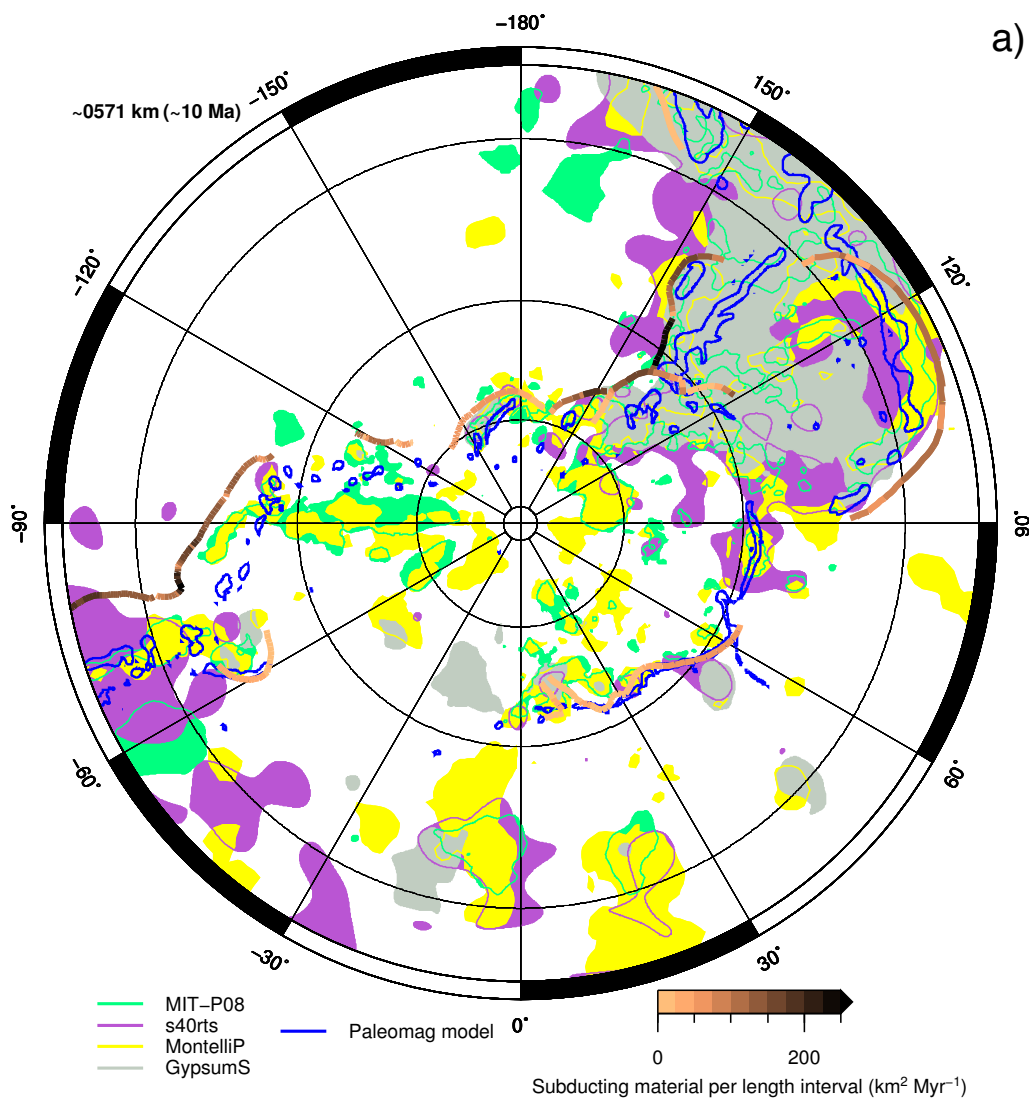
Figure S 2 cont.

b)

~1016 km (~40 Ma)

MIT−P08
s40rts
MontelliP
GypsumS

Paleomag model

Subducting material per length interval (km^2 Myr^{-1})
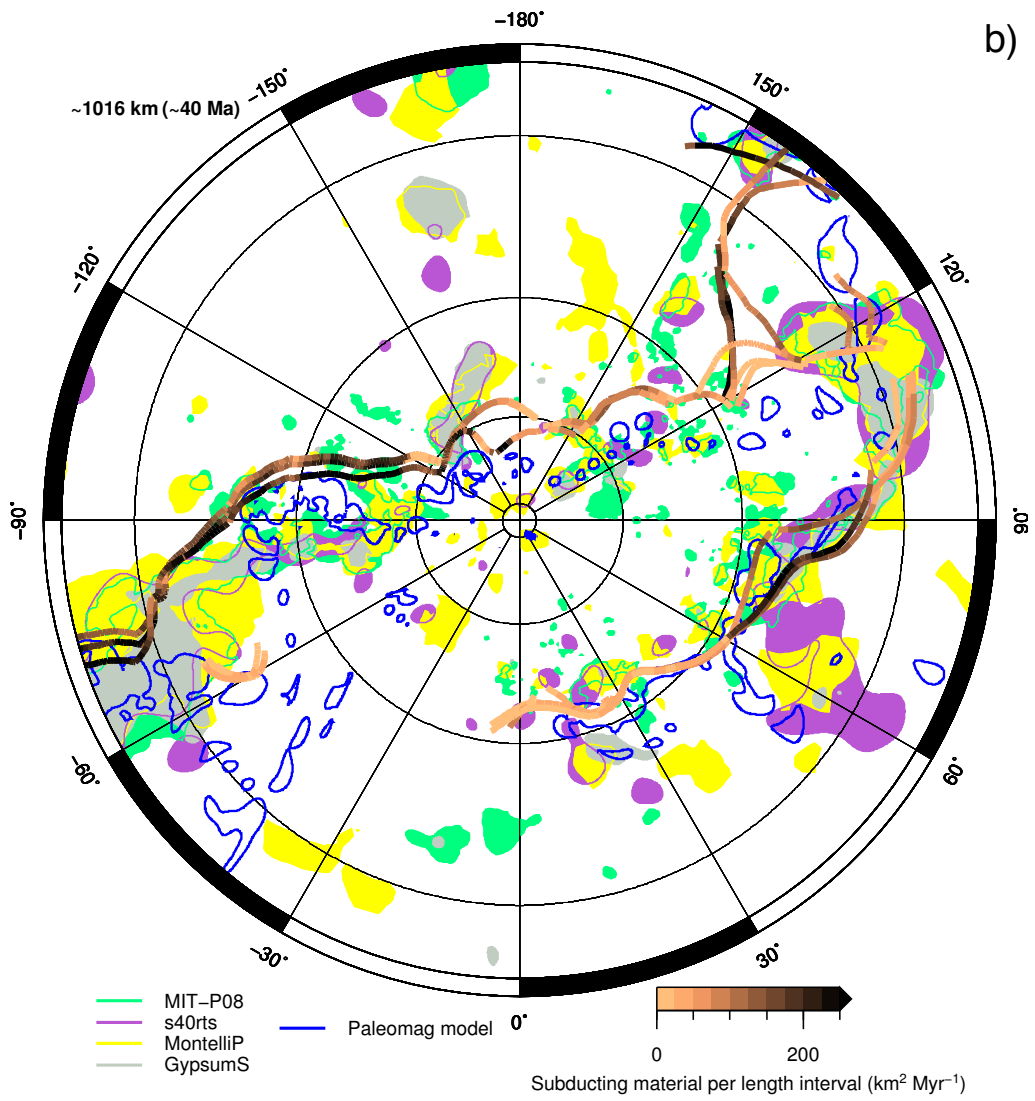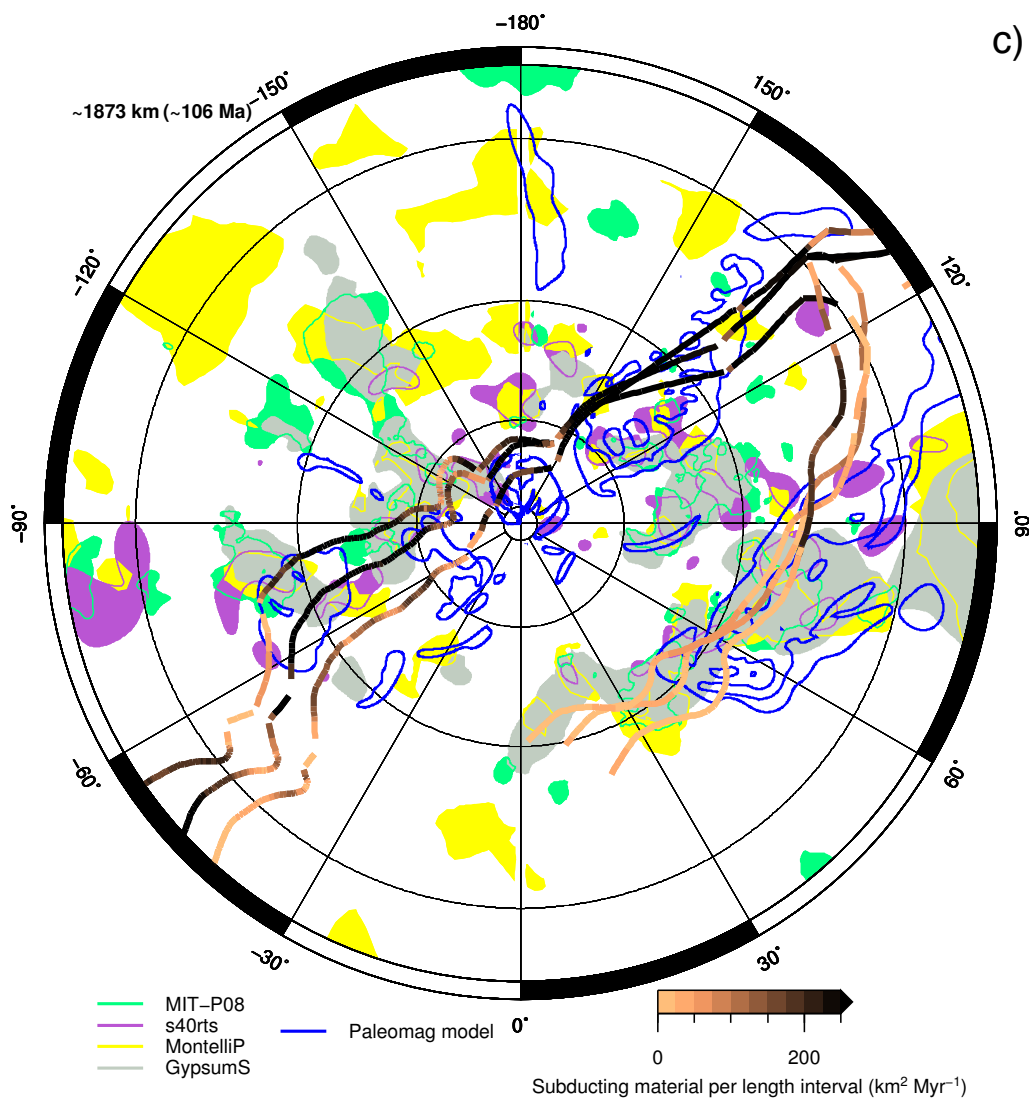
0   200

Figure S 2 cont.

Figure S 2: Same as Figure S1 but with the Hybrid Paleomagnetic reference frame and geodynamic model output.
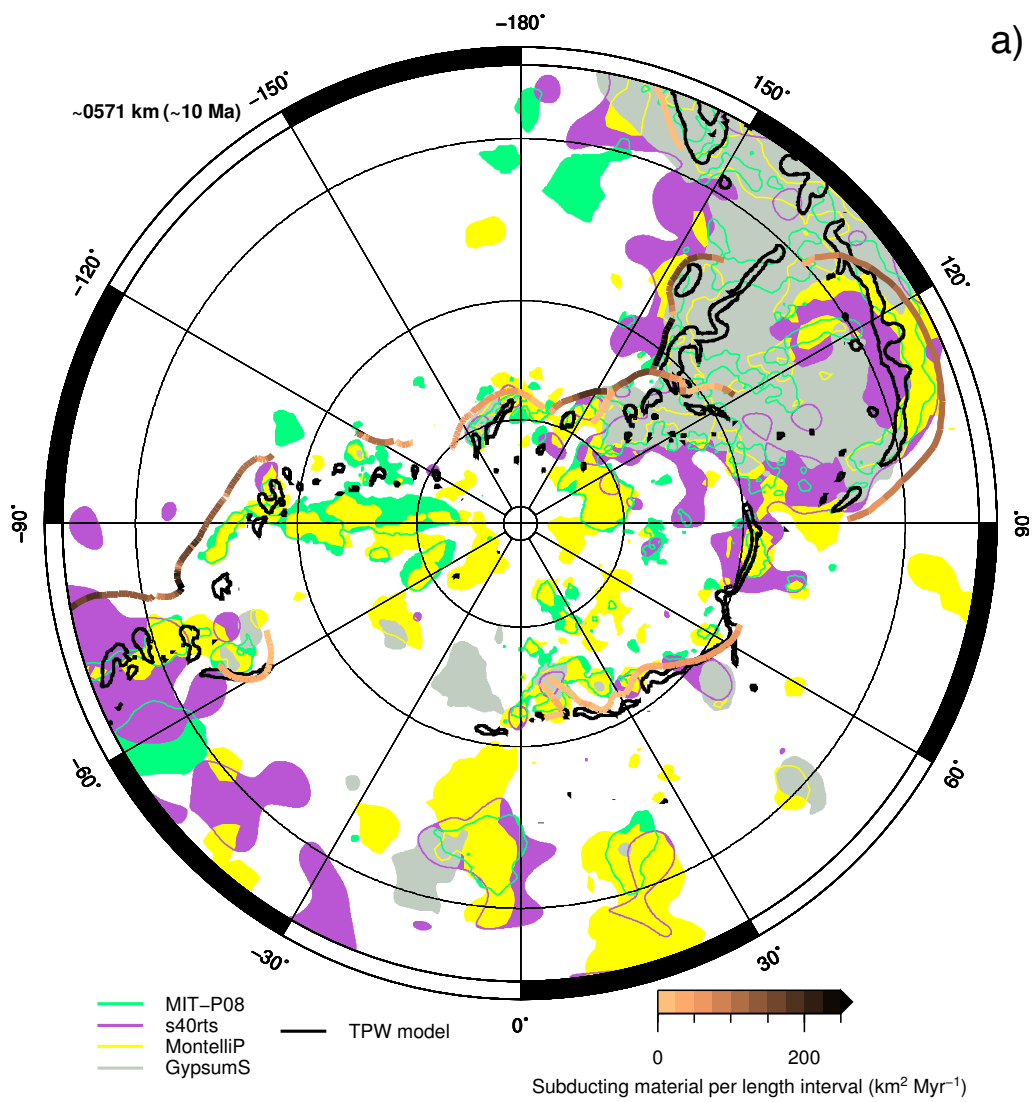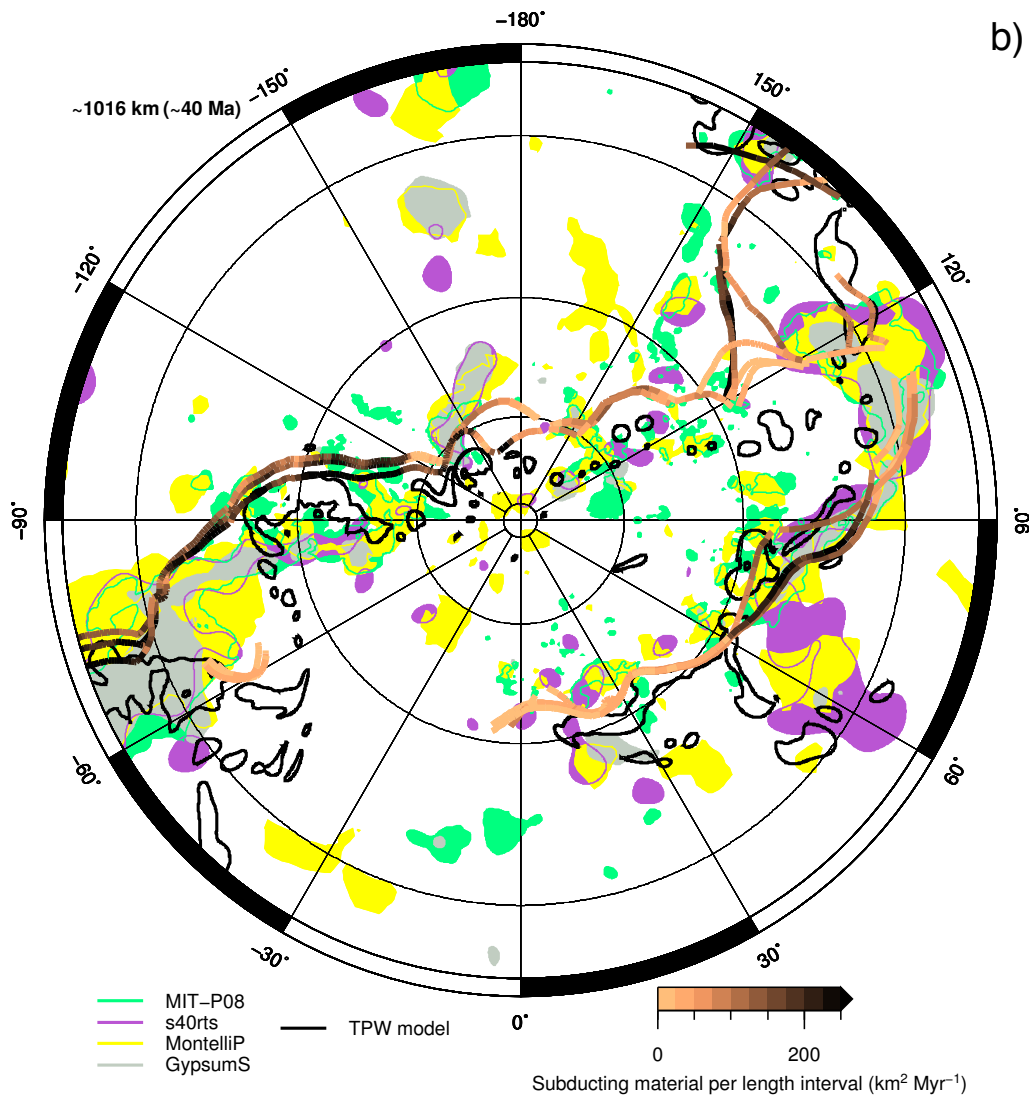
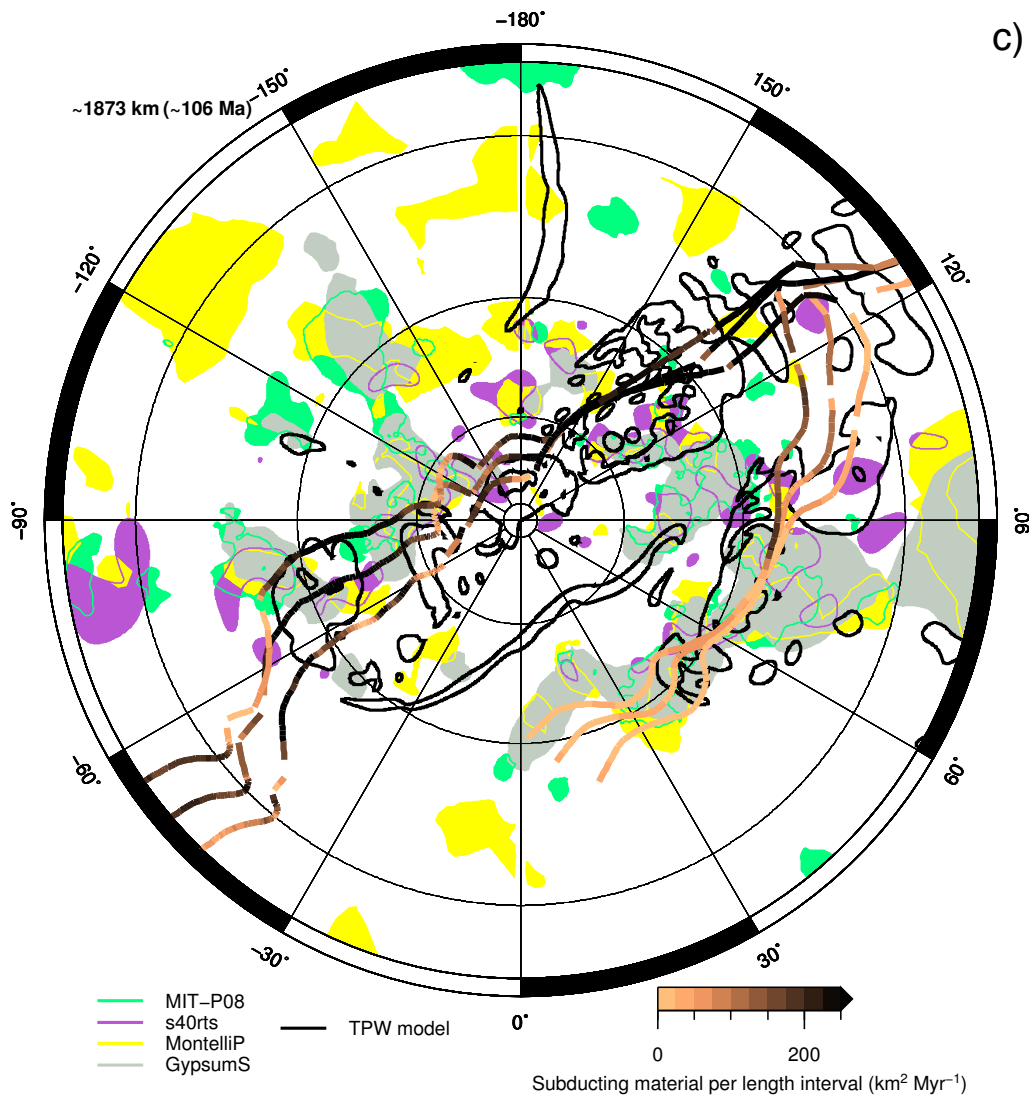Figure S 3 cont.

Figure S 3 cont.

Figure S 3: Same as Figure S1 but with the Hybrid TPW Paleomagnetic reference frame and geodynamic model output.
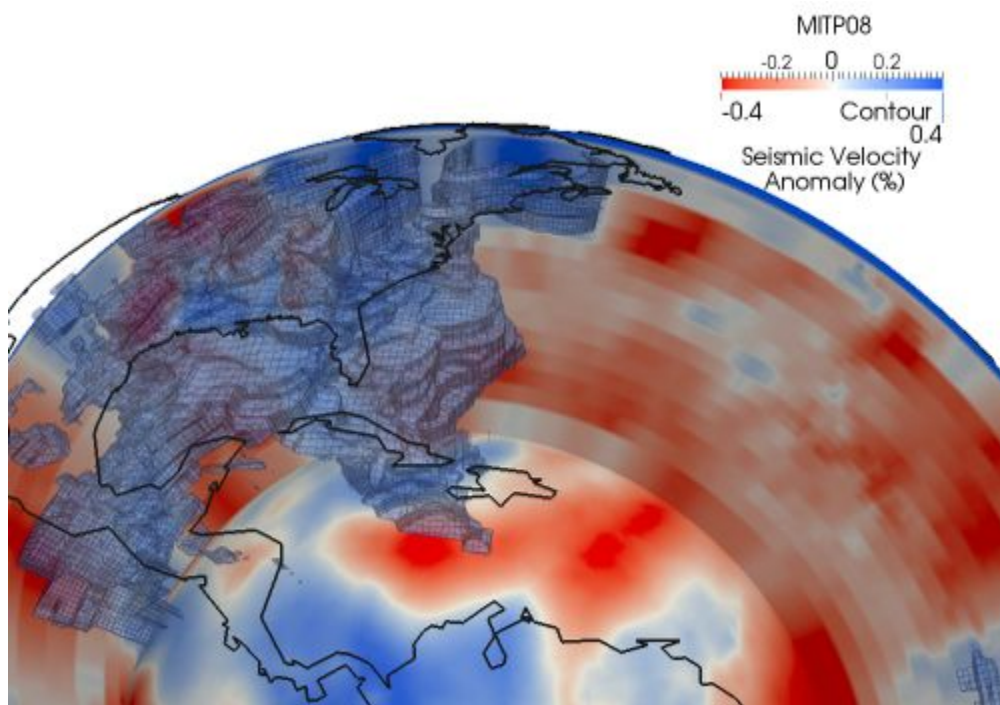
Figure S 4: Snapshot of 3D tomography model (MIT-P08). The image shows the Farallon slab extending from 25°N in the foreground terminating at a vertical cross-section at 60° N. The lowermost depth slice forms the base of the image reflecting the mantle structure at the CMB. The continents are overlain for context. Colors shown in the legend are the seismic velocity perturbation, blue is positive, fast, slab material, and red is negative, slow material. The image highlights the complex nature of assigning a particular depth for any particular slab. Similar results are found for all slabs discussed.
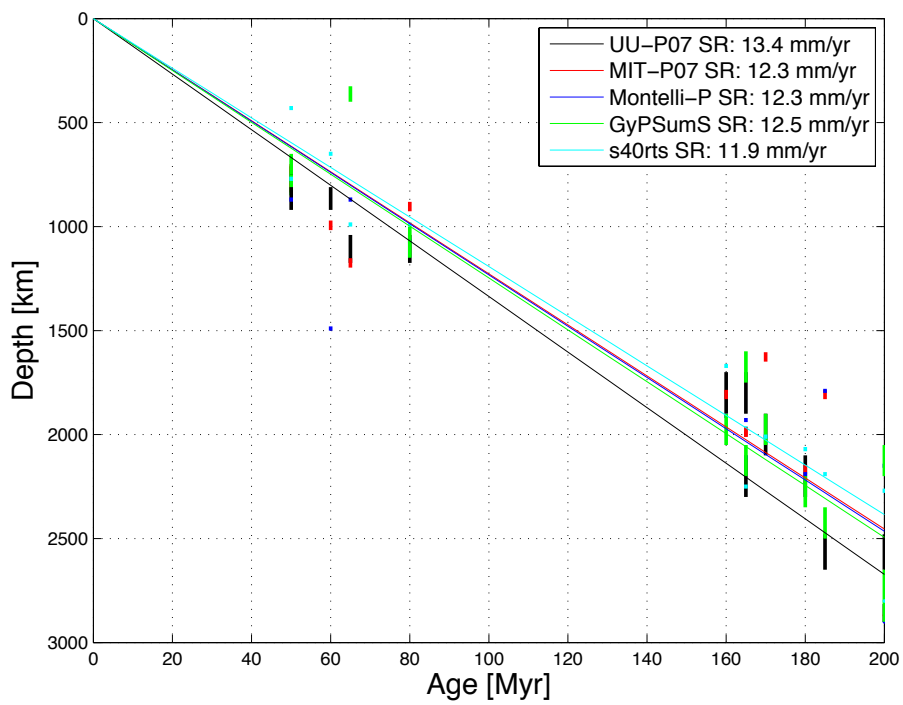
Figure S 5: Age-depth plot for each of the tomography models. Each model is colored as in the legend, and is accompanied by the corresponding sinking rate. The thick bars show the locations of the slab tops and bases (Table 2, 3, 4). The length of the bar corresponds to the maximum and minimum depth for each inferred point.
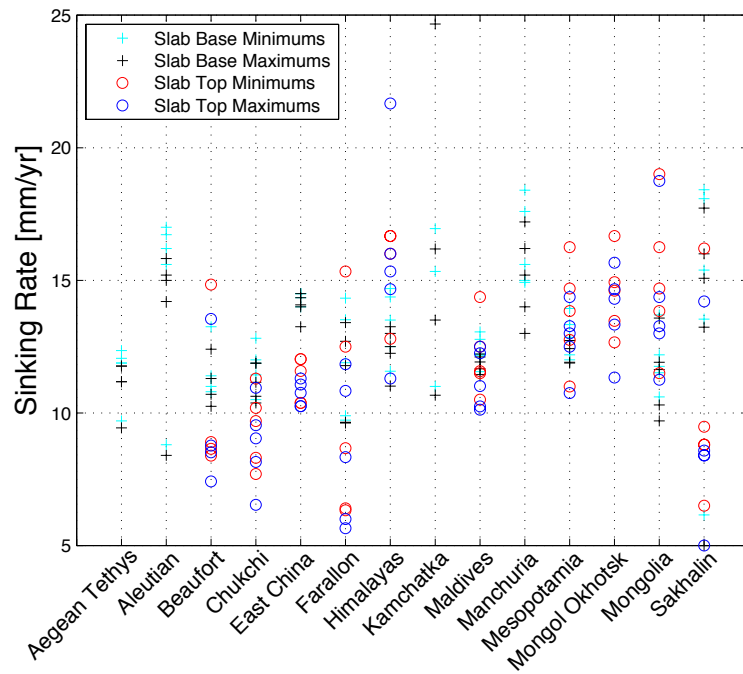
Figure S 6: Regional sinking rates for the slabs appearing in each tomography model used in this study (Table 2, 3, 4). Crosses correspond to slab bases and circles correspond to slab tops. Aqua and red are minimum values for each model, whilst black and blue are maximum values for each model.

References

Müller, R., Sdrolias, M., Gaina, C., Roest, W., 2008. Age, spreading rates, and spreading asymmetry of the world's ocean crust. Geochemistry, Geophysics, Geosystems 9, Q04006.

Schubert, G., Turcotte, D.L., Olson, P., 2001. Mantle Convection in the Earth and Planets. Cambridge University Press.

5 Discussion of subduction dynamics and its tectonic consequences

The energy source for plate tectonics is the release of the mantle's gravitational potential energy through convection, modulated by internal radiogenic heating and core cooling. Plate tectonic theory provides mechanisms and explanations for numerous types of large-scale topographic and geophysical features on Earth, such as mid-oceanic ridges, trenches, hotspot island chains and mountain belts. The theory is well established and its kinematic framework is generally accepted (Bercovici et al., 2000). However, considerable debate remains about the relative contributions of the forces driving plate tectonics and their tectonic implications (Conrad and Lithgow-Bertelloni, 2002; Lithgow-Bertelloni and Richards, 1998). Plate tectonics is the surface expression of mantle convection, and subducting slabs are the thermo-chemical downwelling of the convective process. Thus, understanding the subduction process and its kinematic consequences is essential for unravelling Earth's geological history.

Due to the non-linearity of physical parameters controlling subduction processes, conducting parameter sensitivity analyses is paramount to understanding these processes. The BEM-Earth software solves for buoyancy and mantle flow using boundary elements and allows for reproducible and realistic numerical models of subduction whilst self-consistently reproducing the kinematics of plate motions, including the vector magnitudes and directions (Chapter 2; Chapter 3; Appendix A; Morra et al., 2012). BEM-Earth simulations confirm that the kinematics of a plate affected by slab pull resulting from subduction at least partially controls the mantle flow channelled by nearby non-subducting plates. Various physical variables of non-subducting plates, the rheology, geometrical shape, and relative location to the subducting slab, all control the descent of slab

material in the mantle. Natural subduction zones produce different styles of slabs along the extent of the trench (Billen, 2008; Li et al., 2008), this is partially controlled by the inhomogeneity of the nearby non-subducting plates. However, the main driver of the subducting system is likely the subducting plate (Becker and Faccenna, 2009). Forces transmitted by the subducting slab to the overriding plate have tectonic consequences on the overriding plate itself (van Dinther et al., 2010), such as the shift from compressional to extensional settings as the viscosity and geometry of the overriding plate is changed. I find this is related to how much of the induced mantle flow energy acting on the plate is dissipated in deforming the plates.

Subduction is a primary driving force of plate motions and plate deformation. Cold, strong slabs effectively transmit stresses to subducting surface plates, exerting a direct slab pull force on these plates, drawing them rapidly toward subduction zones (Conrad and Lithgow-Bertelloni, 2004). Between the end of the Late Cretaceous to the early Cenozoic, the Pacific Plate underwent a significant kinematic shift, resulting from changes in its primary driving forces. In Chapter 3 I find induced mantle flows that actuate tractions on non-subducting plates control the motion of the Pacific at the end of the Late Cretaceous. Following the subduction of the Pacific-Izanagi ridge, in the models from 52 Ma onwards, the Pacific Plate is then primarily controlled directly by slab-pull in the northwest. The absolute motions of the Pacific derived from subduction driven forces correspond well with plate motions derived from plate reconstructions (Seton et al., 2012; Chandler et al., 2012), when model assumptions and simplifications are taken into account. Absolute reference frames strongly dependent on Pacific hotspots do not reproduce Pacific plate motions driven by buoyancy (Doubrovine et al., 2012; Wessel and Kroenke, 2008).

Subducting slabs coupled mechanically to the rest of the plate impart stress on the lithosphere and induce deformation in the plate (Chapter 2 and 3). The present state of stresses within a plate and its recent evolution is important for understanding geological phenomena as diverse as the distribution of earthquakes, mountain building events, volcanism, sedimentary basin formation, and the distribution of fluid reservoirs. Globally, the tectonic stress field and its variations are intimately linked to the driving mechanism of plate tectonics (Lithgow-Bertelloni and Guynn, 2004). Forces responsible for plate motion are edge forces, including slab pull and ridge push, driving rigid plates over a weaker asthenosphere that acts to modulate plate motion. However, oceanic

lithosphere penetrating the lower mantle also significantly contributes to slab pull and slab suction. A consequence of these forces result in motion and deformation of the plate. Indeed, Finite Element analysis of the North American plate showed (Humphreys and Coblentz, 2007) that the boundary loads are most important for inter-plate stress, followed by internal stresses, then basal loads acting from within the asthenosphere beneath the plate. Knowledge of stress magnitude on plate boundaries bears directly on fault stress levels, faulting mechanics, and the distribution of stress through the crust and mantle lithosphere. My analysis in Chapter 3 of stresses deforming the Pacific, due to the buoyancy driven forces acting on the plate, reveals that regions of intraplate deformation occur directly adjacent to the most voluminous subducting slabs. Certain types of volcanism can be considered as a proxy for a highly-stressed deforming lithosphere (Clouard and Gerbault, 2008). I find many occurrences of intraplate volcanism, which results in volcanic chains lacking age-progression (i.e. not related to mantle plumes), across the Pacific correlates with modeled lithospheric deformation. The origin of intraplate volcanism without age progression and far away from plate boundaries remains poorly understood (Koppers, 2011; Lee and Grand, 2012). Intraplate volcanism can be viewed as being due to hotspots or hot regions within tectonic plates, which may be due to a range of processes including mantle plumes, small-scale convection, or lithospheric cracking within plates (Bianco et al., 2011; Ballmer et al., 2009; Sandwell and Fialko, 2004). In an effort to isolate mechanisms of anomalous Pacific intra-plate volcanism, I analyse changes in plate motion around the Pacific ocean basin by considering slab-pull and mantle drag/suction forces, and compare the results with absolute plate motions derived from plate reconstructions and the occurrence of intraplate volcanics (e.g Clouard and Bonneville, 2005). Tectonic consequences reveal the seamount chains of Hawaii, Louisville, and Tokelau are subject to lithospheric deformation occurring between 72 and 42 Ma. Plate-scale extensional stresses between 72 and 52 Ma correlate with the location and timing of formation of the Gilbert volcanic chain, suggesting an origin due to lithospheric extension at this time. The Musicians Ridge, which is likely composed of mantle plume products, spatially correlate with modeled lithospheric stress and is a likely candidate for late-stage volcanism between 62 and 42 Ma. The 3D mantle flow models suggest stress-induced deformation in the Pacific during the Late Cretaceous and early Cenozoic is at least partially controlled by plate-scale kinematics driven by subduction forces.

The dynamics of a sinking slab are dictated by the interplay of complicated

phenomena governed by an incredibly large array of parameters. Mantle flow models, incorporating 3D numerical simulations, are necessary to study many aspects of subduction dynamics, for instance, Schellart et al. (2007) found slab width controls, to first-order, curvature of subduction zones and the tendency to retreat back with time. A follow up investigation (Schellart et al., 2010) determined plate and trench velocities scale with the width of the plate. Further, Stegman et al. (2010) concluded that the flexural strength and the buoyancy determine the subduction style distinguished by a characteristic slab morphology, and control several subduction characteristics including the partitioning between slab rollback and trench advance, the trench curvature, and the slab's radius of curvature. Slab induced mantle flow is a prominent control on the topographic signal in the vicinity of subduction boundaries (Husson, 2006). This results in a curved shaped characteristic of retreating trenches and a depressed topography above the slab. When a subducting plate interacts with a thermal or chemical discontinuity in the upper or lower mantle boundary they deform (Billen, 2008). A general understanding of subduction controls seems to be understood. However, specific controlling parameters must continue to be investigated to quantify their direct influences on subduction dynamics to determine what effect these parameters may have on surface plate motions and resulting tectonic events.

Plate motions in absolute reference frames are essential for linking plate motions and the history of subduction to mantle dynamics and tectonic events. Additional constraints on absolute plate motion can be derived by considering the inherent connection between plate boundaries and the history of subduction reflected by tomographically interpreted subducted slabs in the mantle. Absolute plate motions, which anchor relative plate motions to the Earth's spin axis, are still controversial as different approaches advocate alternative absolute plate positions through time. Geodynamic mantle convection simulations from the Terra code (Chapter 4) reveal a correspondence with present day mantle structure; its accuracy partially depending on plate reconstruction input. Various methods for reconstructing past plate motions exist (e.g. O'Neill et al., 2005; Doubrovine et al., 2012; Torsvik et al., 2008; Seton et al., 2012), and the apparent misfits with plate motion models implicates the forward geodynamic models in one way or another. I find in Chapter 4 that the locations of paleo-plate boundaries, and subduction zones in particular, along with the relative velocities between the plates is congruent with the accuracy of the geodynamically modeled mantle structure. Model results indicate that while subduction zone location is important in determining modeled mantle structure, plate velocity and hence slab input

rates into the mantle are critical.

Identifying the present-day depth of any particular slab, resulting from now-extinct or ancient subduction, is not straightforward, as the evolution of the slab since subduction initiation is complicated, thus regional variations in slab sinking rates must be taken into account to avoid spurious global age-depth relationships. Utilising regional corrections and validation with iterative geodynamic modeling I help to provide constraints on slab dynamics and the robustness of reference frames in Chapter 4. I find the combination of alternative plate kinematic models, geological observations, mantle tomography, and geodynamic models reveal a globally averaged mantle sinking rate of $13 \pm 3 \, \mathrm{mm/yr}$. Also, my results from geodynamic modeling suggest a sinking rate of $\sim$15–20 mm/yr in the lower mantle. Both the results, from the geological data and modeling, indicate that a viscosity contrast of two orders of magnitude between the upper and lower mantle is reasonable to reproduce natural subduction.

The unfolding of a dynamically evolving sinking slab is a complex process, with several modes of subduction identified (Ribe et al., 2007; Billen, 2008; Sigloch and Mihalynuk, 2013; Li and Ribe, 2012). Individual regional analyses are necessary for complete understanding of any particular slab. However, results of individual regions should be able to self-consistently reproduce global-scale tectonic events. Similarly, global-scale tectonics should self-consistently reproduce regional dynamics and kinematics (Stadler et al., 2010). Modeled regional analyses may not have enough information to properly reproduce the global mantle evolution if neighbouring regions are absent from models (Chapter 2). This multi-scale problem requires multiple tools and observations for effective exploration. BEM-Earth is an efficient Stokes flow solver, useful for investigating real-world mantle dynamics problems. The code provides higher resolution to better reveal natural mantle behaviours, whilst being set-up such that parameters may be explored in a controlled and systematic way. A 10 Myr simulation may be run on 128 processors in around 6 hours. The model evolves dynamically, primarily driven by the amount of material available for slab-pull (and induced suction) forces prescribed in the initial conditions. This dynamic treatment allows for effective investigation of the forces driving the subduction and the resulting tectonics. Concurrently, Terra simulates global mantle convection whilst reproducing regional mantle structure. A typical Terra model run takes around 7 days on 128 processors. Any geodynamic code requires some knowledge of the initial starting conditions for mantle flow, however the way this is implemented and the

boundary conditions of the Terra and BEM-Earth codes differs markedly. Terra uses changing surface boundary conditions, assimilated through plate kinematic models, to sustain model runs for hundreds of millions of years. This may yield advective thickening of slabs at trenches and would require temperature assimilation to overcome this shortcoming (Flament et al., 2013). The lack of enforced boundary conditions in BEM-Earth favours the investigation of the dynamic problems discussed here. However, a significant limitation of BEM-Earth is the simplified viscosity structure of the mantle, restricting the problems that can be investigated to the shallow-mantle plate dynamics considered here. More complex mantle viscosities have been implemented in BEM-Earth elsewhere (Morra et al., 2010, 2012) to investigate longer time-scale mantle interactions. Multi layered viscosity structures can be implemented in Terra simulations, reflecting simplified mantle conditions, the long-term mantle structure can thus be investigated. Terra, as used here, still lacks more realistic radial viscosity profiles which artificially increases the coupling between the surface plates and the underlying mantle. Both Terra and BEM-Earth geodynamic simulations can be compared with independent geophysical data to help understand subduction dynamics and its tectonic consequences.

6 Conclusions and implications

Subduction is an integral component of Earth's tectonics. Subducting slabs provide a link between mantle convection and surface plate motions. The work presented in this thesis utilises the regional configuration of subduction zones in determining multi-scale dynamic and tectonic consequences. Numerical models combined with geophysical observations provide a fundamental method to study these processes at different scales. Using these methods I find that dynamics of subduction are strongly dependent on the geometry and rheology of the subducting slab and also on the non-subducting plates adjacent to the subduction zone. The dynamics result from the induced mantle flow driven by the evolution of plate motion and boundary configurations along subduction zones. Numerical models not accounting for overriding plate induced slab suction overestimate trench retreat by up to 65% in a 20 Myr model run. Overriding plates with a larger effective viscosity are associated with faster subducting slabs, analogue to oceanic plates subducting faster beneath more rigid continental lithosphere. Subduction dynamics are dominated by poloidal mantle flows, which couple the down-going and overriding plates. Trench-orthogonal length variations in overriding plates induce flows at least $\sim 2\times$ stronger than trench-parallel width variations. Furthermore, deformation in the overriding plate is related to its length and width, with narrower and longer plates extending more than wider and shorter plates. Large tectonic plates are known to be susceptible to internal deformation, leading to a range of phenomena including intraplate volcanism. Geodynamic models from this thesis suggest subducting plate dynamics during the early Cenozoic, resulting from changes in subduction zone topology, caused intraplate deformation to trigger volcanism along several linear Pacific seafloor structures. Extensional deformation, overprinting oceanic lithosphere weakened by the Manahiki-Chizca ridge and corresponding fracture zones, likely led to

94

volcanic activation precipitating the Gilbert seamount chain around 62 Ma. Localised extension between 72 and 42 Ma may have reactivated volcanism along the Musicians Volcanic Ridges, however sampling is required to confirm this. The poorly understood space and time dependence of intraplate deformation and its relationship with changing plate boundary configurations, subducting slab geometries and absolute plate motion is linked. My models demonstrate that early Cenozoic changes in Pacific plate driving forces only cause relatively minor changes in Pacific absolute plate motions, and cannot be responsible for the Hawaii-Emperor Bend (HEB), confirming previous interpretations that the 47 Ma HEB does not reflect an absolute plate motion event. Reconstructing the surface motions tied to deep subducted anomalies is paramount for unravelling subduction history and understanding slab dynamics. My geodynamic model results indicate that subduction zone location, based on different absolute reference frames, and relative plate motions, are important for correctly reproducing modeled mantle structure critical for accurate representation of subducted slabs. Seismic tomography models provide a present day snapshot of mantle heterogeneity, implicating locations of ancient subduction. In this thesis I have evaluated slab sinking rates by combining alternative plate kinematic models, geological observations, mantle tomography, and geodynamic models. My results converge on a globally averaged mantle sinking rate of 13 ± 3 mm/yr, slightly slower than 15–20 mm/yr predicted by geodynamic models. The complicated evolution of a subducting slab and the inconsistencies between tomography models make deciphering the depth (and lateral location) of any particular slab difficult. Iterative modeling and regional analysis of a specific slab must be performed to accurately correlate subducted material with surface geology and thus determine age-depth relationships. These results have implications for coupling regional subduction models to global-scale analyses, linking geological observations with deep seismic tomography anomalies, and subsequently producing next-generation absolute reference frames. In future work, fully dynamic subduction models may be used for constraining deep-time plate motion reconstructions, which will be verified with forward whole-mantle convection codes and present day observations.

Bibliography

Allmendinger, R., Jordan, T., Kay, S., Isacks, B., 1997. The evolution of the altiplano-puna plateau of the central andes. Annual Review of Earth and Planetary Sciences 25, 139–174.

Ballmer, M., van Hunen, J., Ito, G., Bianco, T., Tackley, P., 2009. Intraplate volcanism with complex age-distance patterns: A case for small-scale sub-lithospheric convection. Geochemistry, Geophysics, Geosystems 10, Q06015. doi:`10.1029/2009GC002386`.

Baumgardner, J.R., 1983. A Three-Dimensional Finite Element Model for Mantle Convection. Ph.D. thesis. University of California Los Angeles.

Becker, T., Faccenna, C., 2009. A review of the role of subduction dynamics for regional and global plate motions, in: Lallemand, S., Funiciello, F. (Eds.), Subduction Zone Geodynamics, Springer, Berlin. pp. 3–34. doi:`10.1007/978-3-540-87974-9\_1`.

Bercovici, D., 2003. The generation of plate tectonics from mantle convection. Earth and Planetary Science Letters 205, 107–121. doi:`0012-821X/02/$`.

Bercovici, D., Ricard, Y., Richards, M.A., 2000. The Relation Between Mantle Dynamics and Plate Tectonics: A Primer. American Geophysical Union. pp. 5–46. doi:`10.1029/GM121p0005`.

Bianco, T.A., Ito, G., van Hunen, J., Ballmer, M.D., Mahoney, J.J., 2011. Geochemical variations at intraplate hot spots caused by variable melting of a veined mantle plume. Geochemistry, Geophysics, Geosystems 12, Q0AC13. doi:`10.1029/2011GC003658`.

Billen, M., 2008. Modeling the dynamics of subducting slabs. Annual Review of Earth and Planetary Sciences 36, 325–56. doi:`10.1146/annurev.earth.36.031207.124129`.

Boyden, J., Müller, R., Gurnis, M., Torsvik, T., Clark, J., Turner, M., Ivey-Law, H., Watson, R., Cannon, J., 2011. Next-generation plate-tectonic reconstructions using GPlates, in: G.R., K., Baru, C. (Eds.), Geoinformatics: Cyberinfrastructure for the Solid Earth Sciences. Cambridge University Press. chapter 7, pp. 95–116. doi:`10.1017/CBO9780511976308.008`.

Bunge, H., Baumgardner, J.R., 1995. Mantle convection modeling on parallel virtual machines. Computers in Physics 9, 207–215. doi:`10.1063/1.168525`.

Bunge, H.P., 1997. Global mantle convection models. Ph.D. thesis. University of California Berkeley.

Bunge, H.P., Hagelberg, C.R., Travis, B.J., 2003. Mantle circulation models with variational data assimilation: inferring past mantle flow and structure from plate motion histories and seismic tomography. Geophysical Journal International 152, 280–301. doi:`10.1046/j.1365-246X.2003.01823.x`.

Capitanio, F.A., Faccenna, C., Zlotnik, S., Stegman, D.R., 2011. Subduction dynamics and the origin of andean orogeny and the bolivian orocline. Nature 480, 83–86. doi:`10.1038/nature10596`.

Carlson, R., Hilde, T., Uyeda, S., 1983. The driving mechanism of plate tectonics: relation to age of the lithosphere at trenches. Geophysical Research Letters 10, 297–300. doi:`10.1029/GL010i004p00297`.

Chandler, M.T., Wessel, P., Taylor, B., Seton, M., Kim, S.S., Hyeong, K., 2012. Reconstructing Ontong Java Nui: Implications for Pacific absolute plate motion, hotspot drift and true polar wander. Earth and Planetary Science Letters 331-332, 140–151. doi:`10.1016/j.epsl.2012.03.017`.

Clarke, D., Quevedo, L., Heine, C., Flament, N., 2013. Post Jurassic Dynamic Topography. Master's thesis. The University of Sydney.

Clouard, V., Bonneville, A., 2005. Ages of seamounts, islands, and plateaus on the Pacific plate. Geological Society of America 388, 71–90. doi:`10.1130/0-8137-2388-4.71`.

Clouard, V., Gerbault, M., 2008. Break-up spots: Could the Pacific open as a consequence of plate kinematics? Earth and Planetary Science Letters 265, 195–208. doi:`10.1016/j.epsl.2007.10.013`.

Conrad, C., Hager, B., 1999. The thermal evolution of an earth with strong subduction zones. Geophysical Research Letters 26, 3041–3044. doi:`10.1029/1999GL005397`.

Conrad, C., Lithgow-Bertelloni, C., 2002. How mantle slabs drive plate tectonics. Science 298, 207. doi:`10.1126/science.1074161`.

Conrad, C., Lithgow-Bertelloni, C., 2004. The temporal evolution of plate driving forces: Importance of "slab suction"versus "slab pull"during the Cenozoic. Journal of Geophysical Research 109, B10407. doi:`10.1029/2004JB002991`.

Davies, D.R., 2008. Applying Multi-Resolution Numerical Methods to Geodynamics. Ph.D. thesis. Cardiff University, School of Earth, Ocean and Planetary Sciences.

Davies, G.F., 1980. Thermal histories of convective earth models and constraints on radiogenic heat production in the earth. Journal of Geophysical Research: Solid Earth 85, 2517–2530. doi:`10.1029/JB085iB05p02517`.

van Dinther, Y., Morra, G., Funiciello, F., Faccenna, C., 2010. Role of the overriding plate in the subduction process: Insights from numerical models. Tectonophysics 484, 74–86. doi:`10.1016/j.tecto.2009.08.038`.

Doubrovine, P., Steinberger, B., Torsvik, T., 2012. Absolute plate motions in a reference frame defined by moving hot spots in the Pacific, Atlantic, and Indian oceans. Journal of Geophysical Research 117, B09101. doi:`10.1029/2011JB009072`.

Flament, N., Gurnis, M., Müller, R.D., 2013. A review of observations and models of dynamic topography. Lithosphere doi:`10.1130/L245.1`.

Forsyth, D., Uyeda, S., 1975. On the relative importance of the driving forces of plate motion*. Geophysical Journal of the Royal Astronomical Society 43, 163–200. doi:`10.1111/j.1365-246X.1975.tb00631.x`.

Forsyth, D.W., 1977. The evolution of the upper mantle beneath mid-ocean ridges. Tectonophysics 38, 89–118. doi:`10.1016/0040-1951(77)90202-5`.

Gerya, T., 2011. Future directions in subduction modeling. Journal of Geodynamics 52, 344–378. doi:`10.1016/j.jog.2011.06.005`.

Grzhibovskis, R., Liu, Y., Morra, G., Rjasanow, S., Weggler, L., 2011. Large scale boundary element methods, in: Large Scale Boundary Element Methods. Faculty of Engineering Univeristy of Brescia, pp. 1–184.

Hager, B.H., O'Connell, R.J., 1979. Kinematic models of large-scale flow in the earth's mantle. Journal of Geophysical Research: Solid Earth 84, 1031–1048. doi:`10.1029/JB084iB03p01031`.

Hayes, G.P., Wald, D.J., Johnson, R.L., 2012. Slab1.0: A three-dimensional model of global subduction zone geometries. Journal of Geophysical Research: Solid Earth 117, B01302. doi:`10.1029/2011JB008524`.

Humphreys, E., Coblentz, D., 2007. North American dynamics and western US tectonics. Reviews of Geophysics 45, 8755–1209.

Husson, L., 2006. Dynamic topography above retreating subduction zones. Geology 34, 741. doi:`10.1130/G22436.1`.

Kim, S., Wessel, P., 2011. New global seamount census from altimetry-derived gravity data. Geophysical Journal International 186, 615–631. doi:`10.1111/j.1365-246X.2011.05076.x`.

Koppers, A.A.P., 2011. Mantle plumes persevere. Nature Geoscience 4, 816–817. doi:`10.1038/ngeo1334`.

Lee, C.T.A., Grand, S.P., 2012. Intraplate volcanism. Nature 482, 314–315. doi:`10.1038/482314a`.

Li, C., van der Hilst, R.D., Engdahl, E.R., Burdick, S., 2008. A new global model for P wave speed variations in Earth's mantle. Geochemistry, Geophysics, Geosystems 9, 5018–+. doi:`10.1029/2007GC001806`.

Li, Z.H., Ribe, N.M., 2012. Dynamics of free subduction from 3-d boundary element modeling. Journal of Geophysical Research 117. doi:`10.1029/2012JB009165,`.

Lithgow-Bertelloni, C., Guynn, J., 2004. Origin of the lithospheric stress field. Journal of Geophysical Research 109, B01408. doi:`10.1029/2003JB002467`.

Lithgow-Bertelloni, C., Richards, M., 1998. The dynamics of Cenozoic and Mesozoic plate motions. Reviews of Geophysics 36, 27–78. doi:`10.1029/97RG02282`.

Matthews, K., Müller, R., Wessel, P., Whittaker, J., 2011. The tectonic fabric of the ocean basins. Journal of Geophysical Research 116, B12109. doi:`10.1029/2011JB008413`.

Max Planck Institute for Chemistry, Mainz, . Georoc. `http://georoc.mpch-mainz.gwdg.de/`. Accessed: 11 August 2013.

Molnar, P., Atwater, T., 1978. Interarc spreading and cordilleran tectonics as alternates related to the age of subducted oceanic lithosphere. Earth and Planetary Science Letters 41, 330–340. doi:`10.1016/0012-821X(78)90187-5`.

Montelli, R., Nolet, G., Masters, G., Dahlen, F., Hung, S.H., 2004. Global p and pp traveltime tomography: rays versus waves. Geophysical Journal International 158, 637–654. doi:`10.1111/j.1365-246X.2004.02346.x`.

Moresi, L., Gurnis, M., 1996. Constraints on the lateral strength of slabs from three-dimensional dynamic flow models. Earth and Planetary Science Letters 138, 15 – 28. doi:`10.1016/0012-821X(95)00221-W`.

Morra, G., Chatelain, P., Tackley, P., Koumoutsakos, P., 2007. Large scale three-dimensional boundary element simulation of subduction, in: Shi, Y., Albada, G., Dongarra, J., Sloot, P. (Eds.), Computational Science – ICCS 2007. Springer Berlin Heidelberg. volume 4489 of *Lecture Notes in Computer Science*, pp. 1122–1129. doi:`10.1007/978-3-540-72588-6\_178`.

Morra, G., Chatelain, P., Tackley, P., Koumoutsakos, P., 2009. Earth curvature effects on subduction morphology: Modeling subduction in a spherical setting. Acta Geotechnica 4, 95–105. doi:`10.1007/s11440-008-0060-5`.

Morra, G., Quevedo, L., Muller, R.D., 2012. Spherical dynamic models of top-down tectonics. Geochemistry, Geophysics, Geosystems 13, 1–66. doi:`10.1029/2011GC003843`.

Morra, G., Yuen, D., Boschi, L., Chatelain, P., Koumoutsakos, P., Tackley, P., 2010. The fate of the slabs interacting with a density/viscosity hill in the mid-mantle. Physics of the Earth and Planetary Interiors 180, 271–282. doi:`10.1016/j.pepi.2010.04.001`.

Müller, R., Dutkiewicz, A., Seton, M., Gaina, C., 2013. Seawater chemistry driven by supercontinent assembly, breakup, and dispersal. Geology 41, 907–910. doi:`10.1130/G34405.1`.

O'Neill, C., Müller, D., Steinberger, B., 2005. On the uncertainties in hot spot reconstructions and the significance of moving hot spot reference frames. Geochemistry, Geophysics, Geosystems 6, Q04003. doi:`10.1029/2004GC000784`.

Pozrikidis, C., 1992. Boundary integral and singularity methods for linearized viscous flow. Cambridge University Press.

Quevedo, L., Morra, G., Müller, R.D., 2010. Parallel fast multipole boundary element method for crustal dynamics. IOP Conference Series: Materials Science and Engineering 10, 012012. doi:`doi:10.1088/1757-899X/10/1/012012`.

Ribe, N.M., Stutzmann, E., Ren, T., van der Hilst, R., 2007. Buckling instabilites of subducted lithosphere beneath the transition zone. Earth and Planetary Science Letters 254, 173–179. doi:`10.1016/j.epsl.2006.11.028`.

Ricard, Y., 2007. Physics of mantle convection, in: Bercovici, D. (Ed.), Treatise on Geophysics. Elsevier. volume 7 Mantle Dynamics, pp. 31–87.

Ritsema, J., Deuss, A., van Heijst, H.J., Woodhouse, J.H., 2010. S40rts: a degree-40 shear-velocity model for the mantle from new rayleigh wave dispersion, teleseismic traveltime and normal-mode splitting function measurements. Geophysical Journal International doi:`10.1111/j.1365-246X.2010.04884.x`.

Sandwell, D., Fialko, Y., 2004. Warping and cracking of the Pacific plate Warping and cracking of the Pacific plate by thermal contraction. Journal of Geophysical Research 109, B10411. doi:`10.1029/2004JB003091`.

Sandwell, D., Smith, W.H.F., 2009. Global marine gravity from retracked Geosat and ERS-1 altimetry: Ridge segmentation versus spreading rate. Journal of Geophysical Research 114, B01411. doi:`10.1029/2008JB006008`.

Schellart, W., Freeman, J., Stegman, D., Moresi, L., May, D., 2007. Evolution and diversity of subduction zones controlled by slab width. Nature 446, 308–311. doi:`10.1038/nature05615`.

Schellart, W., Moresi, L., 2013. A new driving mechanism for backarc extension and backarc shortening through slab sinking induced toroidal and poloidal

mantle flow: Results from dynamic subduction models with an overriding plate. Journal of Geophysical Research doi:`10.1002/jgrb.50173`.

Schellart, W., Stegman, D., Farrington, R., Freeman, J., Moresi, L., 2010. Cenozoic tectonics of western north america controlled by evolving width of farallon slab. Science 329, 316–319. doi:`10.1126/science.1190366`.

Sdrolias, M., Müller, R., 2006. Controls on back-arc basin formation. Geochemistry, Geophysics, Geosystems 7, Q04016. doi:`10.1029/2005GC001090`.

Seton, M., Müller, R., Zahirovic, S., Gaina, C., Torsvik, T., Shephard, G., Talsma, A., Gurnis, M., Turner, M., Maus, S., Chandler, M., 2012. Global continental and ocean basin reconstructions since 200 ma. Earth-Science Reviews 113, 212–270. doi:`10.1016/j.earscirev.2012.03.002`.

Shephard, G., Bunge, H.P., Schuberth, B., Müller, R., Talsma, A., Moder, C., Landgrebe, T., 2012. Testing absolute plate reference frames and the implications for the generation of geodynamic mantle heterogeneity structure. Earth and Planetary Science Letters 317, 204–217. doi:`10.1016/j.epsl.2011.11.027`.

Sigloch, K., Mihalynuk, M.G., 2013. Intra-oceanic subduction shaped the assembly of cordilleran north america. Nature 496, 50–56. URL: `http://dx.doi.org/10.1038/nature12019`.

Silver, P.G., M. Russo, R., Lithgow-Bertelloni, C., 1998. Coupling of south american and african plate motion and plate deformation. Science 279, 60–63. doi:`10.1126/science.279.5347.60`.

Simmons, N.A., Forte, A.M., Boschi, L., , Grand, S.P., 2010. Gypsum: A joint tomographic model of mantle density and seismic wave speeds. Journal of Geophysical Research 115. doi:`10.1029/2010JB007631`.

Stadler, G., Gurnis, M., Burstedde, C., Wilcox, L., Alisic, L., Ghattas, O., 2010. The dynamics of plate tectonics and mantle flow: From local to global scales. Science 329, 1033. doi:`10.1126/science.1191223`. sup and review available.

Stegman, D., Farrington, R., Capitanio, F., Schellart, W., 2010. A regime diagram for subduction styles from 3-D numerical models of free subduction. Tectonophysics 483, 29–45. doi:`10.1016/j.tecto.2009.08.041`.

Torsvik, T.H., Müller, R.D., Van der Voo, R., Steinberger, B., Gaina, C., 2008. Global plate motion frames: Toward a unified model. Reviews of Geophysics 46, 3004–+. doi:`10.1029/2007RG000227`.

Ulvrová, M., Labrosse, S., Coltice, N., Råback, P., Tackley, P., 2012. Numerical modelling of convection interacting with a melting and solidification front: Application to the thermal evolution of the basal magma ocean. Physics of the Earth and Planetary Interiors 206–207, 51–66. doi:`10.1016/j.pepi.2012.06.008`.

Wessel, P., Kroenke, L.W., 2008. Pacific absolute plate motion since 145 Ma: An assessment of the fixed hot spot hypothesis. Journal of Geophysical Research 113. doi:`10.1029/2007JB005499`.

Zhong, S., Yuen, D., Moresi, L., Schubert, G., 2007. Numerical methods in mantle convection, in: Bercovici, D. (Ed.), Treatise on Geophysics. Elsevier. volume 7, pp. 227–252.

A Article 4

Quevedo, L., Hansra, B., Morra, G., Butterworth, N. P., and Müller, R. D. (2013), **Oblique mid ocean ridge subduction modelling with the parallel fast multipole boundary element method**, *Comput Mech*, 51, 455–463, doi:10.1007/s00466-012-0751-5.

Oblique mid ocean ridge subduction modelling with the parallel fast multipole boundary element method

**L. Quevedo · B. Hansra · G. Morra ·
N. Butterworth · R. D. Müller**

Abstract Geodynamic models describe the thermo-mechanical evolution of rheologically intricate structures spanning different length scales, yet many of their most relevant dynamic features can be studied in terms of low Reynolds number multiphase creep flow of isoviscous and isopycnic structures. We use the BEM- EARTH code to study the interaction of the lithosphere and mantle within the solid earth system in this approximation. BEM- EARTH overcomes the limitations of traditional FD/FEM for this problem by considering only the dynamics of Boundary Integral Elements at fluid interfaces, and employing a parallel multipole solver accelerated with a hashed octtree. As an application example, we self-consistently model the processes controlling the subduction of an oblique mid-ocean ridge in a global 3D spherical setting in a variety of cases, and find a critical angle characterising the transition between an extensional strain regime related to tectonic plate necking and a compressive regime related to Earth curvature effects.

Keywords Boundary integral element · Mid ocean ridges · Subduction mechanics

L. Quevedo ( ) · B. Hansra · G. Morra · N. Butterworth ·
R. D. Müller
EarthByte Group, School of Geosciences, University of Sydney,
Sydney, NSW 2006, Australia
e-mail: leonardo.quevedo@sydney.edu.au

G. Morra
School of Earth and Environmental Sciences, Seoul National
University, Seoul, South Korea

1 Introduction

Subduction, the geological process by which the top brittle portion of the upper mantle (the lithosphere) sinks into the more ductile interior of the solid Earth, is the key geodynamic feature of our planet. Downwellings of cold and dense rocks at subduction zones provide the density, temperature and pressure gradients that drive mantle convection; generate the main force propelling plate tectonics (the *slab pull*); and are linked to most of the volcanism and seismicity that puts human lives at risk. The large body of research associated with subduction modelling attests to the complex geophysical aspects involved in its description as well as to difficulties arising from the scarcity of time and depth dependent observations relevant for their understanding.[1]

Multiphysics simulation has contributed to increase the degree of realism of subduction models by incorporating a broad range of attributes and processes influencing very general visco-elasto-plastic rock rheology depending on chemical composition, pressure, temperature and stress. Additionally, setting this systems in a planetary scale spanning very large variations in size and physical properties result in very complex models that push the traditional FEM and FD methods to their limit. Such immense and intricate parameter space makes extremely difficult to pinpoint the effect of an individual variable in the behaviour of the system. As a consequence, in order to discover parameters that control dynamic features of subduction, many systems have been explored only in 2D or in highly symmetric simplified 3D geometries, and with physical constrains to reduce the total number of degrees of freedom.

Global tectonic modes are particular examples in which the simplification leads to concise relationships between

---

[1] For a review on current trends in subduction modelling see [11].

input variables and dynamic behaviour. By describing the full solid earth convection flow in spherical harmonics, the global plate kinematic behaviour can be inferred starting from a simple rheological model of the mantle and an estimation of plate driving forces based on models of the subduction history [15,10]. In this way it has been possible to predict (or more precisely to reproduce) the observed present day and the reconstructed paleo plate kinematics from simplified models of the viscosity and density heterogeneities of the solid earth.

Recent models [1,5,6] have revealed the importance of slab pull variations due to the parallel subduction of a mid-ocean ridge (MOR) in tectonic dynamics. Since they define the regions where oceanic lithosphere is being created from the cooling of magma, these ridges tend to be hotter and more buoyant than the rest of the plate. As they approach a subduction trench that is parallel to their axis, they might cause necking and detachment of the portion that has already subducted (the *slab*) and eventually a dramatic decrease of slab pull which could lead to subduction cessation. Similarly, the subduction of an active ridge orthogonal to the trench could lead to the opening of a window between two slabs significantly altering the pattern of mantle flow in the solid earth. It is therefore essential to the understanding of global tectonics to consider the subduction of such ridges in the more general oblique setting in which they usually occur.

We present the first 3D self consistent dynamical simulations of oblique MOR subduction spanning the complete range of oblique collision angles. The self-consistent dynamic description of 3D ridges, modelled as an indentation in an otherwise flat rectangular tectonic plate, is simplified by assuming a temperature independent viscous creep rheology governed by the Stokes equation. Using a multipole accelerated boundary integral element method, we were able to explore the full range of values of different ridge-trench collision angles between the parallel and orthogonal cases, compare strain estimations on the ridge for different collision angles, and characterise the transition between an extensional regime associated to slab tearing and a compressive regime related to Earth curvature effects. Such transition was impossible to detect in previous works which were limited by computational complexity to the analysis of simplified geometries, end-member cases, 2D models, or particular regional studies [20].

For this study, we use the BEM-EARTH [17,18,21,24] geodynamic modelling software, which allows the study of regional subduction in the context of global spherical mantle flow, reducing the problem dimensionality and accelerating the solution of the resulting dense systems. By integrating multipole methods parallelised using MPI for distributed memory architectures with hashed octtree algorithms for fast identification of near and far-field interacting elements, BEM-EARTH is able to overcome some of the limitations of finite difference/element methods traditionally used in geodynamics.

2 MOR subduction

Despite recent advances, most geodynamic models of ridge-trench collision are two dimensional and involve either a parallel or an orthogonal ridge-axis-to-trench angle. Furthermore, ridge subduction beyond simple slab detachment in the parallel case, has not been reproduced by any 2D thermo-mechanical model and is believed to be caused by 3D effects.

Present day examples of ridge-transform systems intersecting convergent margins like the Chile (Nazca-Antarctica), Rivera (Rivera-Pacific) and Mendocino triple junctions [4] indicate that the simultaneous subduction of two adjacent plates along the same trench is not uncommon, and is manifested trough different tectonic settings for which the angle between the transform or ridge axis and the trench varies. Such ridge-trench collisions have been almost exclusively studied in the parallel case in relation to the the dynamics of subduction cessation and slab detachment [5,1,6] and in the orthogonal case, where they are related to the formation of slab windows [14]. In the parallel case, when a ridge approaches a convergent margin the downgoing material becomes progressively younger and harder to subduct. Lithosphere as old as 10 Myr is considered to be already neutrally buoyant with respect to the surrounding mantle [8] and is not expected to contribute significantly to the downward pull. Eventually, the combined effect of buoyancy and the weakening of the slab at the ridge axis may lead to the cessation of subduction and subsequent detachment of the subducted slab [5,12]. In the orthogonal case, as the diverging oceanic plates subduct, magma that could form at the edges of the plates will not be able to cool down to continue lithospheric formation, thereby forming a *slab window*. Such tearing of the slab and an eventual detachment inhibits the capacity of slabs to propagate stresses through plates and their boundaries and alter the pattern of mantle convection [9,10] therefore having a profound impact on the dynamics of plates and mantle [6,33]. Assuming slab pull is the most significant force driving plate tectonics, the decrease of the pull force associated with ridge subduction could have dramatic implications for tectonic dynamics, in particular for global plate reorganisations.

We use the BEM-EARTH software to self-consistently model the processes controlling such a tectonic setup in a variety of cases, assuming a lithosphere immersed in a less viscous and less dense mantle, an inviscid highly dense core and virtually frictionless plate boundaries.

3 Fluid mechanical model

Mantle circulation and plate tectonic dynamics in the solid earth, characterised by very low Reynolds number, is governed by the Stokes equation for steady, highly viscous flow

$$\nabla \cdot \sigma + \rho \mathbf{b} = 0. \tag{1}$$

where σ_{ij} is the full stress tensor, and $\mathbf{b}$ represents the body forces. In terms of the dynamic viscosity μ, the velocity field $\mathbf{u}$, and the pressure P, the gradient of the stress tensor is given by

$$\nabla \cdot \sigma = \mu \nabla^2 \mathbf{u} - \nabla P. \tag{2}$$

Following several numerical and experimental studies [3,25], we approximate the fluid dynamics of subduction by considering the mantle and the lithosphere as regions of homogeneous density and viscosity, disregarding other the chemical and rheological inhomogeneities. We further assume a simple temperature independent rheology for such multiphase flow, and model only the fundamental forces controlling the process, which we take to be: the buoyancy resulting from the different densities between the flow phases; the viscous drag that might hamper or assist plate motion; and the viscous resistance to bending and stretching.

For our applications we will be interested in the dynamics of subducting plates considered as isoviscous and isopycnic surfaces immersed in a homogeneous mantle. We will therefore solve the flow field for a system consisting of an interface S_1 representing the surface of the earth, surrounded by an unbounded fluid and having disconnected closed interfaces inside representing the subducting slab S_3 and the core-mantle boundary S_2 (see Fig. 1). The boundary conditions are prescribed by the interfacial surface forces $\Delta\mathbf{f}$ resulting from the different material properties of each phase. From Eq. (1) we see that the normal stress discontinuity produced by the differential density ($\Delta\rho = \rho_2 - \rho_1$) of two phases subject to a gravitational acceleration $\mathbf{g}$, is

$$\Delta\mathbf{f}(\mathbf{x}) = \Delta\rho(\mathbf{x}) \ (\mathbf{g}(\mathbf{x}) \cdot \mathbf{x}) \ \mathbf{n}, \tag{3}$$

whereas the velocity field is continuous throughout the full domain. The gravitational acceleration inside the mantle varies in magnitude from $10.8\,\mathrm{ms}^{-2}$ at the core mantle boundary down to $9.8\,\mathrm{ms}^{-2}$ near the surface [31]. Given that main contributions to (3) come from the density contrast and the position, we will assume a radially oriented gravitational field of constant magnitude $g = 10\,\mathrm{ms}^{-2}$. Forcing, deformation and velocity fields are further required to vanish at infinity.

For a point $\mathbf{x}_0$ inside a region V where the viscosity μ is homogeneous, Eq. (1) can be solved for the flow field $\mathbf{u}(\mathbf{x})$ and the pressure field $P(\mathbf{x})$ using the Green function method. The boundary integral formulation [23] of the solution in terms of the Lagrangian specification of the flow field takes the form:
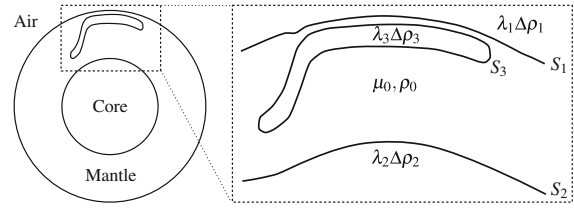

Fig. 1 Subducting plate dynamic as a multiphase flow bounded by the free surfaces S_i. S_1 represents the surface of the Earth, S_2 a viscosity transition at the core–mantle-boundary and S_3 the surface of the subducting plate

$$
u_j(\mathbf{x}_0) = -\frac{1}{8\pi\mu} \int_{\partial V} f_i(\mathbf{x}) G_{ij}(\mathbf{x}, \mathbf{x}_0) dS(\mathbf{x})
$$

$$
+ \frac{1}{8\pi} \int_{\partial V} u_i(\mathbf{x}) n_k(\mathbf{x}) T_{ijk}(\mathbf{x}, \mathbf{x}_0) dS(\mathbf{x}). \tag{4}
$$

Here the cartesian components of the field $\mathbf{u}(\mathbf{x}) = u_j(\mathbf{x})\hat{\mathbf{e}}_j$ are represented in terms of the surface force $\mathbf{f} = \sigma \cdot \mathbf{n}$ and the fundamental solutions G_{ij} and T_{ijk} for the velocity and traction. The integral domain is the boundary ∂V of the region, where the surface element and the components of the normal are $dS(\mathbf{x})$ and $n_k(\mathbf{x})$ respectively. The explicit form of the fundamental solutions, known as *Stokeslet* and *Stresslet* are

$$
G_{ij}(\mathbf{x}, \mathbf{x}_0) = \frac{\delta_{ij}}{r} + \frac{r_i r_j}{r^3}, \qquad T_{ijk}(\mathbf{x}, \mathbf{x}_0) = -6\frac{r_i r_j r_k}{r^5}, \tag{5}
$$

where $\mathbf{r} = \mathbf{x} - \mathbf{x}_0$ and $r = |\mathbf{r}|$. The pressure field can be directly calculated through an integral equation analogous to (4) [23, Eq. (2.3.17)], yet we will only focus on the flow field since it completely defines the dynamic of the system.

In order to solve for the velocities using (4), we first need to find its values on the boundary given the particular constrain. To this aim, we first find the solution right on the boundary $\mathbf{x}_0 \in \partial V$, which leads the following expression involving the *principal value* (PV) of the Stresslet integral:

$$
u_j(\mathbf{x}_0) = -\frac{1}{4\pi\mu} \int_{\partial V} f_i(\mathbf{x}) G_{ij}(\mathbf{x}, \mathbf{x}_0) dS(\mathbf{x})
$$

$$
+ \frac{1}{4\pi} \int_{\partial V}^{\mathrm{PV}} u_i(\mathbf{x}) n_k(\mathbf{x}) T_{ijk}(\mathbf{x}, \mathbf{x}_0) dS(\mathbf{x}), \tag{6}
$$

here the PV is the improper integral value when the point $\mathbf{x}_0$ is right on the boundary.

In practice, we will find the values for the velocity on the quasi-steady boundaries of multiphase flows for which we prescribe the known surface force $\mathbf{f} = \Delta\mathbf{f}$ that accounts for buoyancy.

Using mantle viscosity (density) μ_0 (ρ_0) as a reference and defining a relative viscosity $\lambda_i = \mu_i/\mu_0$ for each particular phase i, we can write the velocity at the boundary $S_i = \partial V_i$ of such phase as a Fredholm integral of the second kind [23,17,16]:

$$\mathbf{u}(\mathbf{x}_0) = -\left(\frac{1}{1+\lambda_i}\right)\frac{1}{4\pi\mu_0}\sum_j \int\limits_{S_j} \mathsf{G}(\mathbf{x})\cdot\Delta\mathbf{f}(\mathbf{x})\,dS(\mathbf{x}),$$

$$-\sum_j\left(\frac{1-\lambda_j}{1+\lambda_i}\right)\frac{1}{4\pi}\int\limits_{S_j}^{PV}\mathbf{u}(\mathbf{x})\cdot\mathsf{T}(\mathbf{x},\mathbf{x}_0)\cdot\mathbf{n}(\mathbf{x})\,dS(\mathbf{x}),$$

$$(7)$$

which might be solved using an iterative technique. Furthermore, we can study the evolution of the flow by solving only on the boundaries and use the Eq. (4) whenever we want a general solution at any point in space.

At each instant, the geometry of the interfaces completely defines the flow field. In turn, the flow field completely defines the evolution of the interfaces, which can be specified in terms of a set of Lagrangian points for each surface S_i:

$$\frac{\partial\mathbf{x}_{S_i}(t)}{\partial t} = \left[\mathbf{u}(\mathbf{x}_{S_i},t)\cdot\mathbf{n}\right]\mathbf{n} + \delta\mathbf{t},\qquad(8)$$

where $\mathbf{n}$ and $\mathbf{t}$ are unit vectors normal and tangential to the point at the surface and δ is a constant. Both the value of δ and the particular orientation of $\mathbf{t}$ are arbitrary. Since the surfaces S_i represent interfaces between fluids and tangential motion have no effect on their shape, we are free to choose $\delta\mathbf{t} = \mathbf{u}\cdot(\mathbf{1}-\mathbf{nn})$ and identify the velocity of points $\mathbf{x}_{S_i}$ with the velocity of the fluid,

$$\frac{\partial\mathbf{x}_{S_i}(t)}{\partial t} = \mathbf{u}(\mathbf{x}_{S_i},t),\qquad(9)$$

which can be explicitly integrated numerically once the value of the flow field on the interface is known.

3.1 Thin lubrication layer

In self consistent simulations of tectonics involving only one plate, the negative buoyancy of the lithosphere would induce vertical sinking, since the mantle is free to overflow the surface of the plate. In order to simulate subduction behaviour without considering the contribution of surrounding plates or studying the global system of inter-plate stresses, we interpose a thin lubrication layer between the surface of the Earth and the surfaces contained within [17,22,25]. This layer allows the plate to slide in any tangential direction, but restores the isostatic equilibrium that keeps it from sinking radially.

4 Numerical method

We simulate the self-consistent fluid mechanical evolution of the subducting slab in a spherical setup, driven by buoyancy, viscous drag, and resistance to bending and stretching without kinematic constrains, using the BEM- EARTH
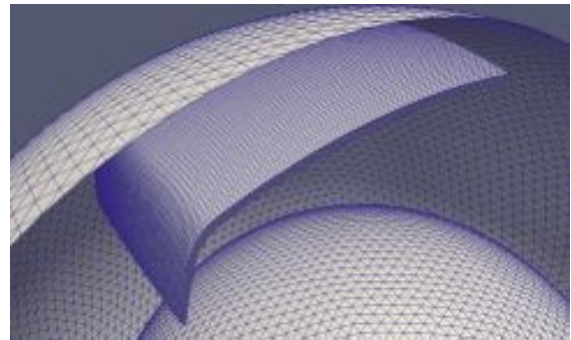

Fig. 2 Discretisation of a typical model of a subducting plate immersed in the mantle between the surface of the Earth and the core–mantle boundary

code [17,18,21,24], a parallel multipole accelerated boundary integral element solver for the steady low Reynolds number flow.

The boundary S_i of each phase is discretised in space as a 3D unstructured triangulated surface mesh (see Fig. 2) on which the variables ($\mathbf{u}$, $\mathbf{f}$, ...) are defined using the collocation approach. A local orthogonal cartesian coordinate system is used to represent the values of linear shape functions that interpolate the variables within each triangle. The kernels integrals in 7 are calculated analytically for this interpolation, leading to a numerically equivalent linear system of the form

$$\left[\varLambda + \mathsf{T}\right]\mathbf{U} = \mathbf{F},\qquad(10)$$

where $\varLambda$ is a matrix containing constant coefficients associated with each surface relative viscosity, T is the discrete kernel of the Stresslet integral, $\mathbf{F}$ the numerical value of the Stokeslet integral on the surface and $\mathbf{U}$ the unknown velocities at each element.

Integrating the kernels to obtain the linear system (10) is a particularly complex task due to the presence of $\mathscr{O}(1/r^3)$ divergencies that render the integral hypersingular. The nature of the regularisation process required to obtain a closed form of the matrix elements [26] leads to very cumbersome expressions requiring the use of symbolic analytical computational tools.

As an example the Stokeslet term in (7) in terms of linear local shape functions $\varphi_a(\mathbf{x})$ defined at each triangle $\mathbf{x}\in T_a$ of the mesh, has the form

$$\sum_{a=1}^{N} g_a(\mathbf{x}_0) = \sum_{a=1}^{N}\int\limits_{T_a} G_{ij}(\mathbf{x},\mathbf{x}_0)n_i(\mathbf{x})n_j(\mathbf{x}_0)\varphi_a(\mathbf{x})dS(\mathbf{x}),$$

$$(11)$$

where the integral is performed on each triangle. A closed expression for this integral in the local coordinate basis has the general form

$$g_a(\mathbf{x}_0) = n_i(\mathbf{x}) \left[\left(1 - \frac{y_0}{y}\right) A_{ij}(\mathbf{x}_0) - \frac{1}{y} B_{ij}(\mathbf{x}_0) \right] n_j(\mathbf{x}_0). \tag{12}$$

where A is a 3×3 matrix of rational functions, and B is a 3×3 matrix involving regular rational and trigonometric functions. The reader is referred to [26] for around 15 explicit independent terms present in each case: inside the triangle $\mathbf{x}_0 \in T_a$, outside the triangle $\mathbf{x}_0 \notin T_a$ and at the boundary of the triangle $\mathbf{x}_0 \in \partial T_a$.

4.1 Fast multipole acceleration

Equation (10) is well-conditioned but dense [34], meaning that the complexity of the calculation of the left hand side of Eq. (10) scales with N^2 for N boundary elements. The decay of the kernels in Eq. (5) and their derivatives with the distance may be used to overcome the poor scaling behaviour of a direct calculation by allowing the application of the fast multipole method [2,13]. In analogy with the multipole expansion of a potential outside the support of an electrostatic charge distribution, our kernels of interest are approximately degenerate, therefore the interaction between sufficiently separated points $\mathbf{x}$ and $\mathbf{y}$ can be approximated by an expression of the form

$$K(\mathbf{x} - \mathbf{y}) \approx \sum_{k=0}^{p-1} \Phi_k(\mathbf{x}) \Phi_k(\mathbf{y}) \tag{13}$$

Effectively decoupling the interactions and allowing a $\mathcal{O}(pN)$ complex calculation of sums of the form

$$\sum_{i \neq j}^{N} V(\mathbf{x}_i) K(\mathbf{x}_i - \mathbf{x}_j) P(\mathbf{x}_j)$$
$$\approx \sum_{k=0}^{p-1} \left(\sum_{i=1}^{N} \Phi_k(\mathbf{x}_i) V(\mathbf{x}_i) \right) \Phi_k(\mathbf{x}_j) P(\mathbf{x}_j) \tag{14}$$

in the Eq. (10). In our case the accelerated approximation algorithm is based on clustering the point-like triangle sources of stress and Stokes field at different length scales and integrate the interaction kernel according to their separation. When the points are close, the kernel is directly integrated, when they are far, the multipole expansion is used (see Fig. 3). BEM- EARTH implements multipole expansions for the Stokeslet or the Stresslet up to the second order.

The Stokeslet and Stresslet multipole expansion can be obtained from the degenerate approximation of the well known single-layer (point charge) and double-layer (dipole) electrostatic potentials [7,27]

$$\phi(\mathbf{x} - \mathbf{y}) = \frac{1}{|\mathbf{x} - \mathbf{y}|}, \qquad \Phi(\mathbf{x} - \mathbf{y}) = \frac{\mathbf{n} \cdot (\mathbf{x} - \mathbf{y})}{|\mathbf{x} - \mathbf{y}|^3}. \tag{15}$$
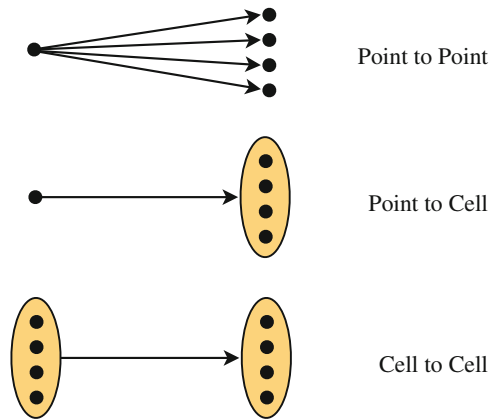

Fig. 3 Depending on the distance between the sources, the contribution to the interaction on each surface is done using local (point to point) or multipole terms (point to cell and cell to cell)
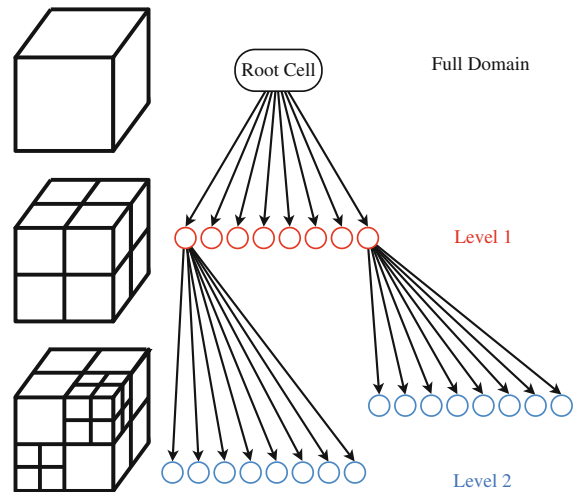

Fig. 4 A volume is progressively subdivided from the full *root cell* into finer regular partitions that define the cells at each level

Applying suitable generating operators [30], the evaluation of the Stokeslet and Stresslet is reduced to

$$G_{ij}(\mathbf{x} - \mathbf{y}) = \left(\delta_{ij} - (x_i - y_j) \frac{\partial}{\partial x_i} \right) \frac{1}{|\mathbf{x} - \mathbf{y}|} \tag{16}$$

$$T_{ijk}(\mathbf{x} - \mathbf{y}) n_k(\mathbf{x}) = \frac{1}{6} \left[\left(\delta_{ij} - (x_i - y_j) \frac{\partial}{\partial x_i} \right) \frac{\mathbf{n} \cdot (\mathbf{x} - \mathbf{y})}{|\mathbf{x} - \mathbf{y}|^3} \right.$$
$$\left. + \left(\delta_{ik} - (x_k - y_k) \frac{\partial}{\partial x_i} \right) \frac{n_k(x_j - y_j)}{|\mathbf{x} - \mathbf{y}|^3} \right] \tag{17}$$

The boundary elements involved in system of Eq. (10) are classified in a spatial tree structure in which aggregations of sources cluster together into *cells* at successive levels of refinement (see Fig. 4). The field evaluation is approximated
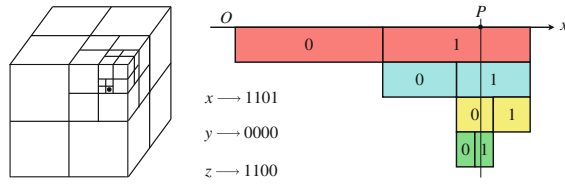
Fig. 5 Coordinates are stored as a binary keys encoding what side of the bisection and at what level the particle is located. The three coordinates are further interleaved and prepended a most significant bit. For the example shown the binary key would be $k_2 = 1\ 101\ 101\ 000\ 100$ which translates to the decimal integer $k_{10} = 6\ 980$
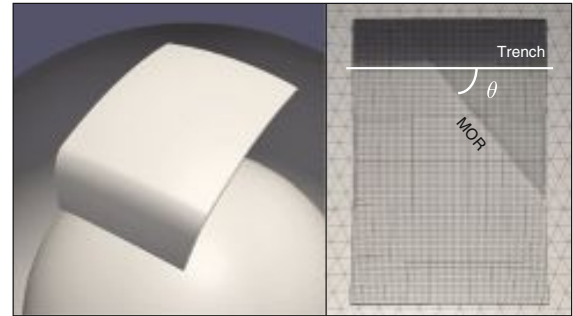

Fig. 6 Typical model setup

through a tree traversal that is truncated according to a prescribed numerical tolerance ϵ. Knowing the maximum distance of the particles from the centre of the cell d, and the value of the correspondent quadrupole moment B_2, for expansions up to second order, an analytical expression for the error per interaction can be derived [32]

$$r = \frac{d}{2} + \sqrt{\frac{d^2}{4} + \sqrt{\frac{3B_2}{\epsilon}}} \qquad (18)$$

leading to a strict criteria defining the smallest interaction distance r to be considered for each cell. This efficiently truncates the calculation by clearly establishing how much the algorithm must traverse the hierarchical structure to obtain the desired precision.[2]

BEM- EARTH uses a hashed octtree method to hierarchically partition 3D space and store cell locations in a integer key. A point P with coordinates $\mathbf{x} = (x, y, z)$ point is located by iteratively bisecting the volume at each axis and storing a single bit representing that it is to be found to the left (0) or right (1) of the midpoint (see Fig. 5). Resulting coordinate words are bitwise interleaved and prepended with a 1-bit to represent all nodes at each level consistently without ambiguities derived from trailing zeroes:

$$
\begin{array}{c|c|c|c|c}
x & 1 & 1 & 0 & 1 \\
y & 0 & 0 & 0 & 0 \\
z & 1 & 1 & 0 & 0 \\
k_2 & 1\ 1\ 0\ 1 & 1\ 0\ 1 & 0\ 0\ 0 & 1\ 0\ 0
\end{array}
$$

This key is directly mapped to index memory locations containing the cell dependent data needed for the calculation and simplifies its balanced distribution in a parallel system. The stopping criteria at each level of refinement is linked to the most significant bit.

A parallel generalised minimal residual method with restart parameter k is used to iteratively solve Eq. (10). Once the flow field at the surfaces is known, an explicit second

order Runge–Kutta adaptive timestep integration of Eq. (9) is performed. The solution is thus only calculated at the end of step and at the half-step. The time step size is constrained by a maximum displacement parameter smaller than half of the characteristic length of the smallest element, satisfying the convergence criteria of the solver. An incompressibility condition is enforced a posteriori on each surface by comparing the total volume surrounded by each interface with the previous timestep, and isotropically correcting the normal displacements according to the residual found. The thin lubrication layer is implemented through an additional correction of normal stresses of the surface elements that lie within a fixed distance of the external surface [18,19].

As the surfaces to be studied have a constrained size and their evolution is followed only up to the point where reach the core-mantle boundary, the deformation of the mesh is not significant enough to require remeshing or additional algorithms to prevent topological changes.

Each model consisting of 61,260 elements with 30,636 nodes was run on a single 8-core SGI Altix XE310 Server blade containing two Intel Xeon X5355 2.66 GHz cpus and 16 GB RAM, part of the Silica cluster at The University of Sydney. The models ran for 150 timesteps with an average 310 s cpu time per step for a total of 13 h of cpu time per run, equivalent to about an hour and a half real time per model. Overall, the useful work performed by BEM- EARTH scales as $\mathcal{O}(N \log N)$ for N boundary elements [21].

5 Oblique ridge subduction model

The different impermeable viscosity/density contrasts defining the phases are the plate surface, the core-mantle boundary and the surface of the Earth, which is free to deform under the stresses produced by the underlying lithosphere and mantle, and has a thin lubrication layer underneath.

We model a rectangular plate with fixed width and length and a thickness of 95 km immersed in a non layered homogeneous mantle and impose density and viscosity contrasts at its boundary (see Fig. 6). The lithosphere is taken to be

---

[2] Similar truncation of matrix entries can be achieved by the wavelet method [29], albeit with a more complicated strategy where its polynomial order depends on the scale.

Table 1 Basic model parameters

Density (contrast)		
Mantle	ρ_M	3, 300 kg m^{-3}
Lithosphere	$\Delta\rho$	30 kg m^{-3}
Viscosity		
Mantle	μ_0	1.0×10^{21} Pa s
Lithosphere	μ	200.0×10^{21} Pa s
Core	μ_C	10.0×10^{21} Pa s
Gravity (magnitude)	g	10 ms^2
Plate dimensions	$L \times W \times D$	$5,097 \times 3,823 \times 95$ km^3
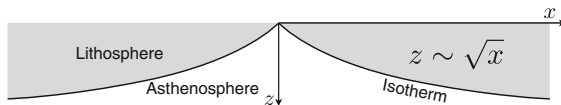
Fig. 7 Profile of a mid ocean ridge

200 times more viscous and than its surrounding mantle, and having a constant density contrast of $\Delta\rho = 30$ kgm^{-3} respect to it. The plate is initially discretised as a regular triangular mesh subdivided 80, 60 and 4 times along its length, width and depth respectively, with a minimum initial mesh element length of around 20 km requiring a total of circa 90,000 boundary elements. As the simulation progresses, the mesh deforms into an unstructured mesh with variable resolution. Though it is possible to adaptively remesh the surface in response to changes in curvature, we chose not to in favour of computational efficiency. The basic model parameters are shown in Table 1. The plate is indented according to the lithospheric thickness profile of a MOR which follows a linear relationship between the thickness off the lithosphere and the square root of the normal distance to the axis (see Fig. 7). Once indented, the plate is bent at a dipping angle of 50° to represent ongoing subduction of 15 % of its length when the simulation starts. The shape is projected to the sphere according to its thickness and depth and positioned in between the surfaces representing the core and surface of the Earth. Similar setups for which the angle θ between the MOR axis and the trench is varied between 0° and 90° are studied.

6 Results

The BEM- EARTH code approximation leads to a very coherent plate motion typical of viscous slab numerical and laboratory experiments on subduction [3,28]. All model runs experience a transition stage in which the surface of the Earth deforms as the lubrication layer responds to lithostatic compensation. The system then evolves freely under the influence of gravity through slab pull, until it reaches a quasi-steady-state regime in which plate motion increases very gradually
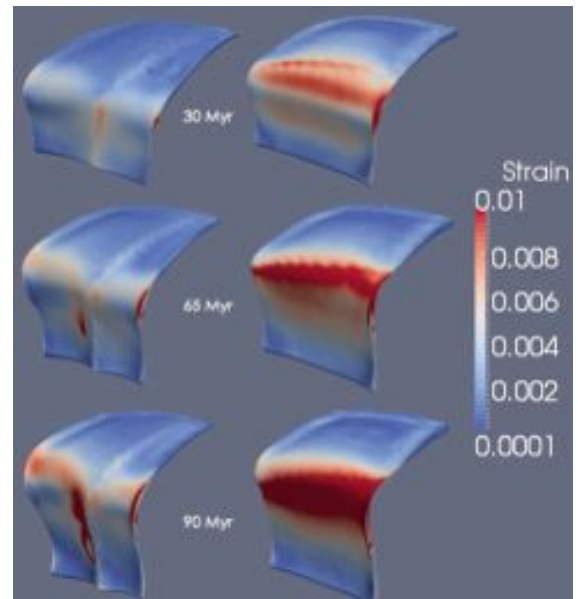
Fig. 8 Time evolution of oblique MOR subduction at 80° (*left*) and 10° (*right*) after 30, 65 and 90 million years

in time and the slab subducts in a near vertical fashion. It is in this stage that the different modes of subduction depending on the oblique MOR angle become apparent. Finally the slab reaches the core and the simulation stops.

Throughout the runs the strain rates at the tail of the plate are consistently low for all the models and only a small degree of lateral subduction and shortening is to be noticed as a boundary effect. In general most of the strain accumulates in the bending of the trench and around the MOR axis, but as subduction progresses the onset of two different modes of subduction are to be noticed (see Fig. 8). Varying the angle between the MOR axis and the trench results in two distinctive phases of subduction dynamics whose end members are characterised by compression and folding in one case and pure stretching and necking in the other (see Fig. 9).

In the first case the slab accommodates to the reduced space available at depth with a sharp fold localised around the near-vertical MOR axis and presents a very uniform inward radial speed or *sinking rate*. In contrast, near parallel to trench subduction of a MOR shows a strong differential sinking rate between each side of the ridge and a high strain rate spread over a broader region around both trench and ridge axis. A transition between these two regimes is to be found at around 60° when the sinking rates at both sides of the MOR becomes comparable (see Fig. 10). The relative motion of points at different sides of the ridge indicates that the two resulting regimes are further distinguished by a compressive versus an extensional regime across the ridge.
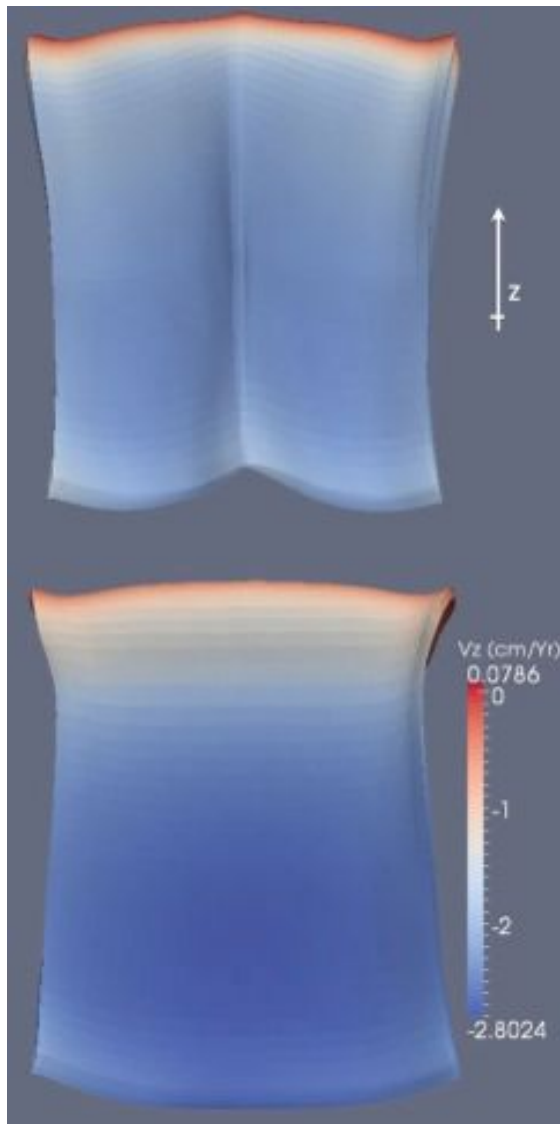
Fig. 9 MOR subduction orthogonal (*top*) and parallel to the trench (*bottom*) as end members of oblique MOR subduction dynamics characterised by folding and by necking and stretching respectively. (Color figure online)

Fig. 10 Slabs of increasing oblique subduction angle from 0° to 80° in 10° increments, *coloured* according to their sinking rates (v_z) as in Fig. 9. The *first element in the last row* is the 60° critical angle for which the sinking rates at both sides are comparable

Fig. 11 Change in shape of the subducting slab after 100 timesteps with varying resolution. As resolution increases the profile approaches the shaded region, suggesting convergence (cf. [19])

We have tested a the robustness of the results respect to the mesh resolution for a non indented square slab with a length equivalent to the radius of the Earth R_{Earth} by varying the element size between $0.005 \times R_{Earth}$ and $0.013 \times R_{Earth}$ (see Fig. 11) leading to surface meshes with a total number of elements between 5,625 and 40,000. The magnitude of the correction after 100 timesteps progressively decays at higher resolution suggesting convergence. Higher resolution models tend to be more flexible, yet the position of the
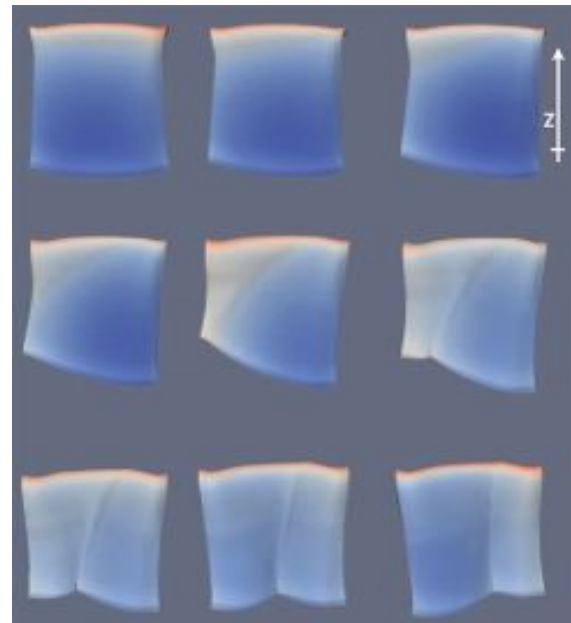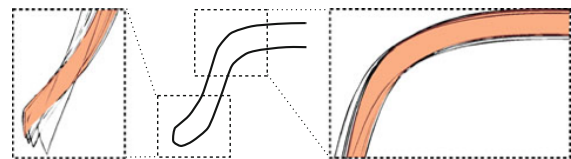
trailing edge of the slab and the speed of its motion remains essentially unchanged [19].

7 Discussion and conclusions

The most remarkable result is the observation that the angle between the MOR axis and the trench seems to be related *ceteris paribus* with the two different modes of subduction which are separated at a value of around 60°. This suggests that the the oblique angle of subduction is a quantity that could control when a slab detaches forming a window or folding into a tighter closed configuration. Further numerical modelling including non-linear viscous and plastic rheology would be necessary to address this claim. Possible geological evidence could derive from the geochemical signature of

volcanism associated with slab windows in the near-parallel oblique subduction case.

In contrast to models with mantle layering, our slab sinks radially with little trench retreat until it reaches the core. Though such scenario may not be entirely realistic, it enhances the effects of oblique subduction. The fact that the stretching and folding start just after the equilibration stage at the beginning of the simulation is strong indication that the different subduction modes we have shown are likely to be present in a more detailed model including the effects of mantle layering.

References

1. Andrews ER, Billen MI (2009) Rheologic controls on the dynamics of slab detachment. Tectonophysics 464(1–4):60–69
2. Barnes J, Hut P (1986) A hierarchical o(n log n) force-calculation algorithm. Nature 324(4):446–449
3. Bellahsen N, Faccenna C, Funiciello F (2005) Dynamics of subduction and plate motion in laboratory experiments: insights into the "plate tectonics" behavior of the earth. J Geophys Res 110(B1):1–15
4. Bird P (2003) An updated digital model of plate boundaries. Geochem Geophys Geosyst 4(3):1027–1028
5. Burkett ER, Billen MI (2009) Dynamics and implications of slab detachment due to ridge-trench collision. J Geophys Res 114(B12)
6. Burkett ER, Billen MI (2010) Three-dimensionality of slab detachment due to ridge-trench collision: laterally simultaneous boudinage versus tear propagation. Geochem Geophys Geosyst 11(11)
7. Cheng H, Greengard L, Rokhlin V (1999) A fast adaptive multipole algorithm in three dimensions. J Comput Phys 155(2):468–498
8. Cloos M (1993) Lithospheric buoyancy and collisional orogenesis: Subduction of oceanic plateaus, continental margins, island arcs, spreading ridges, and seamounts. Geol Soc Am Bull 105(6):715–737
9. Conrad CP, Lithgow-Bertelloni C (2002) How mantle slabs drive plate tectonics. Science 298(5591):207–209
10. Conrad CP, Lithgow-Bertelloni C (2004) The temporal evolution of plate driving forces: Importance of "slab suction" versus "slab pull" during the cenozoic. J Geophys Res 109(B10)
11. Gerya T (2011) Future directions in subduction modeling. J Geodyn 52(5):344–378
12. Gerya TV, Yuen DA, Maresch WV (2004) Thermomechanical modelling of slab detachment. Earth Planet Sci Lett 226(1–2):101–116
13. Greengard L, Rokhlin V (1987) A fast algorithm for particle simulations. J Comput Phys 73(2):325–348
14. Groome W, Thorkelson D (2009) The three-dimensional thermomechanical signature of ridge subduction and slab window migration. Tectonophysics 464(1-4):70–83
15. Hager BH, O'Connell RJ (1981) A simple global model of plate dynamics and mantle convection. J Geophys Res 86(B6):4843–4867
16. Ingber M, Mondy L (1993) Direct second kind boundary integral formulation for stokes flow problems. Comput Mech 11(1):11–27
17. Morra G, Chatelain P, Tackley P, Koumoutsakos P (2007) Large scale three-dimensional boundary element simulation of subduction. In: Shi Y, van Albada GD, Dongarra J, Sloot PM (eds) Computational Science (ICCS 2007) 7th international conference, Beijing, China, May 27–30, 2007, Proceedings, Part I. Lecture notes in computer science, vol 4489, Springer, Heidelberg, pp 1122–1129
18. Morra G, Chatelain P, Tackley P, Koumoutsakos P (2009) Earth curvature effects on subduction morphology: modeling subduction in a spherical setting. Acta Geotech 4(2):95–105
19. Morra G, Quevedo L, Müller RD (2012) Spherical dynamic models of top-down tectonics. Geochem Geophys Geosyst 13
20. Morra G, Regenauer-Lieb K, Giardini D (2006) Curvature of oceanic arcs. Geology 34(10):877–880
21. Morra G, Yuen DA, Boschi L, Chatelain P, Koumoutsakos P, Tackley PJ (2010) The fate of the slabs interacting with a density/viscosity hill in the mid-mantle. Phys Earth Planet Inter 180(3–4):271–282
22. OzBench M, Regenauer-Lieb K, Stegman DR, Morra G, Farrington R, Hale A, May DA, Freeman J, Bourgouin L, Mühlhaus H, Moresi L (2008) A model comparison study of large-scale mantle-lithosphere dynamics driven by subduction. Phys Earth Planet Inter 171(1–4):224–234
23. Pozrikidis C (1992) Boundary integral and singularity methods for linearized viscous flow, vol 7. Cambridge University Press, Cambridge
24. Quevedo L, Morra G, Müller RD (2010) Parallel fast multipole boundary element method for crustal dynamics. IOP Conf Ser Mater Sci Eng 10(1):012
25. Ribe N (2010) Bending mechanics and mode selection in free subduction: a thin-sheet analysis. Geophys J Int 180(2):559–576
26. Salvadori A (2001) Analytical integrations of hypersingular kernel in 3d bem problems. Comput Methods Appl Mech Eng 190(31):3957–3975
27. Shen L, Liu Y (2007) An adaptive fast multipole boundary element method for three-dimensional potential problems. Comput Mech 39(6):681–691
28. Stegman DR, Freeman J, Schellart WP, Moresi L, May D (2006) Influence of trench width on subduction hinge retreat rates in 3-d models of slab rollback. Geochem Geophys Geosyst 7(3)
29. Tausch J (2003) Sparse BEM for potential theory and stokes flow using variable order wavelets. Comput Mech 32(4):312–318
30. Tornberg AK, Greengard L (2008) A fast multipole method for the three-dimensional stokes equations. J Comput Phys 227(3):1613–1619
31. Turcotte DL, Schubert G (2002) Geodynamics, vol 2. Cambridge University Press, Cambridge
32. Warren MS, Salmon JK (1993) A parallel hashed oct-tree n-body algorithm. In: Borchers B, Crawford D (eds) Supercomputing 93: Proceedings of the 1993 ACM/IEEE conference on supercomputing. ACM, New York, pp 12–21
33. Whittaker JM, Müller RD, Leitchenkov G, Stagg H, Sdrolias M, Gaina C, Goncharov A (2007) Major australian-antarctic plate reorganization at hawaiian-emperor bend time. Science 318(5847):83–86
34. Zhu G, Mammoli A, Power H (2006) A 3-d indirect boundary element method for bounded creeping flow of drops. Eng Anal Bound Elem 30(10):856–868